

# Optical characterisation of ozonated electrochromic nickel vanadium oxide flexible thin films

---

Taha Ahmed

Department of engineering sciences  
Division of solid state physics



UPPSALA  
UNIVERSITET

Abstract

## Optical characterisation of ozonated electrochromic nickel vanadium oxide flexible thin films

---

Teknisk-naturvetenskaplig fakultet  
Institutionen för teknikvetenskaper  
UTH-enheten

*Taha Ahmed*

Besöksadress:  
Ångströmlaboratoriet  
Lägerhyddsvägen 1  
Hus 4, plan 0

Postadress:  
Box 536  
751 21 Uppsala

Telefon:  
018-471 30 03

Telefax:  
018-471 30 00

Hemsida:  
<http://www.teknat.uu.se/student>

Electrochromic nickel vanadium oxide thin-films on flexible substrates were subjected to cyclic voltammetry in KOH(aq) electrolytes of pH 14 and pH 12, and in LiClO<sub>4</sub>(PC) at  $c(\text{Li}^+) = 1.0 \text{ mol/L}$ . The films were subjected to ozonation for a set time interval prior to cycling.

Electrochromic performance during cycling was evaluated through *in situ* spectrophotometry at visible wavelengths, along with *ex situ* spectrophotometry in the solar range.

The electrochemical and optical data were evaluated with respect to electrochromic performance. Ozonation increased colouration efficiency in all studied electrolytes. Ozonation had a profound effect on the film's optical behaviour in LiPC, but only moderate in the aqueous electrolytes. The results indicate that the electrochromic performance of thin-film nickel vanadium oxide using Li-based organic electrolytes can be substantially improved by precharging in ozone atmosphere.

Handledare: Sara Green  
Extern handledare: Sophie von Kraemer  
Ämnesgranskare: Gunnar Niklasson  
Examinator: Nora Masszi  
UPTEC TVE 09011  
Sponsor: Chromogenics Sweden AB

# Contents

List of Figures	iii
List of Tables	v
Preface	vi
List of Symbols	vii
Abbreviations and Acronyms	viii
<b>1 Introduction</b>	<b>1</b>
1.1 Chromogenics	1
1.1.1 Electrochromism	2
1.2 The electrochromic device	2
1.2.1 Substrate layers	4
1.2.2 Optically transparent electrode layers	4
1.2.3 Anodic EC layer	5
1.2.4 Cathodic EC layer	5
1.2.5 Ion-conducting electrolytic laminate layer	5
1.3 Nickel oxide as anodic EC layer	5
1.4 ECD applications	6
1.5 Aim of this work	7
<b>2 Theory</b>	<b>9</b>
2.1 Nickel oxide phases	9
2.1.1 Nickel oxide	9
2.1.2 Properties of sputtered nickel oxide	11
2.1.3 Hydroxides and oxyhydroxides	11
2.1.4 Redox reaction scheme	13
2.2 Electrochemistry	15
2.2.1 Cyclic voltammetry	15
2.2.2 Electrolytes	16
2.2.3 Reference electrodes	20
2.3 The ozonation process	21
2.4 Material optics	23
2.4.1 Optics of a thin film	23
2.4.2 The colouration efficiency	23
2.5 Electrochromism	24

<b>3</b>	<b>Experimental method</b>	<b>27</b>
3.1	Materials	27
3.1.1	Some specifics on the sputtered product	27
3.1.2	Sample preparation	28
3.2	Ozonation	28
3.3	Cyclic voltammetry with <i>in situ</i> spectroscopy	29
3.3.1	Ambient atmosphere experimental considerations	32
3.3.2	Inert atmosphere experimental considerations	33
3.3.3	Calculated voltage drops	33
3.4	Optical characterisation in the solar range	35
<b>4</b>	<b>Results and discussion</b>	<b>37</b>
4.1	Ozonated films characterised optically	37
4.2	Ozonation followed by electrochemical cycling	41
4.2.1	Optical characterisation	48
4.2.2	Long-time experiment in LiPC	50
4.2.3	Film breakage on cycling in KOH-14	50
<b>5</b>	<b>Conclusions</b>	<b>53</b>
5.1	Outlook	54
<b>6</b>	<b>Sammanfattning</b>	<b>55</b>
	<b>References</b>	<b>57</b>
<b>A</b>	<b>Method</b>	<b>69</b>
A.1	Handling and storage	69
A.2	Preparation of electrolytes	70
A.2.1	Preparation of aqueous KOH, 1 mol/L	70
A.2.2	Preparation of aqueous KOH, 0.01 mol/L	70
A.2.3	Preparation of aqueous KOH, 0.1 mmol/L	70
A.2.4	Preparation of LiPC, 1 mol/L	71
A.3	Some experimental notes	71
<b>B</b>	<b>Analysis of primary data</b>	<b>73</b>
B.1	MATLAB M-functions	73
B.1.1	File formats	73
B.1.2	MultiplyOpticColumn	74
B.1.3	xyreader	74
B.1.4	xmultiyreader	74
B.1.5	qqreader	75
B.1.6	chargecollector	75
B.1.7	unfoldcv	75
B.1.8	foldoptic	76
B.1.9	GetArea	77
B.1.10	multiplyoncolumn	77
<b>C</b>	<b>Results</b>	<b>81</b>
	<b>Document notes</b>	<b>97</b>



# List of Figures

1.1	Electrochromic device, schematic . . . . .	3
2.1	Nickel's Pourbaix diagram in water . . . . .	10
2.2	Nickel vanadium oxide crystallite . . . . .	12
2.3	Bode reaction scheme in KOH(aq) . . . . .	14
2.4	Sawtooth potential . . . . .	16
2.5	A cyclic voltammogram explained . . . . .	17
2.6	Specific conductivity of KOH(aq) . . . . .	19
2.7	Propylene carbonate and lithium perchlorate . . . . .	20
2.8	Optics of a thin film in air . . . . .	23
3.1	Sample preparation photographed . . . . .	29
3.2	Geometry of a sheet and a film electrode . . . . .	30
3.3	The ozonation procedure . . . . .	31
3.4	OceanOptics spectrometer spectral profile . . . . .	31
3.5	Electrochemical <i>in situ</i> cells, photograph . . . . .	33
3.6	<i>In situ</i> electrochemical cell (KOH), to-scale drawing . . . . .	34
3.7	<i>In situ</i> electrochemical cell (LiPC), to-scale drawing . . . . .	35
3.8	Perkin Elmer $\lambda 9$ spectrophotometer . . . . .	36
4.1	Transmittance in the visible after ozonation . . . . .	39
4.2	Ozonation curves: transmittance vs ozonation time . . . . .	39
4.3	Reflectance spectra, solar, with ozonation series . . . . .	40
4.4	Bleaching charge vs transmittance . . . . .	41
4.5	CE per cycle . . . . .	42
4.6	CE <i>in situ</i> at cycle 10 . . . . .	43
4.7	Charge capacities at stable cycle . . . . .	43
4.8	Charge capacity per cycle . . . . .	44
4.9	Charge reversibility . . . . .	45
4.10	OCP per electrolyte and ozonation state . . . . .	46
4.11	KOH-14 CV & $T_{550}$ at stable cycle . . . . .	46
4.12	KOH-12 CV & $T_{550}$ at stable cycle . . . . .	47
4.13	LiPC CV & $T_{550}$ at stable cycle . . . . .	47
4.14	Optical modulation bands . . . . .	48
4.15	$T_b$ and $T_c$ per cycle . . . . .	49
4.16	$T_c$ during initial cycles . . . . .	49
4.17	Long-time cycling in LiPC, CV . . . . .	50
4.18	Long-time cycling in LiPC, <i>in situ</i> $T_{550}$ . . . . .	51

4.19	Film breakage in KOH, photographs . . . . .	52
5.1	Optical modulation bands . . . . .	53
6.1	Elektrom tunnfilmsanordning . . . . .	55
A.1	Sample storage system . . . . .	70
A.2	Mettler H18 balance . . . . .	71
C.1	Bleaching charge vs transmittance . . . . .	82
C.2	Charge capacity at stable cycles . . . . .	82
C.3	$T_b$ and $T_c$ per electrolyte . . . . .	83
C.4	Change in coloured-state transmittance . . . . .	84
C.5	Optical modulation in LiPC . . . . .	84
C.6	Optical modulation in KOH-14 . . . . .	85
C.7	Optical modulation in KOH-12 . . . . .	85
C.8	CE <i>in situ</i> in all electrolytes . . . . .	86
C.9	CE(T,R) <i>ex situ</i> in all electrolytes, visible range . . . . .	86
C.10	CE(T,R) <i>ex situ</i> all electrolytes, solar range . . . . .	86
C.11	CE(T) <i>ex situ</i> in all electrolytes . . . . .	87
C.12	CE(T) <i>ex situ</i> compared with CE <i>in situ</i> . . . . .	87
C.13	KOH-14 CV & $T_{550}$ at stable cycle . . . . .	88
C.14	KOH-12 CV & $T_{550}$ at stable cycle . . . . .	88
C.15	LiPC CV & $T_{550}$ at stable cycle . . . . .	88
C.16	CV & $T_{550}$ , NONOZ films in KOH-14 . . . . .	89
C.17	CV & $T_{550}$ , NONOZ films in KOH-14 . . . . .	89
C.18	CV & $T_{550}$ , NONOZ films in KOH-12 . . . . .	89
C.19	CV & $T_{550}$ , NONOZ films in LiPC . . . . .	90
C.20	CV & $T_{550}$ , OZ040 films in KOH-14 . . . . .	90
C.21	CV & $T_{550}$ , OZ040 films in KOH-12 . . . . .	90
C.22	CV & $T_{550}$ , OZ040 films in LiPC . . . . .	91
C.23	CV & $T_{550}$ , OZ120 films in KOH-14 . . . . .	91
C.24	CV & $T_{550}$ , OZ120 film in KOH-14 . . . . .	91
C.25	CV & $T_{550}$ , OZ120 films in KOH-12 . . . . .	92
C.26	CV & $T_{550}$ , OZ120 films in LiPC . . . . .	92
C.27	As-deposited film transmittance . . . . .	93
C.28	As-deposited solar transmission spectra . . . . .	94
C.29	Change in transmittance after storage . . . . .	94
C.30	Post-ozonation bleaching in air . . . . .	95

# List of Tables

3.1	Sheet properties . . . . .	28
3.2	Summarised experimental matrix . . . . .	32
3.3	Conversion between standard electrode potentials . . . . .	33
4.1	Optical transmittance for ozonated films . . . . .	38
A.1	Electrolyte solutions . . . . .	70
A.2	PE $\lambda 9$ spectrophotometer settings . . . . .	71
B.1	MultiplyOpticColumn.m . . . . .	74
B.2	xyreader.m . . . . .	75
B.3	xmultiyreader.m . . . . .	75
B.4	qqreader.m . . . . .	76
B.5	chargecollector.m . . . . .	76
B.6	unfoldcv.m . . . . .	77
B.7	foldoptic.m . . . . .	78
B.8	GetArea.m . . . . .	79
B.9	multiplyonecolumn.m . . . . .	79
C.1	As-deposited film transmittance . . . . .	93
C.2	Linear equations fit to post-ozonation bleaching in air . . . . .	95

# Preface

I believe that our achievements are not the result of our own efforts, but build on the efforts of many, contemporaries as well as predecessors.

I would like to acknowledge my supervisors Sara Green and Sophie von Kraemer and my professor Gunnar Niklasson for introducing me to this area of science. Before I came here, I knew almost nothing of electrochromism. This report is so much better thanks to you.

Although I have tried my best to keep errors out of this report, any errors, factual or conceptual, are those of the author himself.

I would like to present my deepest thanks to all the staff of the solid state physics department at the Ångström Laboratory, for their generous support and helpful advice during this project.

Uppsala, August 24  
*Taha Ahmed*

# List of Symbols

- $T_b$  Bleached-state optical transmittance (%), reported at 550 nm unless otherwise stated.
- $T_c$  Coloured-state optical transmittance (%), reported at 550 nm unless otherwise stated.
- $T_i$  Initial (on *in situ* experiment start) optical transmittance (%), reported at 550 nm unless otherwise stated.
- $T_{\text{asd}}$  Transmittance in the as-deposited state (%), reported at 550 nm unless otherwise stated.
- $T_{550}$  Optical transmittance at 550 nm (%).
- $d$  Thickness, or atomic interlayer distance (Å).
- $i$  Current (A).
- $j$  Current density (mA/cm<sup>2</sup>).
- $\nu$  Potential scan rate (mV/s).
- $Q_c$  Total amount of cathodic charge recorded within the potential window (mC).
- $Q_a$  Total amount of anodic charge recorded within the potential window (mC).

# Abbreviations and Acronyms

- KOH-14 Aqueous KOH(aq) electrolyte at pH 14,  $c(\text{K}^+) = 1.0 \text{ mol/L}$ .
- KOH-12 Aqueous KOH(aq) electrolyte at pH 12,  $c(\text{K}^+) = 10 \text{ mmol/L}$ .
- LiPC Li-based electrolyte,  $\text{LiClO}_4$ , dissolved in propylene carbonate (PC).  
 $c(\text{Li}^+) = 1.0 \text{ mol/L}$ .
- W. E. Working electrode of a three-electrode electrochemical cell.
- R. E. Reference electrode of a three-electrode electrochemical cell.
- C. E. Counter electrode of a three-electrode electrochemical cell.
- ITO Indium tin oxide,  $\text{Sn:In}_2\text{O}_3$ .
- PET Polyethylene terephthalate, a thermoplastic polyester resin.
- CE Colouration efficiency, in units of  $\text{cm}^2/\text{C}$  unless otherwise stated.
- R Optical reflectance. In units of percent (0 – 100%) unless otherwise stated.
- T Optical transmittance. In units of percent (0 – 100%) unless otherwise stated.
- asd As-deposited. A  $\text{Ni}_{1-x}\text{V}_x\text{O}_y\text{H}_z$  sheet or film in as-deposited condition.
- NONOZ A film in non-ozonated state (may have been electrochemically cycled).
- OZ040 A film in intermediately ozonated state (exposed to UV/ $\text{O}_3$  for 40 seconds).
- OZ120 A film in ozonated state (exposed to UV/ $\text{O}_3$  for 120 seconds).
- ECD Electrochromic device.
- OTE Optically transparent electrode.
- CV Cyclic voltammogram.
- OCP Open circuit potential.

# Introduction

There exists a whole range of materials which optical properties can be changed in a controlled manner. Such materials are called *chromogenic*, and are introduced below. A chromogenic material that changes its optical property in response to an applied electric potential is termed *electrochromic*.

This work concerns itself with thin films of nickel vanadium oxide, an electrochromic material, for application in electrochromic devices. Specifically, it studies the effect of *precharging* of the film by process of ozonation.

This chapter introduces such terms and concepts, necessary for understanding the process of electrochromic colouring. The **aim of this work** is specified in more detail before the end of the chapter.

## 1.1 Chromogenics

The term *chromogenics* is a broad descriptor used for all materials which *reversibly* change their optical properties (such as transmittance or reflectance) in response to an external stimulus. Chromogenic materials may also be described as *optical switching materials*, due to their ability to switch optical properties in a region of the spectrum, e.g., from low to high transmittance, or from low to high reflectance (or both, thus switching absorptance).

A multitude of chromogenic materials have been discovered, which change their optical properties in response to different external stimuli (physical effects), e.g., light (photochromics), temperature (thermochromics), ambient atmospheric chemistry (gasochromics), magnetism (magnetochromics), and electricity (electrochromics) [10, 49, 65]. Each technology has its advantages and drawbacks.

Not all the mentioned chromogenic technologies offer the same capabilities. For example, direct user control of the optical switching is difficult using photochromics; this technology is better suited to an automatic response to changes in the ambient environment. As such, the photochromic effect is used in self-darkening sunglass lenses that lower their transmittance in the visible region upon exposure to UV light (sunny outdoors environment) and revert to a clear state in the absence of UV light (indoors).

Electrochromics has attracted most of the attention within the chromogenics

field ever since the late 1960's when electrochromism of tungsten oxide,  $\text{WO}_3$ , was discovered by Deb [38].

The advantages of electrochromics over the other chromogenic technologies are the ability to control the optical switching by a small direct current, the ability to continuously vary the colouration degree, and the ability to hold at any colouration degree without supplying additional power ("open circuit memory").

During the 1980's much of the research in electrochromics was oriented towards display applications (watches, monitors, etc.) [72], and thus towards reflectance modulation. After a short and lost battle against the then emerging liquid crystal (LCD) technology, research was eventually focused on transmittance modulation for use as smart windows (for indoor light and glare control) and at the same time the need for an optically active counter-electrode compatible with  $\text{WO}_3$  became apparent.

### 1.1.1 Electrochromism

An electrochromic material is able to reversibly change its optical properties when a voltage is applied across it [55]. Electrochromism involves electroactive species (redox reactions), and is ultimately caused by an electron-transfer reaction at an electrode in a electrochemical cell [99].

Electrochromism is exhibited by a number of materials, both solid-state and in solution, inorganic and organic [72]. This report focuses on the electrochromism of inorganic oxide materials, specifically nickel oxide. Additionally, the optical property investigated is the broadband transmittance and reflectance in the visible spectrum, with some solar range experiments.

Depending on the mode of the electrochromism, a material is said to be either a *cathodic* or *anodic* electrochrome. An EC material that *colours* (darkens, becomes less transmittive) upon electron *insertion* is cathodic, and an EC material that *bleaches* (clears, becomes more transmittive) upon electron *insertion* is *anodic* [55]. An electrochromic material is thus *cycled* between bleached and coloured states by the insertion and extraction of electrons.

Electrochromism is displayed by the oxides of the transition metals, with the oxides of Cr, Mn, Fe, Co, Ni, Rh, and Ir anodically colouring, while the oxides of Ti, Nb, Mo, Ta, and W colour cathodically [55]. Vanadium oxide can colour both anodically and cathodically.

## 1.2 The electrochromic device

Ever since Deb [38] discovered that tungsten oxide exhibited cathodic electrochromism, ceramic electrochromic technology has been based on that oxide. This study, though, focuses on the electrochromic nickel oxide material. For readers interested in the electrochromism of tungsten oxide, I may point to excellent books by Granqvist [55] and Monk et al. [84], and the review article by Niklasson and Granqvist [87].

To construct an electrochromic device (ECD) the EC material needs to be incorporated in an electrical circuit comprising an electrochemical cell, and if the aim is a transmittance modulating device (such as for glazing), the constituting layers need to be optically transparent in the visible spectrum.

An ECD is built up of two redox couples [32], which in this specific design (Figure 1.1) are cathodically colouring  $\text{WO}_3$  and anodically colouring  $\text{NiVO}$ , joined by



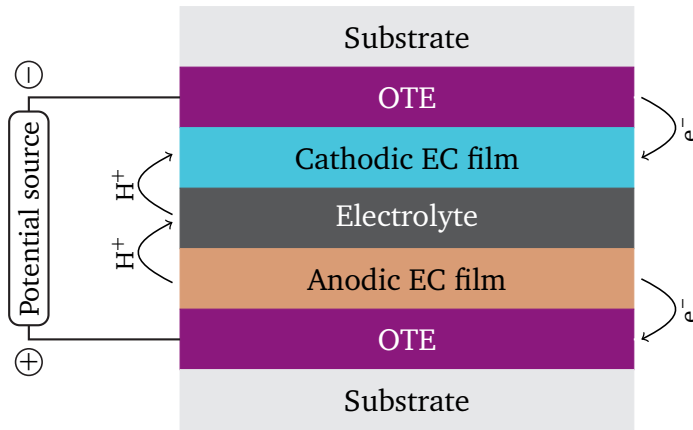


Figure 1.1: Schematic drawing of a transmissive electrochromic device (ECD). The substrate flexible polyester (PET) foil, which is optically transparent in the visible spectrum. The optically transparent electrode layers (OTE) consist of indium tin oxide ( $\text{Sn:In}_2\text{O}_3$ ), which is both optically transparent and electrically conductive. The electrochromic layers are mixed conductors, i.e., they transport both electrons and ions. The ion-conductive electrolyte layer is a polymer-based laminate. The arrows illustrate the direction of electron and cation flow during colouration (darkening) of the device. 🔍

an ion-conducting electrolytic laminate [13], all sandwiched between two flexible PET foils coated with an optically transparent electrode. This device design has been the focus of a lot of attention lately [7, 10, 87], mainly because the flexible substrate opens up the possibility of using roll-to-roll technology for inexpensive production [16, 57].

ECDs of this design have been extensively researched and tested, and have shown good contrast and good stability for thousands of cycles. The device works by applying a low electrical voltage (about 3 volts) across the microscale ceramic “sandwich”, which responds by darkening. Depending on the electronic control circuits attached, the ECD may darken continuously or in discrete stages. Electricity is only needed to change the state of the device, not to sustain a set level of transmittance (this is because the EC materials have open circuit memory).

If an ECD, constructed as in Figure 1.1, is short-circuited it will revert to its bleached state, retaining its primary function of light transmittance [99]. And with suitable electronic control circuits, the ECD bleaches on power loss, and is thus fail-safe.

From Figure 1.1 it is clear that the function of an ECD is similar to that of a likewise constructed battery; with the addition that this particular battery changes its optical transmittance depending on its state of charge. This battery analogy has been used earlier [10, 13, 32, 54], and only holds at an abstract level.

Just as the electrode capacities of a well designed battery need to match each other closely for the battery to perform optimally, so should the charge capacities of the anodic and cathodic EC materials match each other (with different signs).

The closer the electrode capacities of an ECD are matched, the wider the transmittance window [62]. Balancing of the charge capacities of the constituent EC

layers is done at device assembly, and is termed *precharging* the constituent layers. This step in device assembly and production has proven to be crucial for subsequent device operation [15].

In the following a short description of each layer of the ECD will be given, including data on health issues pertaining to the contained elements, and also mineral trading prices where possible. Regarding prices quoted below: please note that although prices are quoted per kilogram of pure metal in all cases for easy comparison, trading is usually done in much larger quantities.

### 1.2.1 Substrate layers

The substrate is a flexible foil of biaxially oriented semicrystalline polyethylene terephthalate (PET), a polymer resin of the polyester group. The biaxial stretching steps during production makes the film semicrystalline, which gives the film excellent dimensional stability and good optical transparency [97].

Residues of the inorganic catalyst used during PET polymerisation are present in most PET materials [103]. The previously cited reference states that approximately 90% of all PET production uses antimony trioxide ( $\text{Sb}_2\text{O}_3$ ), a potential carcinogen, and that the catalyst does leach from the finished product at detectable concentrations, but well below WHO guideline concentrations. Regarding PET for beverage containers, this is still clearly disturbing; regarding PET in ECDs or similar technologies, it is technically relevant to keep track of possible contaminants which may affect the system's performance. Although any effects from PET catalysts would seem unlikely, in my opinion.

Other inorganic catalysts are used for PET polymerisation, such as germanium, titanium or aluminium oxides [3, 48, 111]. Any one of them may eventually replace antimony trioxide.

### 1.2.2 Optically transparent electrode layers

The optically transparent electrode is a layer of indium tin oxide (ITO),  $\text{Sn}:\text{In}_2\text{O}_3$ .

Indium mineral deposits are scarce, and indium is mainly extracted as a by-product from zinc mining [109]. Worldwide annual production of indium is no more than a thousand tonnes [110], including recycled metal.

Indium prices rose abruptly a few years back with the expansion of the flat-panel market, and has since fluctuated around \$800 per kilogram In (at >99.9% purity) [110].

The other metal species of ITO is tin, primarily mined as stannate,  $\text{SnO}_2$ . Estimated world reserves are 11 million metric tonnes, and worldwide production (2008) was 333,000 tonnes [29]. Tin prices have fluctuated recently. Over the last five years (2004–2008) average price was \$13 per kg Sn, but 2008 saw a rise to \$22/kg on average [30]. Still much cheaper than indium, though.

ITO is primarily used as transparent electrode in liquid crystal displays and other flat-panel applications [110].

Due to the high cost of indium, alternative transparent conductors is a hot field of research. Some proposed alternatives (of which the news has come to Polacksbacken) are  $\text{ZnO}:\text{Al}$  (AZO) [10, 33],  $\text{TiO}_2:\text{Nb}$  [87], single-walled carbon nanotubes (SWNT) [63, 102, 115],  $\text{SnO}_2:\text{F}$  [56],  $\text{SnO}_2:\text{Sb}$  [109], and poly(3,4-ethylene dioxythiophene) (PEDOT) [109]. Of these, AZO stands out, being an *n*-type wide band gap semiconductor, with conductivity  $10^{-3}$  to  $10^{-4}$  S/cm (com-

parable to ITO), and possible to sputter deposit [10, 33]. SWNTs are also promising; researchers have demonstrated a production method from carbon dioxide gas [88] and scalable and continuous fabrication of SWNTs in a wet process [37], as well as production of transparent SWNTs for EC applications [63] even on flexible plastic substrates [102]. Nonetheless, ITO, along with  $\text{SnO}_2\text{:F}$  and AZO, are still the most used and widely studied transparent conductors among the oxides, according to Granqvist and Hultåker [56].

### 1.2.3 Anodic EC layer

In this study the anodic electrochrome consists of hydrated nickel vanadium oxide,  $\text{Ni}_{1-x}\text{V}_x\text{O}_y\text{H}_z$ .

Nickel is a metal of the iron group in the periodic table. Nickel is abundant, and the estimated world reserves are 130 million metric tonnes [70].

Prices are stable, with little fluctuation over the last five years. Average traded price during 2008 was \$21 per kg Ni [70].

Nickel is not harmless to the human physiology. Many studies have shown that both soluble and insoluble forms of nickel damage genetic material [85]. Despite that, low levels of nickel is widely present in air, water, food, and consumer products [85]. Occupational exposure to nickel occurs mainly by inhalation of dust particles and fumes or by dermal contact [85]. The most commonly reported adverse health effect associated with nickel exposure is contact dermatitis [1]. A cell-study by Fletcher et al. [45] indicates that the nickel(II) ion is the active agent in nickel toxicity, mutagenesis and carcinogenesis, irrespective of the nickel compound to which an organism is exposed. In that sense, soluble nickel compounds are more toxic than insoluble nickel compounds.

Data on the toxicity of vanadium pentoxide [2], indicates that the main route of exposure is to the respiratory tract, and even so its main effect is to irritate the mucus and cause extended coughing. Since  $\text{V}_2\text{O}_5$  is present in the nickel oxide film as a homogeneous solid phase, it is not expected to cause any health issues.

### 1.2.4 Cathodic EC layer

The cathodic EC layer is commonly a thin film of tungsten trioxide,  $\text{WO}_3$ . It is usually blue in its coloured state and colourless in its bleached state. Tungsten oxide for EC applications has been studied extensively, and detailed accounts on its properties can be found in [55].

This layer usually contributes with the majority of the electrochromic effect in the device. Tungsten oxide sells for around \$20 per kg in the commodities market.

### 1.2.5 Ion-conducting electrolytic laminate layer

Either one of two kinds of electrolytes are usually employed in ECDs. Laminated devices commonly employ a polymer, e.g., PMMA (polymethyl methacrylate) dissolved in a liquid electrolyte such as  $\text{LiClO}_4$ -propylene carbonate [24]. So called all-thin-film devices use solid inorganic ion conductors, such as  $\text{ZrO}_2$  [73].

### 1.3 On nickel oxide's suitability as anodic electrochrome layer

So far, the cathodic EC material of choice has been and remains tungsten oxide. Any anodic EC material is therefore chosen on the basis of how well it complements tungsten oxide, optically and electrochemically.

Nickel oxide possesses *anodic* electrochromic properties [108], which is complementary to the cathodic electrochromism of tungsten oxide.

Among the anodic EC oxides, nickel oxide has shown that it combines moderate cost with excellent optical properties [54], and that it works well electrochemically with  $\text{WO}_3$  [16]. The electroactive phases of the nickel oxide electrode are nickel hydroxides and oxyhydroxides, which are layered phases that allow for effective ion intercalation and deintercalation, which in turn leads to high colouration efficiencies [46].

Furthermore, the brown colour of nickel oxide in the coloured state complements the blue colour of tungsten oxide, producing a neutral gray colour for the device in the coloured state [6].

The problem with residual absorption of nickel oxide EC films in the bleached state (causing unwanted absorption below 400 nm), can be alleviated with the addition of Mg to the sputtering target, as shown by Avendaño et al. [5].

An important step in electrochromic device design is the *precharging* (adjustment of the charge capacity) of the nickel oxide layer, performed post-deposition by UV irradiation in the presence of air (*ozonation*), as described earlier by Azens et al. [15, 16]. Precharging increases the amount of nickel oxyhydroxide phase in the film.

The use of nickel oxide based electrodes is by no means restricted to electrochromics. Nickel hydroxide is used as a cathode material in NiCd and NiMH batteries [112], and shows promise as a supercapacitor material [76, 78].

### 1.4 ECD applications

Electrochromic technology is particularly suited for use in building envelopes, where it allows the inhabitants to maintain contact with the outside environment, while effectively controlling visible light and heat transfer through the building envelope [54], thus effectively reducing the building's energy cost [16]. EC technology in combination with PV (photovoltaic) technology could even make buildings into net energy producers [107].

A large scale project involves fitting existing building glazing with EC foil [42], which is a major undertaking, and probably needs government backing to be realised.

In electrochromic windows for architectural glazing the electrochromic five-layer "sandwich" is usually applied on the inside surface of the outermost glass pane of the window.

The current cost of electrochromic glass is ten times the cost of regular glass [17]. Obviously the cost has to decrease before the use of EC glass can become widespread. To my knowledge, three major glassmakers produce EC glass, namely: Saint-Gobain Sekurit [101], SAGE Electrochromics, Inc. [100], and Pilkington [41, 107]. They all employ inorganic tungsten-based EC electrodes, and counter electrodes of different materials.

Pilkington has reportedly fitted its Econtrol-Glas<sup>®</sup> EC glass to the southern

facade of a bank building in Dresden, Germany [107]. The glass features five tint levels.

The most widespread application of EC technology to date, is as auto-dimming rearview mirrors in automobiles, by Gentex Corp. [50]. The mirrors use organic electrochromes suspended in a layer that effectively modulates the reflectance of the mirror automatically (by photosensor).

Saint-Gobain Sekurit has produced an electrochromic variable transmittance glass sunroof for a convertible sports-car, the Ferrari 575M Superamerica, a luxury model produced in just 559 units. The Ferrari Superamerica was the first production car to include an electrochromic window [44].

There are many more examples of possible EC applications, including but not limited to: ski goggles [54], visors for MC helmets [54], public information displays [99] and thermal-exposure indicators for frozen foodstuff [99].

Clearly the most promising applications, both commercially and environmentally, are in building glazings and vehicle windows for light, glare and heat control.

## 1.5 Aim of this work

The objective of this work was to characterise flexible foil nickel vanadium oxide [14] optically with regard to ozonation [15], in KOH(aq) of different concentrations and in LiClO<sub>4</sub>+PC.

Since the purpose of the sputtered thin-film nickel oxide is to function as a counter electrode in an electrochromic device, there exists a need to activate it before device assembly.

It is well known that UV irradiation in air oxidises the sputtered film [13, 15]. Theoretical understanding of the ozonation mechanism is quite good, and can be represented by the papers of Avendaño et al. [9] and Bardé et al. [18].

The usage of ozone as an oxidating agent is widespread, with applications in the water treatment industry [77, 114], municipal waste management [113], and even in a new technology called “cold” pasteurisation [92], among many other uses.

This project aims at studying the electrochromic behaviour of oxidised nickel oxide thin films. A small, research-scale UV irradiation chamber was used to perform the ozonation experiments.

There has been only one previously published study on the ozonation of nickel vanadium oxide on a flexible PET substrate, namely that of Azens et al. [14]. That study did not include data on electrochemical cycling after ozonation, but other reports has [15], although they used glass substrates. The work presented in this report on post-ozonation electrochemical cycling in LiPC complements the ongoing research by Green et al. [59] on this electrolyte.



# Theory

We start by describing the structural chemistry of the involved nickel oxide phases, which basically is redox intercalation chemistry. Next, general electrochemistry with an emphasis on cyclic voltammetry is presented, along with the theory governing electrolytes and electrodes. Section 2.3 deals with ozone and its known effect on nickel oxide films. The subsequent section presents basic solid state optics. The final section elaborates on the cause of electrochromism.

## 2.1 Nickel oxides, hydroxides and oxyhydroxides

This section describes the structural chemistry of the electrochromic nickel oxide film and the phases it contains.

### 2.1.1 Nickel oxide

Nickel is a  $3d$  transition metal, in the iron group (group VIII) of the periodic table.

Nickel oxide has a cubic unit cell, with space group  $Fm\bar{3}m$  (225). The cell parameter has been reported with slightly different values by different authors, as,  $4.1684 \text{ \AA}$  [28, 116],  $4.176 \pm 0.001 \text{ \AA}$  [86],  $4.1762 \text{ \AA}$  [68],  $4.180 \text{ \AA}$  [27, 106],  $4.2 \text{ \AA}$  [43],  $4.24 \text{ \AA}$  [118], and as  $4.27 \text{ \AA}$  [119]. The variation of the cell parameter can be attributed to the inherent non-perfect stoichiometry of nickel oxide; the material will always exhibit some oxygen excess [69]. The oxygen excess produces  $\text{Ni}^{2+}$  vacancies which are compensated by the creation of holes on two  $\text{Ni}^{2+}$  sites [11]. Since there is limited interstitial space to accommodate the excess oxygen in the bulk crystalline NiO-type structure, the crystal surface becomes enriched in oxygen, which effectively increases the cell parameter. As a remark, we note that closely stoichiometric NiO appears green, and that nickel deficient  $\text{Ni}_{1-x}\text{O}$  appears black since the effect of the excess oxygen is to increase the magnitude of the continuous background absorption [86].

The chemical formula for nickel oxide should be written  $\text{Ni}_{1-x}\text{O}$  [69], reflecting the material's  $p$ -type semiconducting nature [7]. Nickel oxide has a room-temperature band gap  $3.6\text{--}4.0 \text{ eV}$  [71, 83, 95] and conductivity  $10^{-13} \text{ S/cm}$  [83].

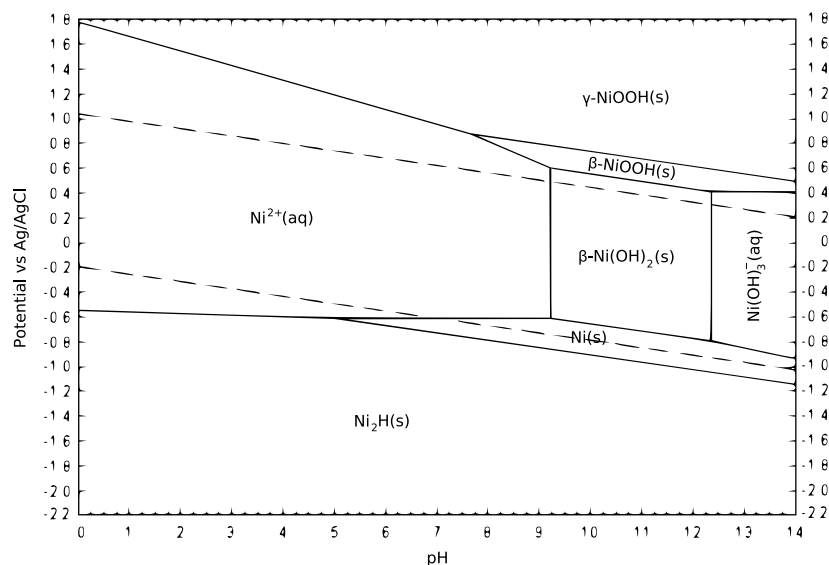


Figure 2.1: Pourbaix diagram for nickel at 25 °C and  $[\text{Ni}(\text{aq})]_{\text{tot}} = 10^{-6}$  mol/g in water. The dashed lines indicate water's thermodynamic stability area. In a Pourbaix diagram, regions related by non-redox reactions are separated by vertical lines; e.g.,  $\text{Ni}^{2+}(\text{aq}) \rightleftharpoons \beta\text{-Ni}(\text{OH})_2$  (no change of oxidation states). Regions which are related by redox reactions are separated by horizontal lines, e.g.,  $\text{Ni}_2\text{H}(\text{s}) \rightleftharpoons \text{Ni}^{2+}(\text{aq})$ . Sloping lines indicate that the reaction is both oxidation state and pH dependent. The Pourbaix diagram clearly shows that nickel oxides, hydroxides and oxyhydroxides are unstable and dissolve in acidic solutions. This diagram was adapted from Beverskog and Puigdomenech [22].

Nickel oxide forms the bulk of the sputtered phase, and recent papers [25, 87] have submitted that it participates in the electrochromic reaction by acting as a “proton reservoir” (Equation 2.1 on page 13).

In a Pourbaix diagram, the regions indicate the conditions of pH and potential under which a species is thermodynamically stable [104]. A redox reaction is any reaction wherein a participant species undergoes a change in oxidation state. The Pourbaix diagram shows that nickel oxide is thermodynamically stable in alkaline solutions, but unstable in acidic. The same holds true for the nickel hydroxides and oxyhydroxides. This instability versus acids limits the usability of nickel-based anodic EC materials, since the most common cathodic EC material,  $\text{WO}_3$ , is thermodynamically stable in acidic solutions but unstable in alkaline (the opposite of nickel oxide) [87]. One way to address this problem was demonstrated by Azens and Granqvist [13], who applied a thin, dense layer of tungsten oxide *on top* of the nickel oxide, thus eliminating its contact with the electrolyte.

As a complement to the Pourbaix diagram, Avendaño et al. [8] reported that Yoon and Pyun [120] found by IR spectroscopy on electrodeposited samples that  $\beta\text{-Ni}(\text{OH})_2$  was stable at potentials below 0.15 V, that  $\alpha\text{-Ni}(\text{OH})_2$  was stable for  $0.15 < E < 0.27$ , that  $\beta\text{-NiOOH}$  was stable above 0.30 V, and that  $\gamma\text{-NiOOH}$  was stable above 0.34 V (all potentials versus Ag/AgCl and in 1 M KOH). IR spectroscopy by Avendaño et al. [8] did not contradict these values. These stability



ranges indicate that  $\alpha$ -Ni(OH)<sub>2</sub>, which is not reported in the Pourbaix diagram (Figure 2.1) resides between the  $\beta$ -Ni(OH)<sub>2</sub> and  $\beta$ -NiOOH regions.

### 2.1.2 Properties of sputtered nickel oxide

For technical reasons pertaining to the dc magnetron sputtering process, it is strongly advantageous to use a non-magnetic sputtering target [6, 12, 15, 59]. For that purpose, the widely available non-magnetic alloy Ni<sub>0.93</sub>V<sub>0.07</sub> is used [6, 9, 34, 58, 87].

It has been shown by X-ray spectroscopy that nickel and vanadium form a mixed-oxide phase in the film [10, 11, 16]; that vanadium is distributed without clustering and substitutes nickel ions [9], and that vanadium is not electrochemically active upon colouration [11]. The material changes structure slightly on vanadium incorporation, mainly expressed by less covalent Ni–O bonding in nickel vanadium oxide [9]. The major effect of vanadium incorporation into the film is an increase of the residual absorption in the bleached state (bleached state transmittance decreases) [6].

Although the amount of vanadium in the sputtering target is fixed, the vanadium concentration in the nickel oxide film may vary depending on sputtering conditions. Thus the following chemical formulas have been reported for magnetron sputtered nickel vanadium oxide films: Ni<sub>0.92</sub>V<sub>0.08</sub>O<sub>1.43</sub>H<sub>0.55</sub> [74], Ni<sub>0.91</sub>V<sub>0.09</sub>O<sub>1.37</sub> [11], and Ni<sub>0.90-0.95</sub>V<sub>0.05-0.10</sub>O<sub>1.45-1.75</sub> [8]. These values were obtained through RBS (Rutherford back scattering) experiments.

The cited formulas give V/Ni ratios of 0.087, 0.099, and 0.053–0.11. They give O/Ni ratios of 1.55, 1.51, and 1.53–1.94. These values are rather high compared to the more reasonable O/Ni ratio of 1–1.3 observed by Green et al. [59]. In any case, the point is that the film contains oxygen in excess.

The role of vanadium in the electrochromic process has been studied by several workers. XPS (X-ray photoelectron spectroscopy) observations by Avendaño et al. [11] indicate that the vanadium ions stay in the bulk nickel oxide and that the electrochromically colouring grain surface layer is vanadium free (*cf.* Figure 2.2). Thus any vanadium valency changes upon cycling or ozonation are not expected to play any significant role in the electrochromism of the films [87]. Vanadium ions substitute nickel ions in the NiO-type structure without any evidence for clustering, as reported by Avendaño et al. [9].

The vanadium does unfortunately increase the optical absorbance of the film in the bleached state [6], especially at wavelengths below 400 nm. However, it does not affect the coloured state absorbance.

Several workers have reported that powder X-ray diffraction of nickel oxide-based thin films detect only cubic nickel oxide, although nickel hydroxide and oxyhydroxide phases could be identified with surface sensitive X-ray spectroscopy techniques, such as XPS [16, 87]. The fact that the surface layers adapt their own structure indicates that their thickness is at least a few monolayers thick [21]. In addition, Avendaño et al. [11] observed that the coloured Ni<sub>2</sub>O<sub>3</sub> phase exists as a “bridge” between the cubic NiO and the hexagonal hydroxide and oxyhydroxide phases, when the film is in its coloured state.

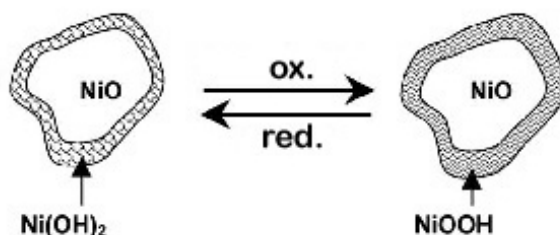


Figure 2.2: A nickel vanadium oxide crystallite’s radial structure, with the surface, consisting of oxygen-rich hydroxide and oxyhydroxide phases, marked gray, and the bulk, consisting mainly of nickel vanadium oxide, shown in a white colour. The electrochromic reactions occur at the accessible oxygen-rich grain surfaces. This illustration was adapted from Bouessay et al. [25].

### 2.1.3 Hydroxides and oxyhydroxides — surface layer species

A common feature shared among all the nickel hydroxides and oxyhydroxides are the layered structure, with octahedrally coordinated nickel at the center of the layers and no hydrogen bonding between adjacent layers of OH groups [91].

These layers are stacked up along the  $c$  axis, with the O–H bonds parallel to it. The  $c$  parameter equals the interlayer distance, and the  $a$  parameter equals the nickel-nickel distance within a layer.

In the next four subsections, structural characteristics for the two hydroxide and the two oxyhydroxide phases are described based on literature data.

#### $\beta$ -Ni(OH)<sub>2</sub> properties

$\beta$ -Ni(OH)<sub>2</sub> has a layered brucite structure [39, 53] and has space group  $P\bar{3}m1$  (164) with a hexagonal unit cell [18, 39, 91]. Unit cell parameters are  $a = 3.126 \text{ \AA}$  and  $c = 4.605 \text{ \AA}$  [39, 91, 105]. Terminal hydroxyl ions are not hydrogen bonded [123], which indicates the absence of intercalated water molecules.

$\beta$ -Ni(OH)<sub>2</sub> is a  $p$ -type semiconductor with a band gap 3.6–3.9 eV [31], and an electronic conductivity on the order of  $10^{-11} \text{ S/cm}$  [87]. Nickel’s oxidation state lies between 2.0–2.2 [112].

I noted with interest the article by Xing et al. [117], which submitted a BET surface area  $431.7 \text{ m}^2/\text{g}$  for a mesoporous, highly crystalline  $\beta$ -Ni(OH)<sub>2</sub>. Their material was not sputtered, but their recorded cyclic voltammograms look very similar to mine and in addition the same scan rate was used. A surface area of that magnitude would put this material ahead of many zeolites in terms of internal surface area.

#### $\alpha$ -Ni(OH)<sub>2</sub> properties

$\alpha$ -Ni(OH)<sub>2</sub> belongs to space group  $P\bar{3}m1$  (164) [18, 39]. Varying cell parameters have been reported in the literature, the most frequently occurring seems to be  $a = 5.34 \text{ \AA}$ ,  $c = 7.60 \text{ \AA}$  [18, 39, 66]. The layer structure is turbostratic (with random rotations along the  $c$  axis) and supports intercalated water molecules (water which is hydrogen-bonded to the terminal hydroxyl groups on the layer surfaces) [91].

The turbostratic layer structure has led some authors to describe the structure as amorphous [53].

Nickel's oxidation state lies between 2.0–2.2 [112].

### $\beta$ -NiOOH properties

$\beta$ -NiOOH has a well-ordered, layered brucite structure [39]. Reported unit cell parameters vary slightly, with Dittrich et al. [39], Oliva et al. [91], Singh [105] reporting  $a \approx 2.82$  Å, while Bardé et al. [18] reports  $a = 2.41$  Å. The inter-layer distance is reported as  $c = 4.83$  Å [18],  $c = 4.84$  Å [105],  $c = 4.85$  Å [39, 91], and as  $c = 4.6$  Å [66]. The majority seem to agree on  $a = 2.82$  Å and  $c = 4.84$  Å, which makes  $\beta$ -NiOOH layers only marginally more separated than  $\beta$ -Ni(OH)<sub>2</sub>. The shorter nickel-nickel distance increases orbital hybridisation, which is reflected in the increased electronic conductivity  $10^{-7}$  S/cm and the decreased band gap 1.7–1.8 eV [31, 87] compared to  $\beta$ -Ni(OH)<sub>2</sub>.

$\beta$ -NiOOH is an  $n$ -type semiconductor. Nickel's oxidation state is 3 [18, 112].

IR spectra displayed the characteristic hydrogen-bonded OH band [123], which points to the presence of intercalated water molecules.

### $\gamma$ -NiOOH properties

$\gamma$ -NiOOH crystallises poorly in the hexagonal or possibly the rhombohedral system [39]. Space group is unknown. Unit cell parameters  $a = 2.82$  Å,  $c = 6.9$ – $7.0$  Å [18, 105]. The wide interlayer space intercalates alkali ions and water molecules [91]. The oxidation state of nickel is higher than three [75], more precisely observed to lie between 3.5–3.7 [18, 19, 105, 112].

#### 2.1.4 Redox reaction scheme

We have seen that Ni(OH)<sub>2</sub> exists as two structural modifications, called  $\alpha$  and  $\beta$ . The  $\alpha$ -Ni(OH)<sub>2</sub> contains intercalated water in its wide interlayers, and stabilises by *dehydrating* to the more stable  $\beta$ -Ni(OH)<sub>2</sub> on standing in alkaline solution [120]. In a similar fashion, NiOOH exists as two structural modifications, called  $\beta$  and  $\gamma$ . The  $\gamma$ -NiOOH can be formed on severe charging (oxidation) in KOH.

Together with the bulk NiO phase (which is bleached), and the coloured Ni<sub>2</sub>O<sub>3</sub> phase, these phases form the system which governs the electrochromic colouration and bleaching of nickel oxide-based films. Most previous studies on the colouration mechanism of nickel oxide dealt with cation intercalation; H<sup>+</sup> in particular. Only a few studied lithium ion intercalation [20, 35, 94] and only a few attempts [9, 18] have so far been made at explaining the mechanism of colouration on ozone exposure.

In our description of the electrochromic reactions below, I mainly describe reactions taking place at what is known as steady state conditions. It has been shown by Bouessay et al. [25] and others which I have not mentioned, that the electrochromic reaction proceeds through three stages, namely *activation*, *steady state* and *degradation*. Some authors name the initial stage *stabilisation*, the intended meaning is the same. Stabilisation occurs during the initial electrochemical switching cycles, and usually includes the irreversible reaction wherein oxygen-rich surface species are oxidised to oxyhydroxides [12].

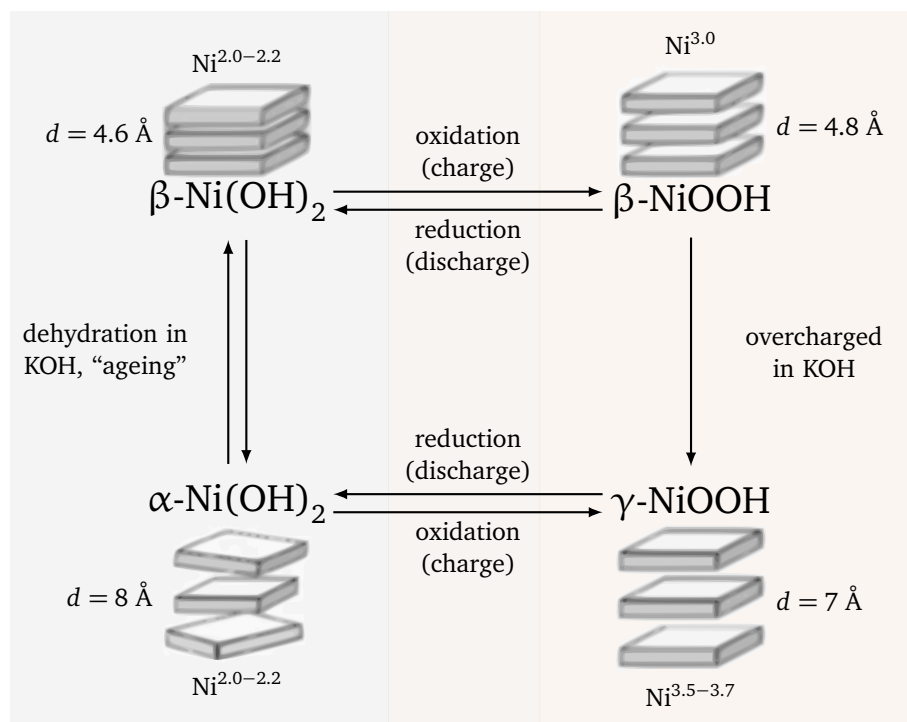
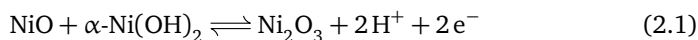
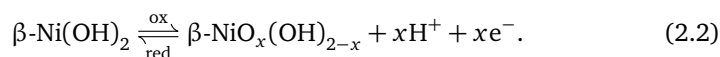


Figure 2.3: Conversion scheme for nickel hydroxide and oxyhydroxide phases during electrochemical cycling in KOH, following the scheme originally proposed by Bode et al. [23], and in similar form by [12, 18, 25, 53, 61, 87, 112]. Inter-layer distances,  $d$ , and nickel oxidation states as reported by Wehrens-Dijksma and Notten [112]. Left-hand species are bleached (low nickel oxidation state), and right-hand species are coloured (high nickel oxidation state). Equation 2.1 complements these reactions by including NiO and Ni<sub>2</sub>O<sub>3</sub>.

Equation 2.1 [11], shows how the bulk NiO phase can participate in the (steady state) electrochromic reaction. Bouessay et al. [25] described the NiO as “a reservoir of electrochemically active phase.”



The electrochemical cycling between  $\beta\text{-Ni(OH)}_2$  and  $\beta\text{-NiOOH}$  is a heterogeneous reaction [91] that takes place by phase boundary movement [96], and not through diffusion in the homogeneous phase. This is supported by the lack of any observations of a continuous variation of cell parameters during cycling. The expansion of the interlayer spacing is caused/triggered by water intercalation [47]. The  $\beta\text{-}\beta$  reaction can be generalised and written as [55]:



$x$  is normally one or very close to one, which makes this a one-electron transfer process.

The  $\beta\text{-}\beta$  reaction is simple, straight-forward, and easy to grasp conceptually. And on top of that, it is *the* reaction employed in all battery nickel hydroxide

electrodes, since it involves the least amount of shrinkage and expansion on cycling [91]. From the Bode scheme (Figure 2.3) it is clear that this is not the only possible colouration mechanism.

Indeed, by using GITT (galvanostatic intermittent titration technique) to determine the proton diffusion coefficient during ion insertion and extraction, Avendaño et al. [8] showed that the ion extraction involves two phase transitions, corresponding to a  $\beta\text{-Ni(OH)}_2 \rightleftharpoons \alpha\text{-Ni(OH)}_2$  transition at  $-0.1$  V vs Ag/AgCl followed by a  $\alpha\text{-Ni(OH)}_2 \rightleftharpoons \gamma\text{-NiOOH}$  transition at  $0.23$  V vs Ag/AgCl. Colouration occurred at the second phase transition.

Electrochemical cycling will eventually cause degradation of the film. This is not hard to understand for  $\alpha\text{-Ni(OH)}_2$  to  $\gamma\text{-NiOOH}$  cycling, where the mechanical stress alone may cause breaking. For  $\beta\text{-Ni(OH)}_2$  to  $\beta\text{-NiOOH}$  cycling, Bouessay et al. [25] suggests that the degradation is caused by process of *self-discharge and partial dissolution* of the oxidised phase. The self-discharge results from the spontaneous reduction of  $\beta\text{-NiOOH}$  to  $\beta\text{-Ni(OH)}_2$  at lower potentials, since  $\beta\text{-NiOOH}$  is less thermodynamically stable than  $\beta\text{-Ni(OH)}_2$ . The oxidised phase may also partially dissolve into the electrolyte solution, and since the solution volume is usually large the dissolution reaction is far from equilibrium and recrystallisation will not occur spontaneously.

Such degradation processes affect the reversibility of the charge capacity. For example, if part of the oxidised phase is dissolved into solution during the anodic sweep, and not somehow restituted during the subsequent cathodic sweep, then the material has essentially lost some of its electroactive phase. This translates into a reduced charge capacity.

As it happens, no such decrease of the charge capacity occurred [25], although the degradation processes were still present. This peculiarity has been attributed to the ability of the bulk NiO phase to form new active phase, e.g., as in Equation 2.1. In conclusion, it appears that the electrochromic colouration process is flanked by an ongoing competition between degradation processes and regeneration processes in KOH(aq).

## 2.2 Electrochemistry

A very broad definition of electrochemistry is given by Crow [36]: “electrochemistry is concerned with charges and with their movement and transfer from one medium to another.” The ultimate unit of charge is that carried by the electron.

Electrochemistry may be divided into different branches, each dealing with electron transfer across a particular *interface* (boundary between two media). The largest branch of electrochemistry is concerned with the exchange of electrons between electronic conductors (usually termed *electrodes*) and species in solution within which that electrode is placed [36]. That description fits the basic elements of an *electrochemical cell*.

Actually, an electrochemical cell consists of two electrodes in contact with an electrolytic solution and joined by an external electrical circuit, which is also the basic configuration of an ECD. An electrochemical cell may either produce electricity, and is then termed a *galvanic cell*, or consume electricity, and is then termed an *electrolytic cell* [4].

We will not describe basic electrochemistry in much detail here, but quickly move on to the technique of cyclic voltammetry. Readers interested in general

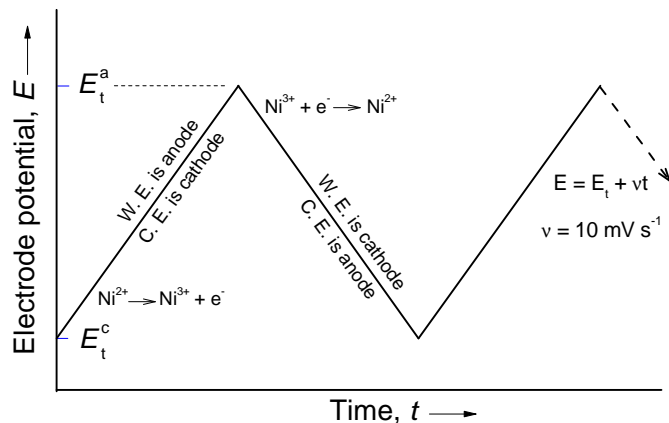


Figure 2.4: In cyclic voltammetry experiments a potential shaped as in the figure is applied on the working electrode, while the current is measured. The main characteristics of this symmetric sawtooth waveform (and thus of any CV experiment) is the negative and positive turn-round potentials,  $E_t^c$  and  $E_t^a$ , and the rate of change of the potential,  $v$  (the slope of the curve). 🔍

electrochemistry may find *Electrochemistry* by Hamann et al. [60] useful.

### 2.2.1 Cyclic voltammetry

In this technique, the potential on the working electrode is continuously varied between an upper and a lower limit as shown in Figure 2.4, with the resulting current being simultaneously detected and recorded (Figure 2.5). The applied potential is usually generated with a function generator, integrated into a potentiostat which also detects and records the current [36, 60].

The current is recorded versus applied potential (at the reference electrode), but since the potential is varied as a linear function of time, the current response could just as well be reported as current versus time [93].

The area of the working electrode which is immersed into the electrolytic solution is directly proportional to the recorded current. To make all reported cyclic voltammograms comparable, all CVs are plotted as *current density* versus potential. Current density is simply the primary recorded current divided by the immersed electrode surface area.

The integrated area under the CV in the cathodic and anodic half-cycle, corresponds to the cathodic and anodic *charge capacity*, respectively. The charge capacity is the effective intercalated charge that is reversibly transferred upon cycling

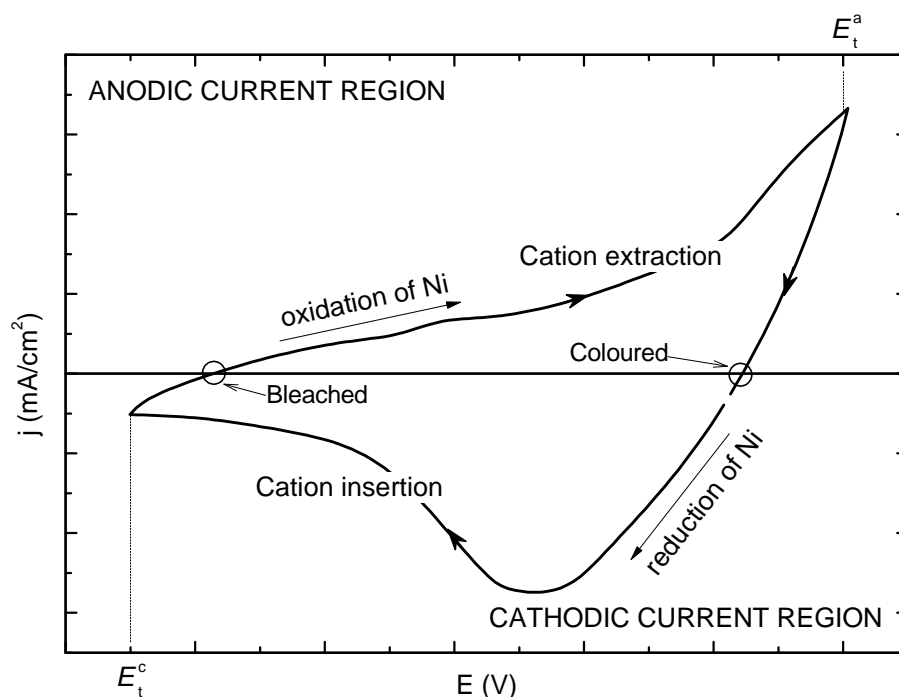


Figure 2.5: The resulting current from one of my experiments after the application of a sawtooth potential. The arrows denote the scan direction. From this plot, it can be seen that any CV consists of two half-cycles, or sweeps. During the reverse sweep (bottom half) the recorded current is negative and the half-cycle is termed *cathodic*. During the forward sweep the recorded current is positive and the half-cycle is termed *anodic*. The area covered by the curve in each half-cycle is the cathodic and anodic *charge capacity*, respectively. For a reversible reaction they should be equal. 🔍

[12].

$$\begin{aligned}
 Q_{\text{anodic}} &= \int_{E_c}^{E_a} j dE \approx \sum j \Delta E \\
 Q_{\text{cathodic}} &= \int_{E_a}^{E_c} -j dE \approx \sum -j \Delta E
 \end{aligned}
 \tag{2.3}$$

### 2.2.2 Electrolytes

Electrolytes are species giving rise to ions (by dissociation in solution) to a greater or lesser extent, strong electrolytes being completely ionised and weak electrolytes only to a lesser extent [36]. When the electrolyte is dissolved in a *solvent*, the resultant *solution* is termed an *electrolytic solution*, but it is commonly referred to as just *electrolyte*, which is not formally correct but the practice is widespread.

### On the choice of electrolytes

Based mainly on the work of Avendaño Soto [12] and unpublished and published work by Green et al. [59], potassium hydroxide in water (at different concentrations) and lithium perchlorate in propylene carbonate were selected, since KOH(aq) is without dispute the *de facto* reference electrolytic solution within the field of electrochromics, and LiClO<sub>4</sub>(PC) was chosen because it approximates the behaviour of more complex, organic Li-based electrolytes quite well.

### Resistance in an electrolytic solution

Ohm's law states the fundamental relationship between potential, current and resistance.

$$E = iR \quad (2.4)$$

$E$  is the electric potential (V),  $i$  is the current (A), and  $R$  is the resistance ( $\Omega$ ).

The resistance of a portion of an electrolyte solution may be defined in the same way as for a metallic conductor,

$$R = \rho \left( \frac{l}{A} \right) \quad (2.5)$$

$\rho$  being the resistivity and  $l$  and  $A$  the length (cm) and area (cm<sup>2</sup>) respectively of the portion of solution studied.  $G = 1/R$  is known as the conductance of the material.

The reciprocal of resistivity  $\rho$ , is known as the conductivity  $\kappa$  (S cm<sup>-1</sup>).

$$\kappa = \frac{1}{\rho} = \frac{l}{RA} \quad (2.6)$$

By inserting Equation 2.6 into 2.5, we get

$$R = \left( \frac{l}{A} \right) \left( \frac{1}{\kappa} \right) \quad (2.7)$$

from which the so-called cell constant ( $\kappa_{\text{cell}} = \kappa R$ ) can be calculated if the resistance is measured using a standard electrolyte.

Equation 2.7 can be inserted into Ohm's law, which gives

$$E = i \left( \frac{l}{A} \right) \left( \frac{1}{\kappa} \right). \quad (2.8)$$

And since we are particularly bright students, we recognize that  $i/A$  equals the quantity known as *current density*,  $j$ . So, we simplify the previous expression and write

$$E = j \frac{l}{\kappa} \quad (2.9)$$

which gives the voltage drop  $E$  from the experimentally measured current density  $j$  and the already known specific conductivity of the electrolyte  $\kappa$ .



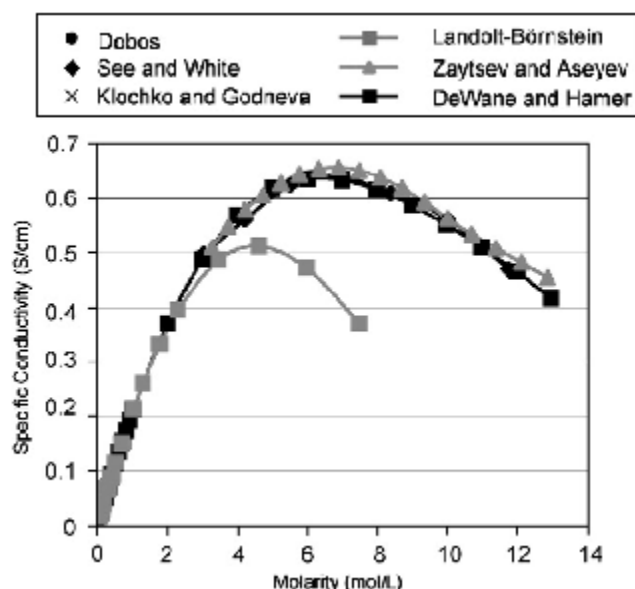


Figure 2.6: Specific conductivity of KOH(aq) vs molarity at 25 °C, from six different sources. Reproduced from Gilliam et al. [52].

### Potassium hydroxide in water

KOH(aq) is a widely used and studied electrolytic solution within the whole field of electrochemistry.

Thin film nickel oxide-based electrodes have been extensively studied in KOH(aq), and most of the mechanistic understanding of the electrode processes have been developed for this electrolyte. From that viewpoint, its inclusion into the experimental matrix was essentially mandatory.

Potassium hydroxide dissolved in water makes a strongly alkaline and protic electrolytic solution [59]. The alkalinity (high pH) makes the solution corrosive to glass and other materials, but at the same time very conductive.

The specific conductivity of KOH(aq) (over a molarity range of 0 – 12 mol/L at temperatures between 0–100 °C) has been reviewed by Gilliam et al. [52]. At 25 °C the specific conductivity increases with increasing molarity up to ~7 M, after which the specific conductivity decreases again (see Figure 2.6).

At 25 °C, the calculated specific conductivity [52] of KOH(aq) at a concentration 1.0 mol/L is  $\kappa = 0.2153$  S/cm. At a concentration  $1 \cdot 10^{-2}$  mol/L it is  $\kappa = 0.00243$  S/cm. The specific conductivity shows an almost linear decrease with concentration within this concentration range (concentration decreased a factor 100, specific conductivity decreased a factor 89).

Although water as a solvent works fine in the laboratory, it is not a good solvent for electrochemical devices because of its narrow potential window [26], which is limited by the hydrogen evolution potential at  $-0.623$  V vs Ag/AgCl and the oxygen evolution potential at  $+0.607$  V vs Ag/AgCl.

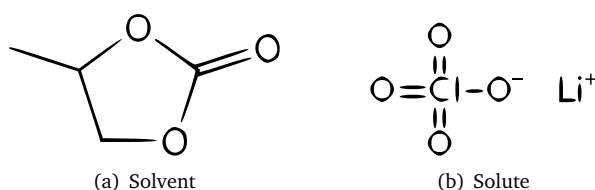


Figure 2.7: Chemical structure of (a) propylene carbonate and (b) lithium perchlorate. Propylene carbonate is a dipolar aprotic cyclic ester, and forms a transparent, odourless and colourless liquid at room temperature. Lithium perchlorate is a white, grainy solid.

### Lithium perchlorate in propylene carbonate, LiClO<sub>4</sub>(PC)

LiClO<sub>4</sub>(PC), or LiPC for short, consists of LiClO<sub>4</sub> electrolyte dissolved in propylene carbonate (see Figure 2.7). Propylene carbonate is a component of the electrolyte for lithium batteries [94], either alone or as a mixture with other solvents.

Lithium perchlorate is a strong electrolyte (ionises completely in solution) with good solubility in both aqueous and organic solvents. It is stable with regards to both electrochemical oxidation and reduction within wide limits.

Propylene carbonate (PC) is very good at solvating cations due to the partial negative charge localised at the carbonyl group. The partial positive charge is less localised. Propylene carbonate decomposes into carbon dioxide and propylene glycol on reaction with water. PC offers a wide potential window, with oxidation of PC starting at +4.5 V vs Li/Li<sup>+</sup>, and reduction of PC below +1 V vs Li/Li<sup>+</sup> [94].

Values for the specific conductivity of LiPC were not abundantly available, and the only relevant data I could find was presented as not too detailed plots. With that said, these are the values I found. Bohnke et al. [24] reported  $\kappa \approx 0.45$  S/m at 22°C. Georén and Lindbergh [51] reported  $\kappa \approx 0.50$  S/m at 25°C.

### 2.2.3 Reference electrodes

The electrochemical experiments of this project employed either one of two reference electrodes, namely the silver-silver chloride electrode for aqueous-based systems, and the lithium electrode for systems using the LiClO<sub>4</sub> electrolyte.

#### Silver-silver chloride electrode

The Ag/AgCl electrode is a secondary reference electrode (the primary being the standard hydrogen electrode, SHE) of the second kind [36, 60]. Reference electrodes of the second kind are built up as follows: a metal M is placed in contact with a sparingly soluble salt of M<sup>z+</sup>, all placed in a solution containing a strongly ionised salt with a common anion [36].

The operation of the silver-silver chloride electrode is dependent upon the reaction



which is the solubility of the virtually insoluble silver chloride salt. We can write the solubility product  $K_s$ ,

$$K_s^{\text{AgCl}} = a_{\text{Ag}^+} \cdot a_{\text{Cl}^-} \quad (2.11)$$

(we use activity for stringency, for practical concerns it can be replaced by concentration in most cases). We can then write the equilibrium potential of the silver-silver chloride half-cell, consisting of  $\text{Ag}|\text{AgCl}|\text{Cl}^-$ , as

$$E^{\text{Cl}^-|\text{AgCl}|\text{Ag}} = E^{0,\text{Ag}^+|\text{Ag}} + \frac{RT}{F} \ln K_s^{\text{AgCl}} - \frac{RT}{F} \ln a_{\text{Cl}^-}. \quad (2.12)$$

The terms  $E^{0,\text{Ag}^+|\text{Ag}} + \frac{RT}{F} \ln K_s^{\text{AgCl}}$  are the same as the standard potential of the silver-silver chloride electrode,

$$E^{0,\text{Cl}^-|\text{AgCl}|\text{Ag}} = E^{0,\text{Ag}^+|\text{Ag}} + \frac{RT}{F} \ln K_s^{\text{AgCl}} \quad (2.13)$$

which can be calculated since  $E^{0,\text{Ag}^+|\text{Ag}}$  is known (it is +0.7996 V vs SHE) and the solubility product  $K_s^{\text{AgCl}}$  has the value  $1.78 \cdot 10^{-10}$  [60].

That finally gives us the expression

$$E^{\text{Cl}^-|\text{AgCl}|\text{Ag}} = E^{0,\text{Cl}^-|\text{AgCl}|\text{Ag}} - \frac{RT}{F} \ln a_{\text{Cl}^-} \quad (2.14)$$

which shows that the potential of the silver-silver chloride electrode depends on the solution activity of the chloride anion, and this is controlled by the addition of an easily soluble salt of the same anion to the electrode solution. The most commonly used salt is KCl. If for example, a KCl solution of concentration 1.000 mol/L is used, the equilibrium potential of the Ag/AgCl electrode is  $E^{\text{Cl}^-|\text{AgCl}|\text{Ag}} = 236.8$  mV vs SHE at 25 °C [60].

For all experiments in this project, a KCl solution of concentration 3.000 mol/L was used, lending the equilibrium potential a value of 207.0 mV vs SHE at 25 °C according to the electrode manufacturer, Metrohm [81].

### Lithium electrode

The  $\text{Li}/\text{Li}^+$  electrode is a secondary reference electrode of the first kind. Electrodes of the first kind consist of a metal M immersed in a solution containing its own ion  $\text{M}^{z+}$ . The solution is common to that of the measurement cell. In our case the electrolyte solution is non-aqueous (propylene carbonate).

The electrode process is



which has a standard reduction potential of  $-3.045$  V vs SHE [60, page 85].

The equilibrium potential of an electrode of the first kind is a function of the activity of the cation  $\text{M}^{z+}$  in solution, the potential may be expressed using the Nernst equation.

$$E^{\text{Li}^+} = E^{0,\text{Li}^+} + \frac{RT}{F} \ln a_{\text{Li}^+} \quad (2.16)$$

## 2.3 The ozonation process

Ozone is a triatomic homonuclear molecule. Its  $C_{2v}$  symmetry renders it polar, and it is a strong oxidising agent.

Ozone is an allotrope of oxygen, naturally occurring in the ‘‘ozone layer’’ of the Earth’s stratosphere. Ozone is also present at sea-level in low concentrations,

which is usually monitored due to its negative effects on human health. In the Stockholm area the average daily sea-level ozone concentration in June 2009 was  $60 \mu\text{g}/\text{m}^3$ , well below the Swedish recommended limit of  $120 \mu\text{g}/\text{m}^3$  [82]. Sea-level ozone concentration varies with season and depends on wind and temperature conditions.

The first attempt to use ozone as an oxidising agent was done by Besson in 1947 [18]. Today ozonation is a very common method, used mainly to cleanse unwanted compounds by oxidation. Low ozone concentrations (in the industrial meaning) can be produced by UV irradiation of air in a closed space ( $\text{UV}/\text{O}_3$ ); higher ozone concentrations are produced using corona discharge arcs.

Practical electrochromic device operation relies on inserting and extracting a charge density of the order of  $10\text{--}20 \text{ mC}/\text{cm}^2$  between the anodic and cathodic electrochromic films [15]. But during device operation, any amount of charge can *only* be extracted from one film if the other film can accommodate it. Usually, the anodic nickel oxide EC layer, which is in its bleached (i.e., discharged \*) state after sputtering, needs to be activated before operation.

Ozonation presents an alternative method for producing oxidised nickel oxide films. It has been demonstrated that the colouration of the nickel oxide film upon ozonation corresponds to a *well-defined* amount of charge density inserted into the film [13, 15].

On successful precharging of the anodic and cathodic EC layers, an optimally performing device is achieved, i.e., a device operating with its maximum optical modulation range and consuming only a small amount of power.

So far, we have described ozone, the process of ozonation, the necessity of precharging EC layers and why ozonation is a viable route. Now allow me to present some specifics.

The visible effect of ozonation on nickel oxide film is that it becomes coloured, just as it would during a colouration half-cycle in an electrochemical cell. It can thus be inferred that ozonation causes oxidation of  $\text{Ni}^{2+}$  to  $\text{Ni}^{3+}$ . According to Avendaño et al. [9], ozonation also changes the vanadium oxidation state from  $\text{V}^{4+}$  to  $\text{V}^{5+}$  and increases the local distortion around the vanadium ion. This is oddly interesting, since in another paper, Avendaño et al. [11] found that the coloured grain surface layer is void of vanadium ions. Could it be that  $\text{O}_3$  penetrates the nickel oxide grains far enough to react with vanadium? That would imply that the grain surface itself must be very porous.

Bardé et al. [18] observed that during ozonation of  $\beta\text{-Ni}(\text{OH})_2$ , the size and shape of the crystallites was maintained, but their texture became less uniform in appearance. Ozonation is a solid state process [18].

Colouration on ozone exposure may be described by Equations 2.17 and 2.18 [12], wherein bleached  $\beta\text{-Ni}(\text{OH})_2$  and  $\text{NiO}$  forms coloured  $\beta\text{-NiOOH}$  and  $\text{Ni}_2\text{O}_3$  on ozonation. I have written the formulas specifically using  $\beta$  designations, because the work of Bardé et al. [18] showed that the final phase retains the characteristics of the reduced precursor phase on ozonation. Thus  $\alpha\text{-Ni}(\text{OH})_2$  should

---

\*Since different definitions of *charge* and *current* are used in the literature, a clarifying note may be in order. I follow the definition of current as flowing from the positive to the negative terminal of a battery. Since electrons flow in the opposite direction, our electrode is discharged during reduction, and charged during oxidation.

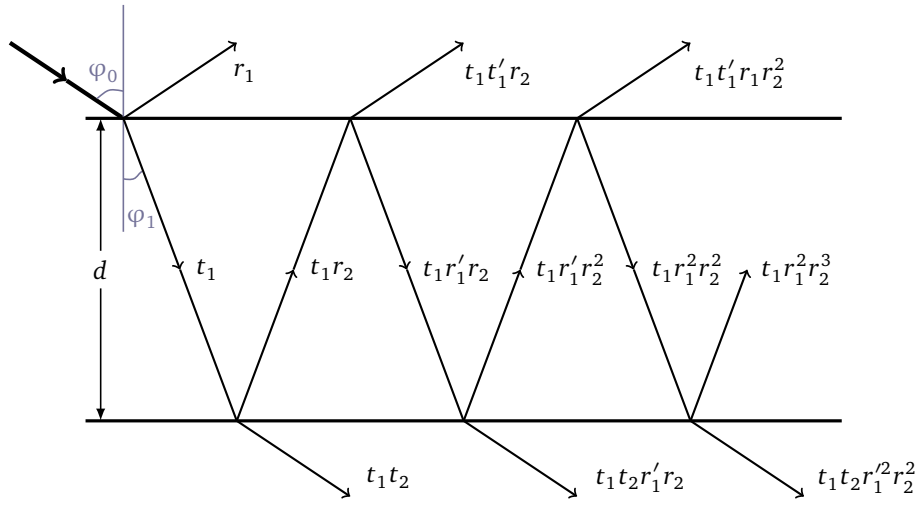

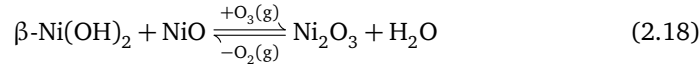
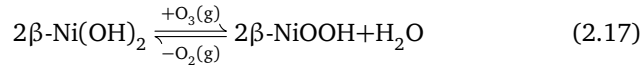


Figure 2.8: Multiple reflections in a thin film layer in air, taking interference effects into account. The angle of incidence is  $\varphi_0$ , the thickness of the layer is  $d$ . All angles are shown greatly exaggerated. 

become  $\gamma$ -NiOOH on ozonation, and  $\beta$ -Ni(OH)<sub>2</sub>  $\rightarrow$   $\beta$ -NiOOH, as written.



Reaction formulas describing the formation of ozone inside the ozonation chamber are presented in [Section 3.2](#).

I have found no sources stating that the UV light has any effect on the nickel oxide film or any of its constituents.

## 2.4 Material optics

### 2.4.1 Optics of a thin film

The absorption in a slab of thickness  $d$  decreases with  $\exp(-\alpha d)$ , where  $\alpha d$  is known as the optical density ( $\alpha$  is the absorption coefficient of the material). A film can be considered thin if  $\alpha d \leq 1$  [73].

Under the Fresnel formalism and by applying Snell's law of refraction at all interfaces of the thin film model, we get the following equations for transmittance and reflectance amplitudes (for the coherent case) [98],

$$t = \frac{t_1 t_2 \exp(-i\delta)}{1 + r_1 r_2 \exp(-2i\delta)} \quad r = \frac{r_1 + r_2 \exp(-2i\delta)}{1 + r_1 r_2 \exp(-2i\delta)}$$

$$\delta = -\frac{2\pi}{\lambda} N d \cos \varphi_1$$

where  $N$  is the refractive index of the thin film. As can be seen the layer thickness  $d$  will affect the phase shift  $\delta$ .  $t$  and  $r$  are amplitude coefficients, and the square of their absolute value will give their measurable quantities, T and R [73].

### 2.4.2 The colouration efficiency

The spectral colouration efficiency (CE) is a measure of how much optical modulation we achieve per charge unit that passes into or out from the electrode. It can basically be expressed as the change in optical density per electrochemical charge density passed.

$$CE = \frac{\Delta(\alpha d)}{Q} \quad (2.19)$$

Since the optical density depends on the wavelength of observation, the colouration efficiency is cited at a wavelength of 550 nm, except for spectral CEs, which present CE across a wavelength range.

CE is defined as positive for cathodic EC materials, and negative for anodic EC materials (in accordance with IUPAC definitions) [84, p. 54ff]. All CEs in this report are thus negative.

Now, Equation 2.19 is not particularly useful for actually calculating the CE. Instead, an expression that states the optical absorbance as a function of experimentally determined transmittance and reflectance values is usually employed.

$$CE(T, R) = \frac{\ln \left( \frac{(1 - R_{\text{colour}})^2 \cdot T_{\text{bleach}}}{(1 - R_{\text{bleach}})^2 \cdot T_{\text{colour}}} \right)}{\Delta Q_{\text{exch charge}}} \quad (2.20)$$

If the changes in the reflectance are small, i.e., if the quota  $\frac{(1 - R_{\text{colour}})^2}{(1 - R_{\text{bleach}})^2}$  is close to unity, it can be neglected altogether and the CE thus calculated as

$$CE(T) = \frac{\ln \left( \frac{T_{\text{bleach}}}{T_{\text{colour}}} \right)}{\Delta Q_{\text{exch charge}}} \quad (2.21)$$

This expression was used to calculate all *in situ* CE values, since *ex situ* reflectance data showed that changes in reflectance were indeed small.

Colouration efficiency is a very useful figure of merit for EC materials [32]. Needless to say, CE should be maximised for most efficient device operation.

## 2.5 Electrochromism

The optical modulation in the nickel oxide film is due to an intervalence charge transfer reaction [54, 99], specifically the transition  $\text{Ni}^{2+} \rightleftharpoons \text{Ni}^{3+} + e^-$  [8, 16]. All electrochromic colouration is fundamentally a consequence of an electron transfer reaction [99], which is not surprising at all since the optical properties of any material is directly connected to its electronic structure.

The colouration efficiency (CE) has empirically been found to correlate well with the crystallinity of the nickel oxide film in the 300–500 nm wavelength range [8, 10]. The CE is also affected by several factors, such as grain size, porosity, and hydrogen and oxygen content of the film [7].

Avendaño et al. [8] relate grain size, oxygen content, colouration efficiency and internal surface area in a neat scheme. The essence of it is: small grains with high oxygen content possess large surface areas and contain large amounts of active material, i.e., oxygen, which ultimately leads to high colouration efficiency.

Several authors, among them [16, 119, 121], assert the importance of the internal surface area to the electrochromic reaction. The oxygen-rich nickel hydroxide and oxyhydroxide phases exist in surface sheaths of the nickel oxide grains. The *external* surface area is just the area of the grain itself, and the *internal* surface area, which I have referred to several times, is the area available to a certain species, such as a proton, in all the cracks, pores, and other regular and irregular cavities on the surface of the grains. The internal surface area is usually orders of magnitude larger than the external surface area, especially for porous materials.

A massive amount of experimental evidence indicates that the electrochromic reaction takes place at the grain boundaries [7, 10, 11, 16, 67, 83].

Upon electrochemical cycling the electrochromic reaction stabilises to reach the steady state. This stabilisation can take several cycles, during which the film structure and composition “sets”, mainly by oxidation of nickel oxide to nickel hydroxide and oxyhydroxide [11]. The activation period is manifested as an either increasing or decreasing charge capacity (depending on electrolyte) that stabilises when steady state conditions are reached [57].

The actual number of cycles required for stabilisation depend on several factors, most importantly film composition and structure and the length and scan rate of the cyclic voltammetry. For example, Niklasson and Granqvist [87] summarised that nickel vanadium oxide films required 10–20 cycles for the charge capacity to stabilise. Green et al. [59], who used cyclic voltammetry parameters identical to mine, performed optical measurements after cycling for about ten cycles. Yu et al. [122] noted very little change in the cyclic voltammetry response after the sixth cycle.





# Experimental method

This chapter presents the employed experimental methods. Additional details are also presented in [Supplement A](#).

We start by describing the properties of the investigated material, the sputtered nickel vanadium oxide sheet. Second the process of ozonation is detailed. Then the *in situ* spectroscopic cyclic voltammetric technique, which constituted the major part of all work, is presented. Finally the methods for *ex situ* spectroscopic analysis are given.

## 3.1 Materials

All films investigated in this study were produced by dc magnetron sputtering between February and April 2009. The sputter deposition parameters were not part of this project. The thesis by Avendaño Soto [12] includes details on optimising dc magnetron sputter deposition parameters for nickel oxide-based sheets. The production number for each sheet that was part of this project is reported in [Table 3.1](#).

### 3.1.1 Some specifics on the sputtered product

The product supplied for this study were  $33 \times 33 \text{ cm}^2$  triple-layer sheets, consisting of  $\text{Ni}_{1-x}\text{V}_x\text{O}_y\text{H}_z$  coated on ITO coated on PET. The top layer (NiO) was sensitive to scraping and abrasion, so all sheets were handled with care and kept between plastic sheets during preparation.

The substrate layer was made of biaxially oriented semicrystalline PET (polyethylene terephthalate) resin, approximately  $175 \text{ }\mu\text{m}$  thick. PET films generally possess good dimensional stability and good optical transparency [97].

The electrically conducting layer ( $\text{Sn}:\text{In}_2\text{O}_3$ , ITO) was approximately  $150 \text{ nm}$  thick. It is known that its deposition method influences the electrochemical behaviour of the nickel oxide film [79], just as any substrate affects what is coated onto it.

The nickel vanadium oxide layer is approximately  $200 \text{ nm}$  thick, and hydrated in its as-deposited condition. Nickel oxide-based films with similar properties have

Table 3.1: A total of five sheets was used during this project. Some sheets were used to produce samples of just one size, others were cut into samples for both optical and electrochemical cycling. All samples (films) of a specific type from one sheet formed a *series*. Series were denoted with a running letter, starting from Z for electrofitted films, and starting from B for films without any electrical contacts. The reported as-deposited transmittance was measured over more than 10 different samples from each series. The resistance values were measured with a regular two-probe ohmmeter and so are not very reliable.

Sheet	Batch	Film dimension	$T_{\text{asd}}$ (550 nm), %	$\bar{\Omega}$ , $\Omega$
N987	Z-series*	70 × 20 mm	— <sup>‡</sup>	—
N987	B-series	40 × 30 mm	61.4 ± 1.64	—
N1041	Y-series*	65 × 15 mm	71.0 ± 1.52	361 ± 57
N1041	C-series	40 × 30 mm	69.5	—
N1067	X-series*	65 × 15 mm	68.9 ± 1.09	455 ± 60
N1099	W-series*	65 × 15 mm	69.8 ± 1.54	342 ± 51
N1167	V-series*	65 × 15 mm	68.1 ± 1.67	545 ± 80

<sup>‡</sup> No *in situ* optical experiments for Z-series films.

\* Samples fitted with electrical contact.

been studied earlier by [6, 7, 10, 14, 15]. The actual transmittance of the film as deposited depends on the precise deposition conditions. Common for all sputtered nickel oxide films is that they are hydrated in the as-deposited state [5, 6].

### 3.1.2 Sample preparation

Every produced sheet was given a production number N#### (see Table 3.1). To perform electrochemical cycling experiments, a small piece of the sheet was cut out and fitted with an electrical contact. To perform experiments *ex situ*, no electrical contact was required, although it caused no problem if such a contact was present. So, early on during the project (after the first sheet was produced) I started cutting every new sheet into smaller pieces directly after production. This preparatory step was performed in a clean-room.

Figure 3.1 shows some photographs from the film electrode cutting process. An ideal “cutting” blueprint is drawn in Figure 3.2, which also shows the dimensions of a finished film electrode.

During sample preparation precautions were taken against damaging the films in any way (see Supplement A.1 for more details).

## 3.2 Ozonation

Ozonations were performed by UV irradiating the nickel vanadium oxide film in an ozone photoreactor (model PR-100 of UVP Inc., Upland, USA) operated in air. Hg lamps provided a nominal irradiation intensity of  $I = 15 \text{ mW/cm}^2$  at  $\lambda = 245 \text{ nm}$  and  $I = 1.5 \text{ mW/cm}^2$  at  $\lambda = 185 \text{ nm}$ . Operation yielded a steady-state ozone concentration of 50 ppm with air in the photoreactor according to the manufacturer’s data sheet. That corresponds to  $\sim 100 \text{ mg O}_3/\text{m}^3$  (using conversion factor  $1 \text{ ppm} = 2.0 \text{ mg/m}^3$ , [40]).

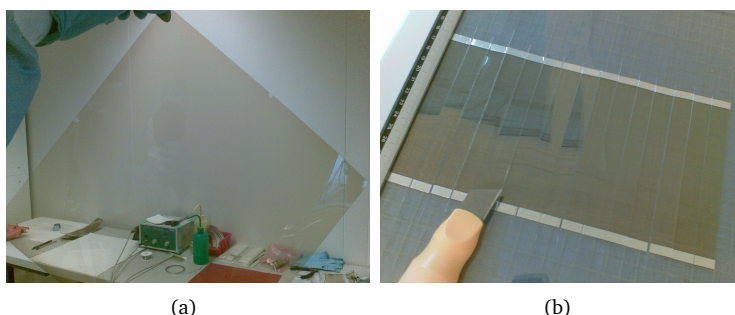
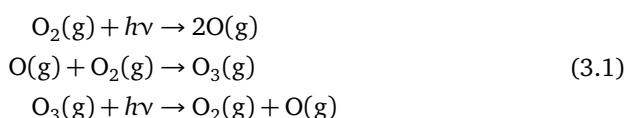


Figure 3.1: (a) A freshly sputtered sheet held up to the light. A brownish tint, caused by absorption in the violet band of the visible spectrum, is visible, as well as a weak reflection of the photographer. (b) Shows part of the same sheet, fitted with electrical contacts and cut into so-called “strips”, which makes two film electrodes by cutting down their middle.

The formation and degradation of  $O_3(g)$  inside the photoreactor can be described by the reactions of Equation 3.1,



where  $h\nu$  is a photon of suitable energy. The first reaction is the rate-limiting step.

Since the ozone concentration inside the photoreactor is high enough to be harmful, the whole ozonation chamber was placed inside a ventilation hood. On ozonation completion, any residual ozone inside the chamber was quickly sucked into the ventilation hood.

Inside the photoreactor six small fans (Panaflo DC brushless, by Matsushita Electric Japan) were placed along the chamber walls facing each other and the film. They were controlled from a separate unit, and always operated at 12 V and 0.1 A each, which gave a suitable fan speed.

The distance between the film in its glass tray and the quartz lamp in the ceiling of the photoreactor was approximately 7 cm.

Films were subjected to ozonation for a time of 20, 40, 60, 90, 120, 180, and 240 seconds and followed by spectral characterisation. One unique film was never subjected to more than one ozonation.

For electrochemical cycling experiments films were subjected to either intermediate ozonation of 40 seconds or long ozonation for 120 seconds, denoted OZ040 and OZ120, respectively. Non-ozonated films were denoted NONOZ or just NOZ.

### 3.3 Cyclic voltammetry with *in situ* spectroscopy

All electrochemical measurements were performed on a ECO Chemie Autolab PGSTAT 10 with a GPES interface, and all cyclic voltammetry experiments used the scan rate  $\nu = 10$  mV/s.

*In situ* spectroscopy was carried out using an OceanOptics S2000 spectrometer. The light beam, supplied by a LS-1 tungsten halogen light source [89], was

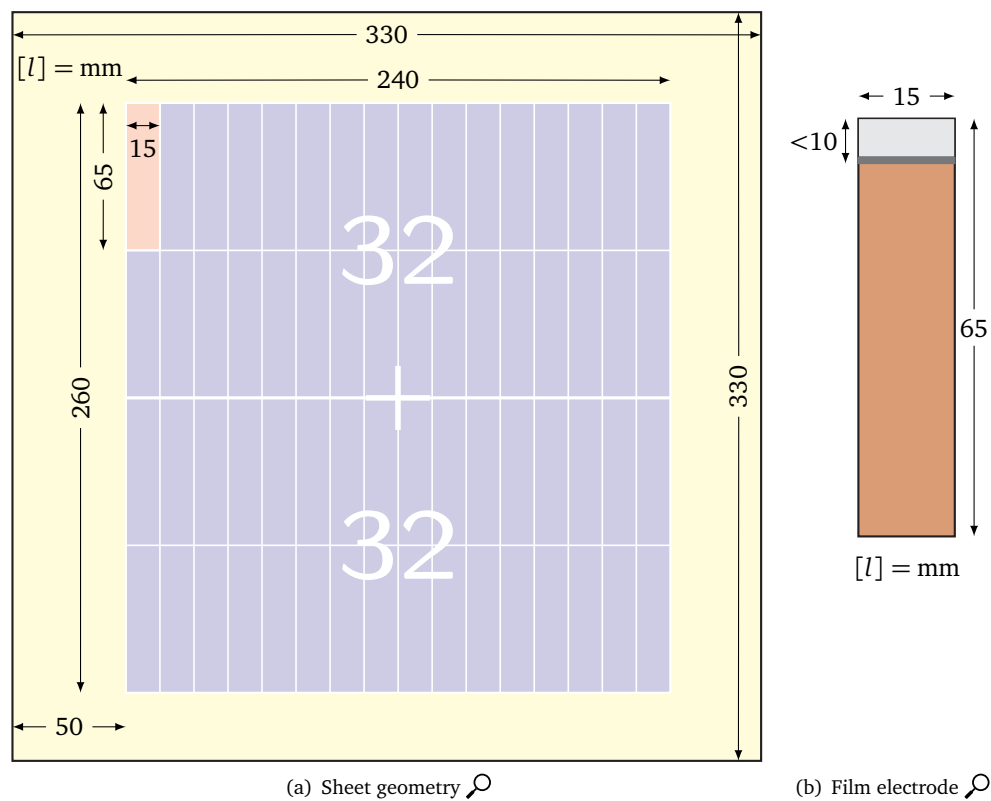


Figure 3.2: (a) Geometry of a sheet, with cutting-scheme for producing two areas of 16 strips each, where each strip consists of two films joined at the bottom, making a total of 64 film electrodes from one  $33 \times 33$  cm sputtered sheet. The margins of the sheet are not used in avoidance of eventual sputtering inhomogeneities towards the sheet edges. (b) Dimensions of a prepared  $\text{Ni}_{1-x}\text{V}_x\text{O}_y\text{H}_z$  film electrode. Shows the electrical tape (light gray) and soldering (dark gray) with typical dimensions.

both conducted to and collected from the spectroelectrochemical cell by 200  $\mu\text{m}$  diameter UV/Vis (200–800 nm) optical fibres (Avantes). The S2000 spectrometer featured an asymmetric crossed beam Czerny-Turner monochromator and a Sony ILX511 small-well CCD detector [90].

The spectrometer was set to an integration (exposure) time of 100 ms, followed by mathematical signal averaging 15 times to increase the signal-to-noise ratio. That way good S/N can be achieved despite the higher photon noise of a small-well CCD compared to a more power-consuming large-well CCD. Flash delay was set to 50 ms.

The spectral profile transmitted through my lab-bench optical system, generated by the LS-1 tungsten lamp, transmitted through a fibre optic cable ( $\sim 1$  m), air, and through another fibre optic cable to the detector, is shown in Figure 3.4 (in the page margin). Total intensity depended mainly on the proper alignment of the two focussing lenses at the air/fibre optic interface. At its peak the intensity reached  $\sim 1800$  counts. During inert atmosphere *in situ* experiments the peak

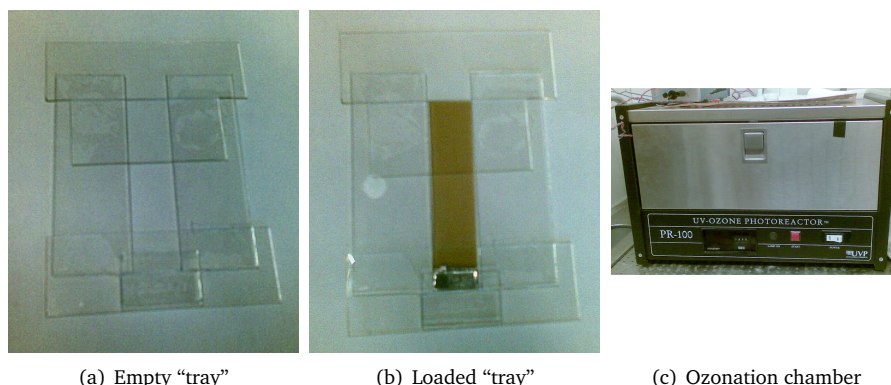


Figure 3.3: This glass support (a), called the “tray”, was used to hold films in place during ozonation and to keep the films in position during optical measurements using the OceanOptics S2000 spectrometer. This was necessary, since the convection inside the ozonation chamber would otherwise have sent the films flying, and the optical measurements benefited since the plastic substrate otherwise tended to bend and curve which reduced transmitted intensity. The “tray” was constructed using glass microscope slides (Thermo Scientific,  $75 \times 25$  mm) and regular superglue. This construction was used for all ozonations. (c) shows the ozonation chamber. Ozonation time was set with an integrated digital timer.

intensity dropped to  $\sim 200$  counts, due to large transmission losses through the glove box fibre optic connectors (inevitable losses, unfortunately).

During an *in situ* experiment spectral intensity values were recorded simultaneously at six wavelengths within the visible range, namely 400 nm, 475 nm, 550 nm, 625 nm, 700 nm, and 775 nm. Measurements were taken at five second intervals (for most experiments, some featured 1-second intervals) and recorded on a PC.

Every spectral capture was preceded by a light/dark calibration of the S2000 spectrometer. For electrochemical *in situ* experiments, the 100% level was taken as the transmittance of the cell containing the electrolyte solution, and for purely optical characterisation of films the 100% level was taken as the transmittance of the air. In all cases the dark level was measured with the detector lens covered with a tight-fitting rubber cap.

Cyclic voltammetry was done in quiet solution (without stirring). Most CV experiments were run for 11 cycles, several were run a larger number of cycles and none less than said number. Precedence has been set by Avendaño et al. [7], who cycled 10 times before optical measurements using the very same setup but a slightly wider potential window and by Green et al. [59] who cycled 10 times before optical measurements. Additional support is provided by Avendaño et al. [11] who stated “excellent electrochromism even from the first voltammetric cycles.”

An added feature of my experiments is that *in situ* optical transmittance was recorded from the start of the first cycle and *continuously* at six wavelengths simultaneously until the end of the experiment.

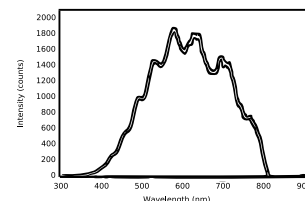


Figure 3.4: Spectral profile of the OceanOptics fibre optic system.

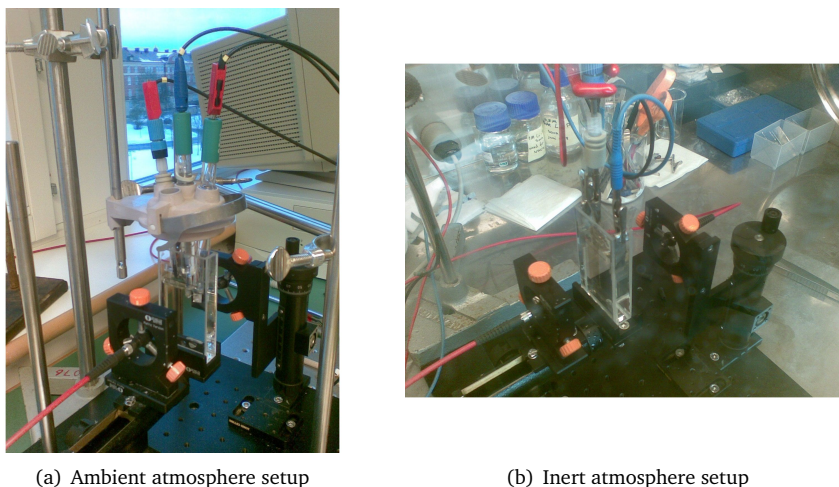
Table 3.2: Summary of all electrochemical cycling experiments. The first letter of the sample designation denotes the series it belongs to, the other two characters are a running index.  $T_i$  is the transmittance at 550 nm, measured *in situ* at the start of the first cyclic voltammogram. Open circuit potential (OCP) is reported vs Ag/AgCl. OCPs are also presented graphically in [Figure 4.10](#). The last column presents the actual area of the nickel film electrode that was immersed into the solution. That area was measured after each experiment with millimeter paper. Experimental *in situ* spectroscopy data for each experiment is presented in [Supplement C](#).

Sample	Electrolyte	State	$T_i/\%$	OCP, V	Area/cm <sup>2</sup>
YO1	KOH-14	NONOZ	75.6	-0.138	6.89
YQ1	KOH-14	NONOZ	78.4	-0.037	6.00
YU2	KOH-14	NONOZ	78.0	-0.155	6.75
YV1	KOH-14	NONOZ	77.3	-0.132	6.90
YW2	KOH-14	NONOZ	76.2	-0.141	6.45
YW1	KOH-14	OZ040	38.1	0.391	6.90
YV2	KOH-14	OZ040	32.9	0.410	6.75
YP1	KOH-14	OZ120	15.3	0.433	5.88
YX1	KOH-14	OZ120	20.7	0.416	6.30
YX2	KOH-14	OZ120	17.3	0.427	6.38
WK1	KOH-12	NONOZ	73.9	-0.038	7.76
WL2	KOH-12	NONOZ	70.3	-0.155	7.68
VG1	KOH-12	OZ040	37.4	0.553	7.50
VG2	KOH-12	OZ040	44.4	0.554	6.95
WJ1	KOH-12	OZ120	8.79	> 0.60	7.76
WK2	KOH-12	OZ120	17.9	0.599	7.69
WM1	LiPC	NONOZ	81.7	-0.487	9.09
WM2	LiPC	NONOZ	75.9	-0.070	8.37
WN1	LiPC	NONOZ	72.4	-0.072	7.50
VD1	LiPC	OZ040	48.3	0.537	6.50
VD2	LiPC	OZ040	50.8	0.540	7.50
WE2	LiPC	OZ120	15.6	0.601	7.14
VY1	LiPC	OZ120	44.3	0.568	8.26
VY2	LiPC	OZ120	40.1	0.567	7.93
VR2	LiPC	OZ120	32.0	0.574	7.05

### 3.3.1 Ambient atmosphere experimental considerations

Electrochemical measurements were carried out in a three-electrode cell (glass cuvette) filled with aqueous potassium hydroxide ( $V \approx 50$  mL) at either pH 14 or pH 12 (strongly alkaline). A platinum foil ( $\sim 1.5$  cm<sup>2</sup>) served as the counter electrode, and a Ag/AgCl electrode as reference (filling solution  $c(\text{KCl})=3$  mol/L). The  $\text{Ni}_{1-x}\text{V}_x\text{O}_y\text{H}_z/\text{ITO}/\text{PET}$  film was placed as working electrode. The typical cell configuration is shown in [Figure 3.6](#).

The potential sweep limits used were  $E_t^c = -0.5$  V vs Ag/AgCl and  $E_t^a = 0.6$  V vs Ag/AgCl, and the sweeps were started at the open circuit potential of the cell. Scan rate was  $\nu = 10$  mV/s.



(a) Ambient atmosphere setup

(b) Inert atmosphere setup

Figure 3.5: The electrochemical *in situ* cell, (a) under ambient atmosphere, and (b) under inert atmosphere inside an argon-filled over-pressurised glove box.

Table 3.3: Conversion between standard electrode potentials at 25 °C. Values for the Ag/AgCl (3 mol/L KCl) electrode vs SHE by Metrohm [81] product sheets. Values for Li/Li<sup>+</sup> electrode vs SHE by Hamann et al. [60, page 85].

SHE	Ag/AgCl	Li/Li <sup>+</sup>
0 V	-0.2070 V	3.045 V
0.2070 V	0 V	3.252 V
-3.045 V	-3.252 V	0 V

### 3.3.2 Inert atmosphere experimental considerations

Electrochemical measurements were carried out in a three-electrode cell glass cuvette filled with 1.0 mol/L LiClO<sub>4</sub>(PC) ( $V \approx 50$  mL). Two pure lithium (99.9%) foils served as counter and reference electrodes. The typical cell configuration is shown in Figure 3.7.

The potential sweep limits used were  $E_t^c = 2.5$  V vs Li/Li<sup>+</sup> and  $E_t^a = 4.0$  V vs Li/Li<sup>+</sup>, and the sweeps were started at the open circuit potential of the cell. Scan rate was  $\nu = 10$  mV/s.

The cells were assembled and maintained in an inert atmosphere glove box with a water content less than 10 ppm. Work under inert atmosphere was necessary since lithium metal is reactive towards air and humidity [59], and propylene carbonate (the solvent) is reactive towards water.

### 3.3.3 Calculated voltage drops

Due to the finite conductivity of any real electrolyte solution, passage of current is accompanied with a voltage drop arising from Ohm's law (Equation 2.4). The voltage drop is proportional to the current and distance through the electrolyte.

Due to space limitations inside the glass cuvette, this aspect had to be sacri-



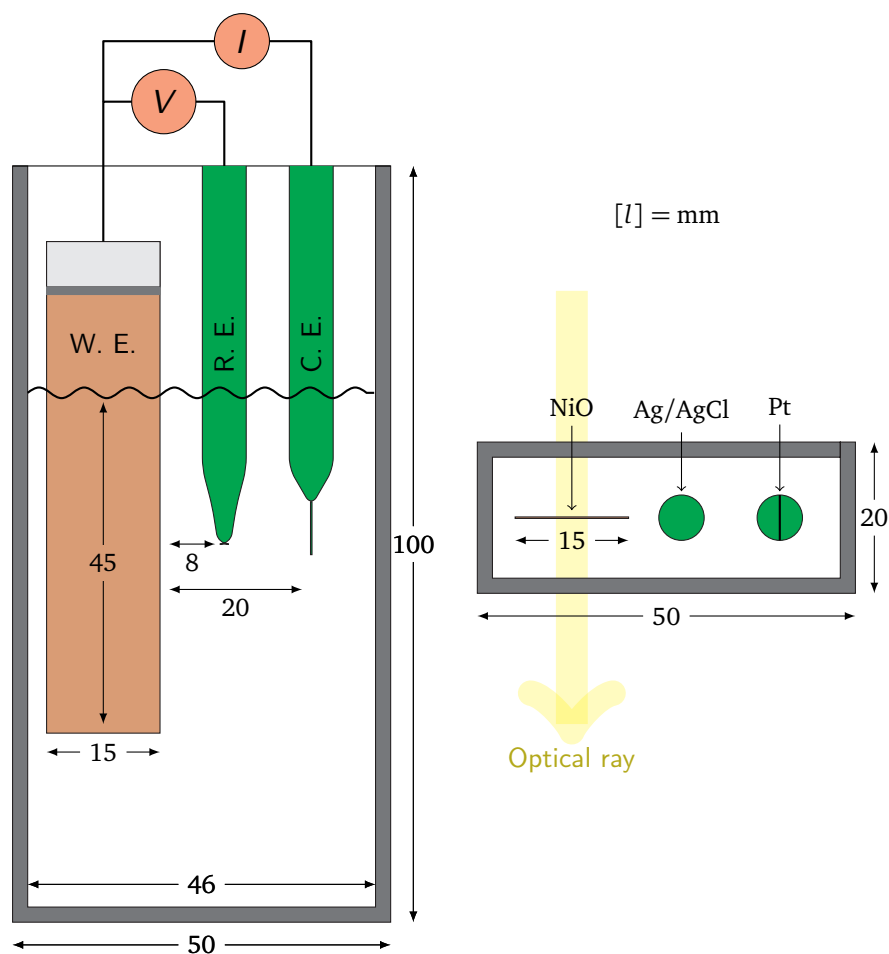


Figure 3.6: The *in situ* electrochemical cell used for aqueous electrolytes, drawn according to scale. Seen along the optical path (at the left) and from above (at the right). Current and voltage are denoted  $I$  and  $V$  respectively. 🔍

ficed to achieve good *in situ* spectroscopy conditions.

Nonetheless, the voltage drop was calculated for every electrolyte and electrode configuration used (for electrode configurations, see Figure 3.6 and Figure 3.7).

Equation 2.9 was used to calculate the voltage drop. The width of the cuvette (50 mm) was used as the distance  $l$ , and the highest recorded current density was inserted as  $j$ . The straight-forward calculation gave that voltage drop (across the width of the cell) was  $\sim 10$  mV for KOH-14,  $\approx 0.1$  V for KOH-12, and  $< 0.1$  V for LiPC.

No corrections have been applied to the reported cyclic voltammograms.



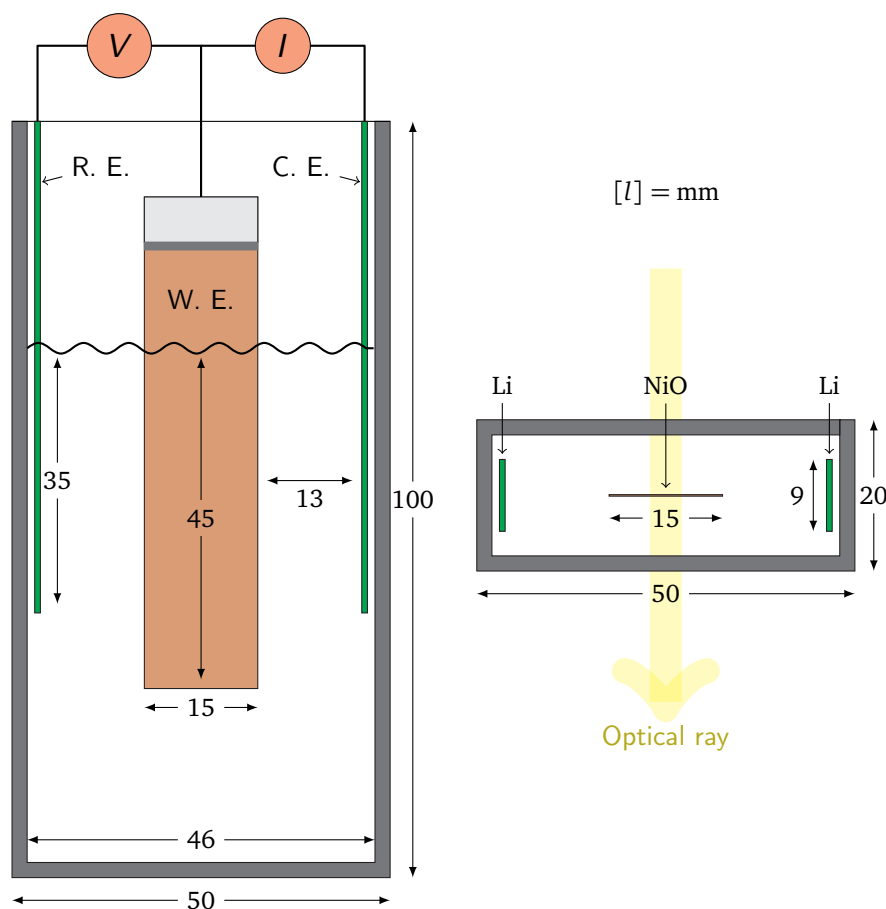


Figure 3.7: The *in situ* electrochemical cell used for  $\text{LiClO}_4/\text{PC}$  electrolyte, drawn according to scale. Seen along the optical path (at the left) and from above (at the right). Current and voltage are denoted  $I$  and  $V$  respectively. The shown electrolyte level (wavy horizontal line) corresponds to approximately 50 mL, which was the volume used in all experiments. 🔍

### 3.4 Optical characterisation in the solar wavelength range

*Ex situ* transmittance and reflectance spectra were collected with a UV-Vis-NIR Perkin Elmer  $\lambda 9$  spectrophotometer.

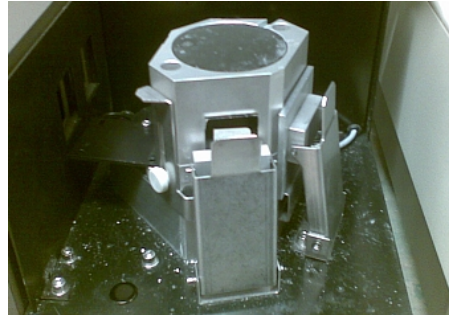
The  $\lambda 9$  is a 1980's era state-of-the-art spectrophotometer, with a rotating-mirror beam splitter, and a  $\text{BaSO}_4$  coated integrating sphere. The instrument employs a deuterium lamp in the 200–320 nm range, and a tungsten lamp up to 2500 nm. Two detectors are also employed; a photo-multiplier tube between 200–860.8 nm, and a lead sulfide detector between 860.8–2500 nm. The detectors are located inside the integrating sphere [64].

The discontinuities at 319.2 nm and 860.8 nm, which are visible in several spectra, are thus artifacts due to the change of lamp and detector in the spectrophotometer [64].

Electrochemically cycled films were withdrawn from the electrolyte, rinsed

(a) Perkin Elmer  $\lambda 9$ 

(b) Reflection mode



(c) Transmission mode

Figure 3.8: (a) Perkin Elmer  $\lambda 9$  spectrophotometer, with the integrating sphere setup for ?? reflectance measurement and for ?? transmittance measurement.

with deionised water, blown dry with with nitrogen air and thus placed in the sample compartment of the spectrophotometer. Transmittance was measured at normal incidence, and reflectance was measured at near-normal incidence, between 300–2500 nm. The lower limit was set to 300 nm since nickel oxide is known to absorb strongly below 350 nm, due to its semiconductor band gap [7].

Although the bulk of all optical characterisations were performed on the  $\lambda 9$ , some were performed with a Perkin Elmer  $\lambda 900$ . The main difference towards the  $\lambda 9$  was its faster spectra collection time, on top of a host of other improvements, I suppose.

## Results and discussion

In this chapter the results are divided into two major sections. Ozonated (and non-ozonated) films who were not subjected to electrochemical cycling form one logical section, and are presented first since they form the baseline behaviour against which the films' behaviour after electrochemical cycling is compared. The second section, which is the largest, is subdivided into four main parts. First, colouration efficiencies and charge capacities are presented, followed by recorded open circuit potentials and aggregated *in situ* spectroscopy data. Section 4.2.1 shows how the bleached and coloured state *in situ* transmittance ( $T_b$  and  $T_c$ ) behaved in the studied electrolytes and under different ozonation states. Section 4.2.2 presents the results of a long-time (over 700 cycles) experiment in LiPC of an ozonated film. Finally, in Section 4.2.3 some remarks are made on the films tendency to break upon cycling in KOH-14.

### 4.1 Ozonated films characterised optically

Before cycling ozonated NiO-films, the optical response after ozonation needed to be determined. From previously published results [15] it was clear that nickel oxide films respond to ozonation by *colouring*, and that the colouring was not physically different from that achieved by electrochemical cycling.

Figure 4.1 shows ozonation curves in the visible spectral region for Y-series, V-series, B-series, and W-series films. Although some differences can be observed between the series, especially for intermediate ozonation times, the overall reproducibility is good.

When the optical transmittance at 550 nm is extracted from the ozonation curves, and plotted against ozonation time, we get a nice set of “standard ozonation curves” (Figure 4.2), that show how the transmittance decreases with increasing ozonation time. For large-area nickel oxide films I expect the overall shape of the curve to be preserved, but unless a higher ozone concentration is employed, longer ozonation times should be expected.

Table 4.1: Optical transmittance at 550 nm for ozonated films at ozonation times of 0, 20, 40, 60, 90, 120, 180, and 240 seconds. The presented error values are calculated standard deviations, based on measurements of  $n$  number *different* films. Transmittance was measured with the OceanOptics S2000 spectrometer, except for W-series and X-series, which were measured on the Perkin Elmer  $\lambda$ 900 spectrophotometer. All reported values pertain to films ozonated in fresh condition (within at most three days since sputter deposition), except X-series which was ozonated 39 days after deposition, as a test. For comparison,  $T_{550}$  for as-deposited X-series was  $68.9 \pm 1.1$  % ( $n = 12$ ).

	Y-series		V-series		B-series		W-series		X-series	
	$T_{550}/\%$	$n$	$T_{550}/\%$	$n$	$T_{550}/\%$	$n$	$T_{550}/\%$	$n$	$T_{550}/\%$	$n$
NONOZ	$71 \pm 1.7$	2	$68.1 \pm 1.7$	12	$61.5 \pm 1.7$	5	$69.6 \pm 2.1$	8	$67.8 \pm 1.0$	8
OZ020	$58.0 \pm 0.3$	2	$54.1 \pm 0.8$	3	$46.1 \pm 0.2$	2	-	-	$65.0 \pm 0.9$	4
OZ040	$32 \pm 3.2$	2	$39.3 \pm 2.0$	3	$37.4 \pm 1.9$	2	$37.4 \pm 6.2$	4	-	-
OZ060	$17.7 \pm 1.1$	2	$37.5 \pm 2.7$	3	$16.3 \pm 1.9$	2	-	-	-	-
OZ090	-	-	$26.5 \pm 2.0$	3	-	-	-	-	-	-
OZ120	$8.2 \pm 0.7$	2	$25.0 \pm 3.2$	3	-	-	$19.4 \pm 2.5$	4	$54.6 \pm 2.9$	4
OZ180	$6.3 \pm 2.0$	2	$10.5 \pm 0.3$	3	$14 \pm 11$	2	-	-	-	-
OZ240	-	-	9.3	1	-	-	-	-	-	-

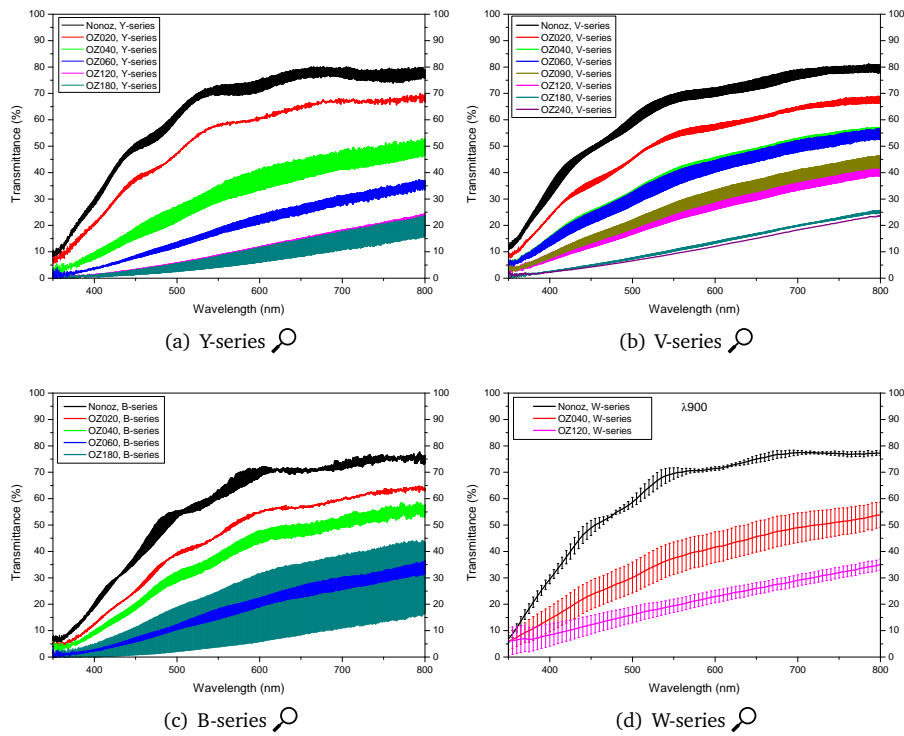


Figure 4.1: Transmittance of films in the visible after ozonation. Each “band” in the plots is based on measurements of at least two films.

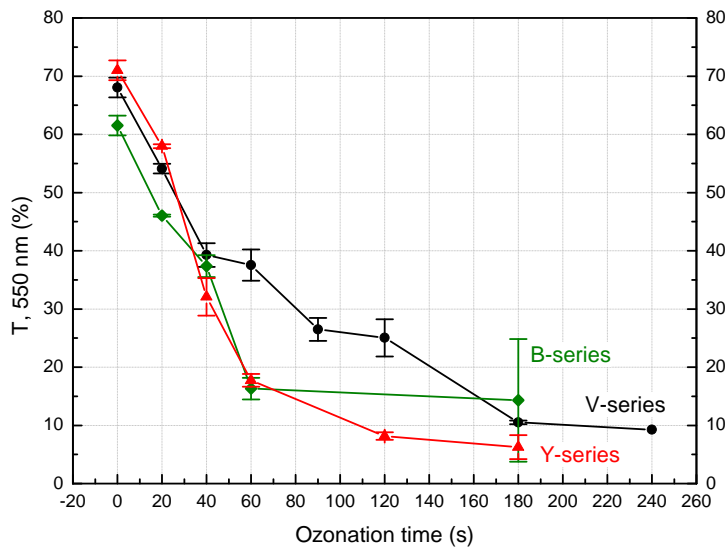


Figure 4.2: Transmittance at 550 nm after ozonation of B-series, Y-series and V-series films. The sputtered nickel oxide films’ response to ozonation shows good reproducibility across separately sputtered sheets (series). Tabulated in Table 4.1.

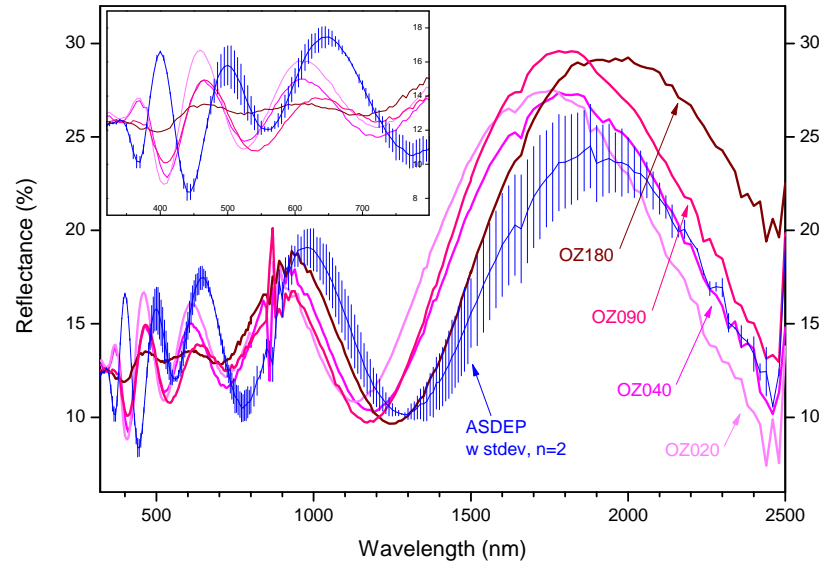


Figure 4.3: Reflectance spectra of as-deposited and ozonated V-series. The inset shows a magnified view of the visible (300–800 nm) region. The reflectance spectra show far less modulation with ozonation state than the transmittance spectra, which shows that  $\text{Ni}_{1-x}\text{V}_x\text{O}_y\text{H}_z$  exhibits transmittance modulation rather than reflectance modulation on colouration [43]. The reflectance spectra also suggest that film reflectance depends on ozonation time in the near-IR region. At these wavelengths, the reflectance of ITO should dominate the spectrum, so it is hard to say if this modulation depends on the nickel oxide layer. 🔍

X-series samples (Table 4.1) were stored for 39 days after sputter deposition, and then the optical transmittance after ozonation was measured. The transmittance values at 550 nm are presented in Table 4.1. Ozonation for 120 s had the same effect as ozonating a fresh sample (characterisation within three days after sputtering) for just 20 seconds. So, clearly something happened in the films during storage that diminished the films' susceptibility to the effect of ozonation.

Figure 4.3 shows a reflectance “ozonation curve”, recorded from just one series, in the solar wavelength range. The inset shows that total reflectance is low (it would be even lower if corrections for integrating sphere effects were applied to the reflectance spectra, but in any case the difference would have been minor and affected all spectra in the same way, so comparisons are still valid) and that no clear effects of ozonation can be discerned in the visible region. This shows that  $\text{Ni}_{1-x}\text{V}_x\text{O}_y\text{H}_z$  films exhibit transmittance modulation rather than reflectance modulation on ozonation.

The reflectance above  $\sim 2000$  nm appears to increase with increasing ozonation time in a quite regular fashion. In this region of the spectrum the reflectance of the ITO layer is known to be substantial, which makes any further derivations from this observation mere speculation at this stage.

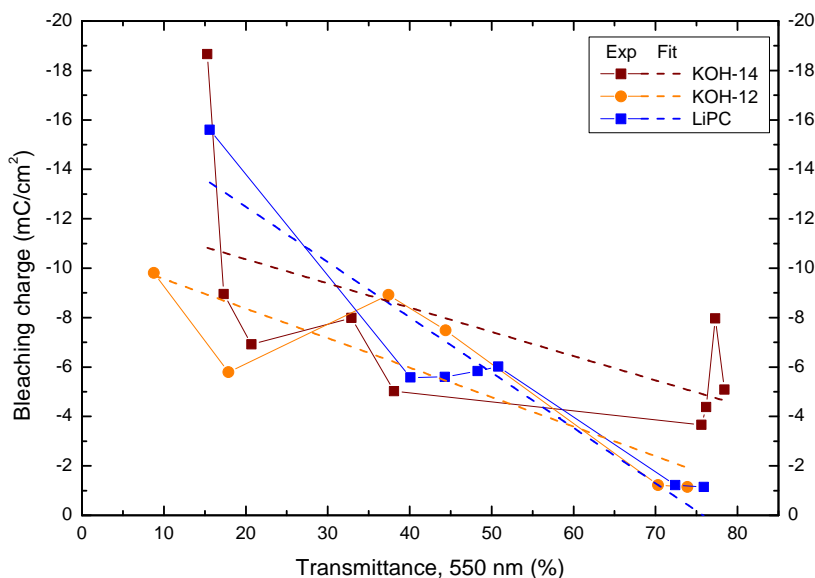


Figure 4.4: Measured transmittance (550 nm) post ozonation versus inserted charge density during the first CV cycle after ozonation. KOH-14 and KOH-12 show roughly the same dependence, with  $|Q_c|$  increasing  $\sim 0.10$  mC/cm<sup>2</sup> for every percent point decrease of transmittance. LiPC shows a more marked increase of  $|Q_c|$  with diminishing transmittance. See Figure C.1 for separate plots of each electrolyte. 🔍

## 4.2 Ozonation followed by electrochemical cycling

Figure 4.4 shows clearly that ozonation corresponds to extracting negative charge from the film. Furthermore, a difference exists between the studied electrolytes. KOH-14 and KOH-12, which differ only by ionic concentration, have the same slope but the higher concentration KOH-14 corresponds to a larger extracted charge, as expected. LiPC shows a different slope, indicating that different electrolytes (with different electroactive species) have different abilities at restituting the charge extracted by ozonation.

The cathodic charge ( $Q_c$ , total charge during the cathodic half-cycle) is used as a good approximation for the total charge consumed from start of the first cycle until complete bleaching. Manual integration of the charge from the potential at the start of the first cycle to the actual bleaching potential was tested, but did not significantly deviate from the cathodic charge as calculated by the instrument. The cathodic charge was thus used as an approximation of the bleaching charge at all times. I believe this approximation was also used by previous workers [15], although it was not explicitly stated.

Figure 4.5 demonstrates a neat feature of uninterrupted *in situ* optical monitoring; the ability to calculate CE for each cycle as the cycling progresses. In KOH-14 and KOH-12, CE decreases markedly after the first cycle for ozonated films, and then levels out. The initial drop is due to the very large optical modulation during the first cycle, which is then never achieved again. Intermediately ozonated samples cycled in KOH-14 decreased initially, but then increased slightly after a

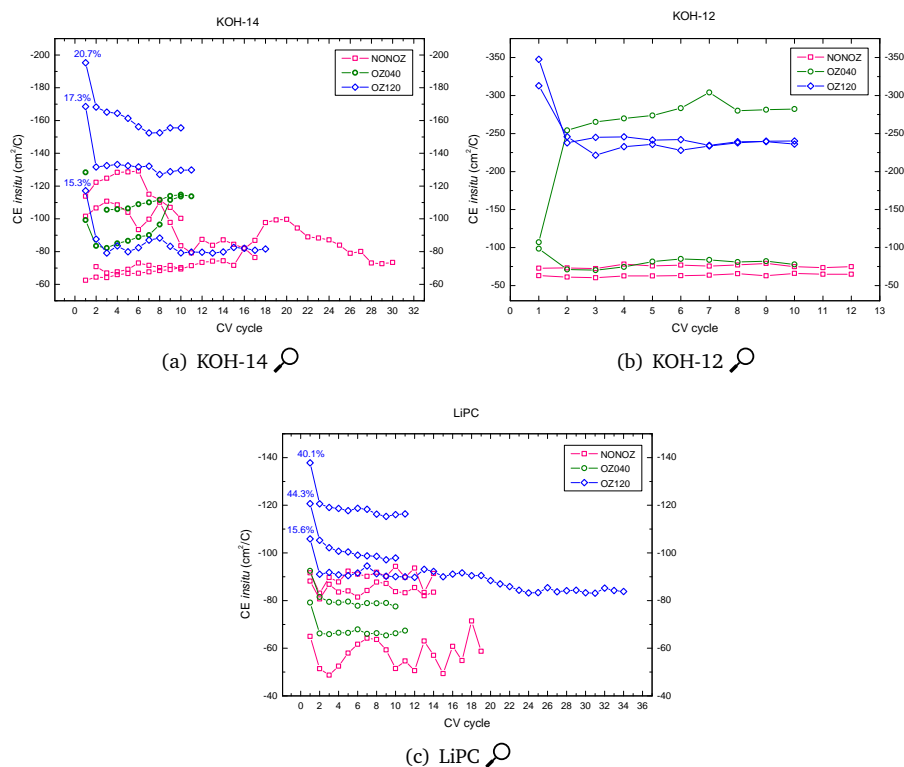


Figure 4.5: Colouration efficiency *in situ* per cycle, for electrochemical cycling in (a) KOH-14, (b) KOH-12, and in (c) LiPC. Each line corresponds to one sample. Experiments at each ozonation state were performed at least in duplicate.

few cycles as the charge capacity stabilised (*cf.* Figure 4.9(a)). Intermediately ozonated films cycled in KOH-12 displayed ambiguous results, while intermediately ozonated films cycled in LiPC decreased on the first cycle and then quickly stabilised. It is interesting to note that ozonated films cycled in LiPC did not show an increase of CE with decreasing transmittance, as would be expected, instead the film with low transmittance (15%) shows a consistently lower CE than the films with  $\sim 40\%$  transmittance. But in general, for all electrolytes, more ozonated films displayed higher colouration efficiencies, neglecting minor deviations.

The colouration efficiency at the tenth CV cycle is plotted in Figure 4.6, and shows that the highest CE across all ozonation states is achieved in KOH-14, while ozonated films show an exceptionally high CE in KOH-12. The CE in LiPC is moderate compared to the other electrolytes, which reflects that the amount of exchanged charge increases with ozonation in LiPC, in contrast to KOH-14 and KOH-12 (see Figure 4.7).

This brings us to the measured charge capacities at stable cycles, shown in Figure 4.7. Films cycled in KOH-14 display an indeterminate trend, with  $\sim 10$   $mC/cm^2$  exchanged for non-ozonated films, and slightly smaller exchanged charge for ozonated states. The standard deviations in KOH-14 are significant, except for OZ040. This could be an effect of experimental inexperience on the author's part,



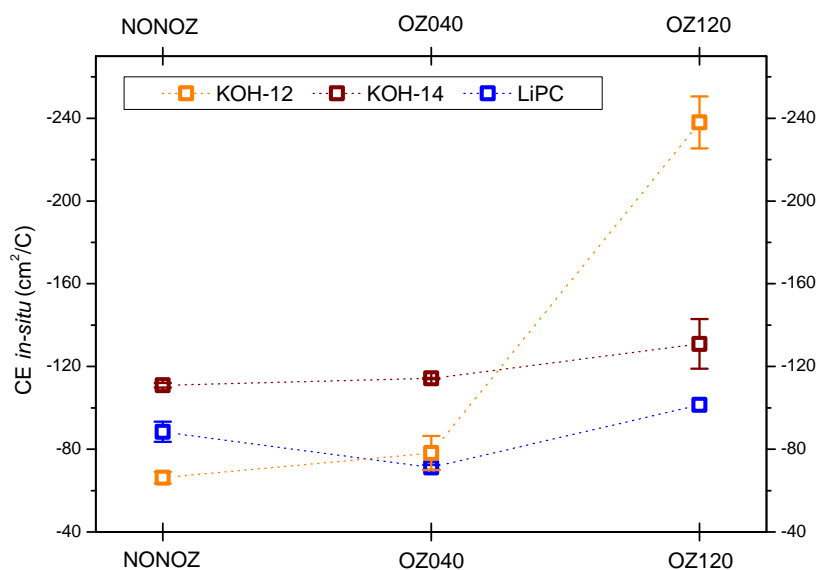


Figure 4.6: CE at CV cycle 10 across ozonation states and electrolytes.

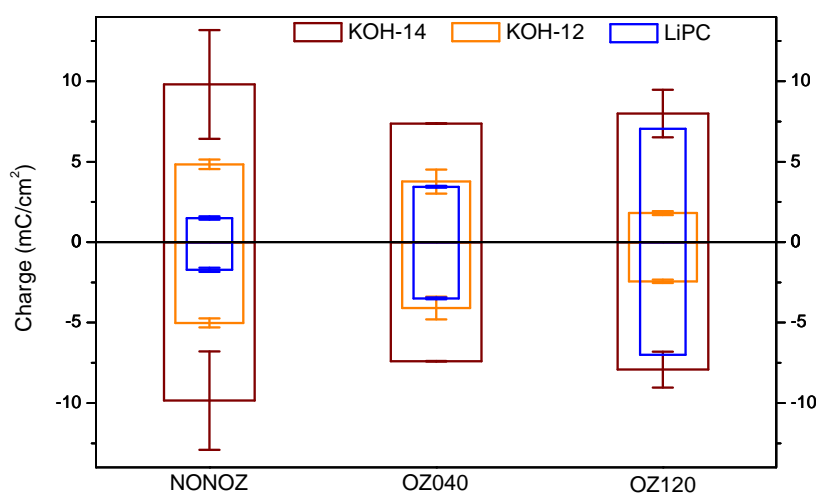


Figure 4.7: Charge capacity at stable CV cycle, with standard deviation, for all electrolytes and ozonation states. Each bar is based on two experiments, except for LiPC OZ120 which is based on one experiment.

since the first experiments to be conducted were those in KOH-14.

The exchanged charge in KOH-12 decreases with increasing ozonation time, with  $4.9 \text{ mC/cm}^2$  for non-ozonated films,  $4.0 \text{ mC/cm}^2$  for intermediately ozonated films and  $2.1 \text{ mC/cm}^2$  for ozonated films. The completely opposite trend is observed in LiPC, with increasing charge capacities as ozonation increases. The small charge capacity ( $1.6 \text{ mC/cm}^2$ ) for non-ozonated films increased to  $7.0 \text{ mC/cm}^2$  for the ozonated film. All exchange charge capacity values are also reported in Figure C.2.

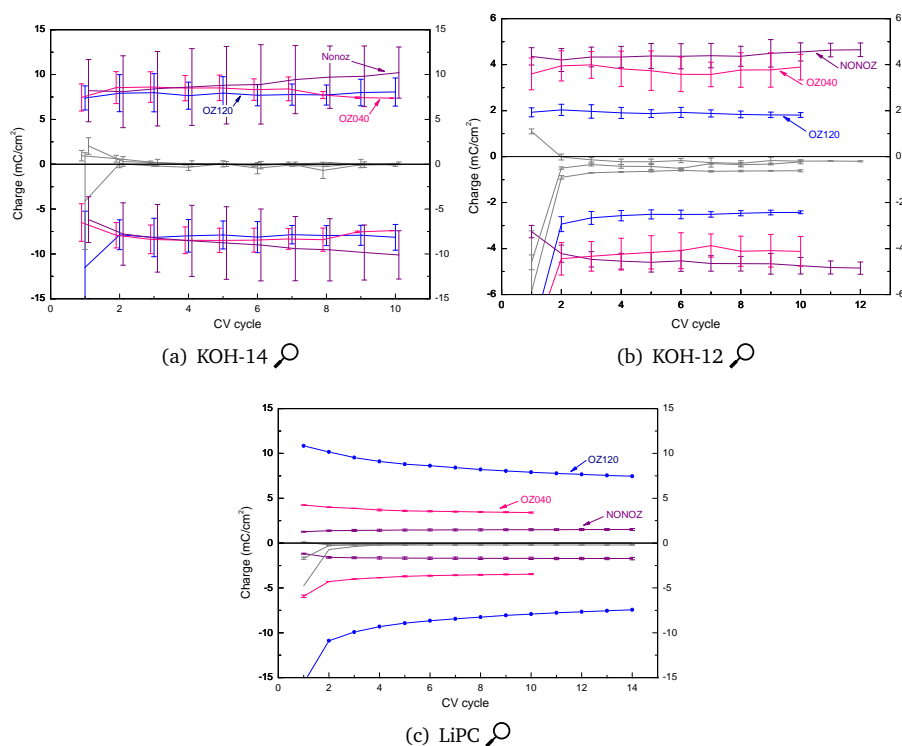


Figure 4.8: Charge capacity per cycle for different states of ozonation. The gray lines, close to  $y = 0$  in the plots, are the difference between the anodic and cathodic charge capacity. If it lies *below* the  $y = 0$  line  $Q_c > Q_a$ , and if it lies *above* the line  $Q_a > Q_c$ .

Figure 4.8 again shows the charge capacity, but for all recorded cycles. We note that the anodic and cathodic charge capacities are of the same magnitude, except in KOH-12, where cathodic charge capacity is slightly larger. In LiPC and KOH-12 the charge capacities of different ozonation states are well separated for all cycles, while we have essentially the same charge capacity for all ozonation states in KOH-14 due to the large experimental error.

In the previously mentioned plot, the actual difference between the anodic and cathodic charge capacities were barely seen due to the scale. Figure 4.9 remedies this, and shows the ratio of anodic charge to cathodic charge for all experiments, except the long-time run in LiPC, which is reported separately.

Figure 4.9 shows that for non-ozonated films in LiPC, the charge capacity never becomes reversible and the difference stays almost constant throughout the cycling experiment at a level of  $-15\%$ , which is quite large. Ozonated films in LiPC show more reversible charge capacities, and on cycling for 33 cycles (OZ120) the anodic charge became larger about halfway through the experiment, indicating that the ratio stabilises above zero for ozonated films in LiPC. Films in KOH-12 and KOH-14 generally show good reversibility, with most films lying within  $\pm 5\%$ .

Regarding Figure 4.10 I would just like to note that the increased OCPs for ozonated states in KOH-12 relative to ozonated states in KOH-14 reflects the fact

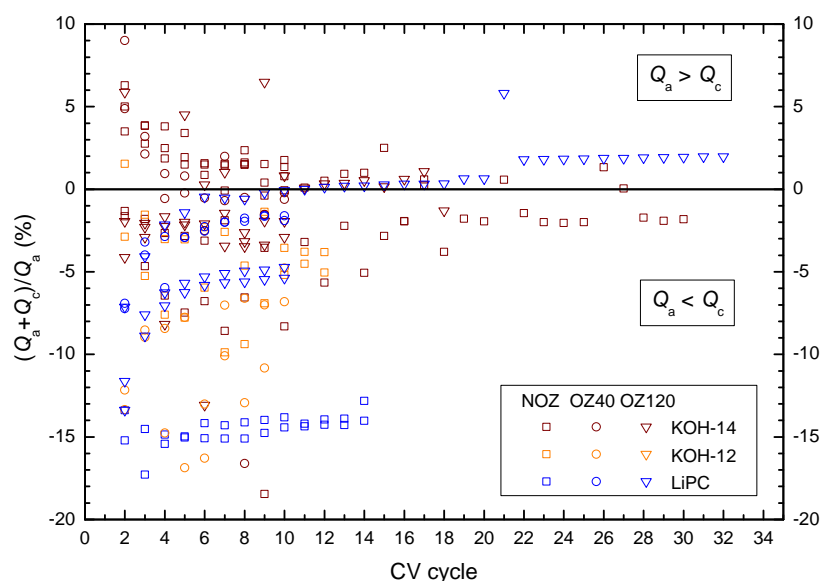


Figure 4.9: Difference between anodic and cathodic charge as percent plotted per CV cycle. 🔍

that the stability window for  $\text{Ni}(\text{OH})_2$  lies within sloping potential boundaries in its Pourbaix diagram (see Figure 2.1). For future experiments, the potential window for lower pH KOH(aq) should be adjusted accordingly. The increased ohmic drop in the electrolytic solution on lower pH should also be taken into account.

Figure 4.11, 4.12, and 4.13 show the actual recorded cyclic voltammogram at stable cycles along with the *in situ* recorded transmittance at 550 nm for the same cycles. The total area covered by each CV cycle corresponds to the total charge capacity (cf. Figure 4.7). The spectra show how the transmittance changes during a cycle, and where the maxima and minima are placed relative to the cyclic voltammogram.

Recorded CVs with overlaid transmittance curves for all experiments are shown in Supplement C, Figure C.13–C.26.

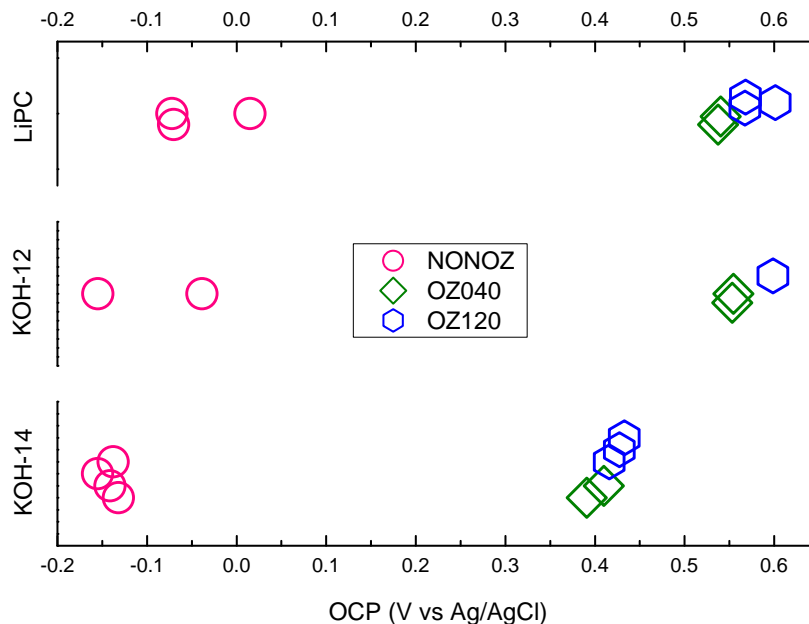


Figure 4.10: Open circuit potentials at start of electrochemical cycling, per electrolyte and for non-ozonated, intermediately ozonated and ozonated films. The basic rule of increasing OCP on oxidation is obeyed, although the difference in OCP between OZ040 and OZ120 is smaller than expected.

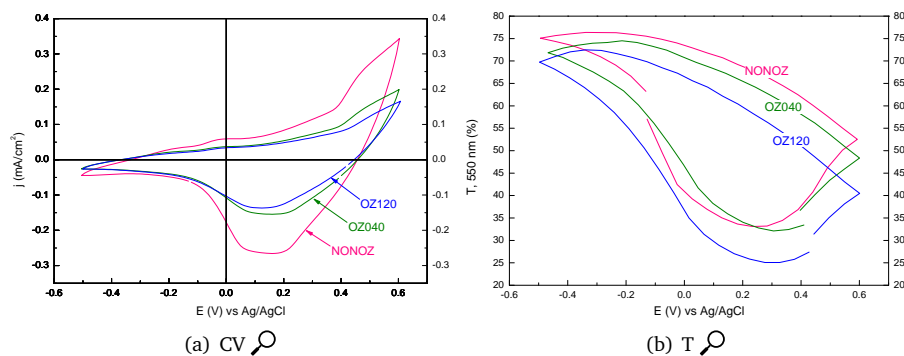


Figure 4.11: KOH-14. CV and T at stable cycles for KOH-14. (a) shows that the charge capacity in KOH-14 decreases on ozonation. The decrease in charge capacity on ozonation is accompanied with a minor shift of the optical modulation band (b). See Figure C.13 for a view split per ozonation state.

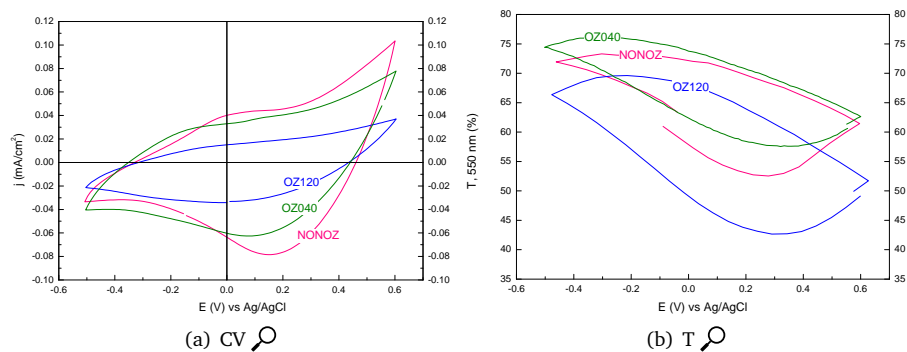


Figure 4.12: KOH-12. CV and T at stable cycles for KOH-12. (a) shows that the charge capacity in KOH-12 decreases on ozonation. The decrease in charge capacity is accompanied with a significant shift downwards of the optical modulation band (b). See Figure C.14 for view per ozonation state.

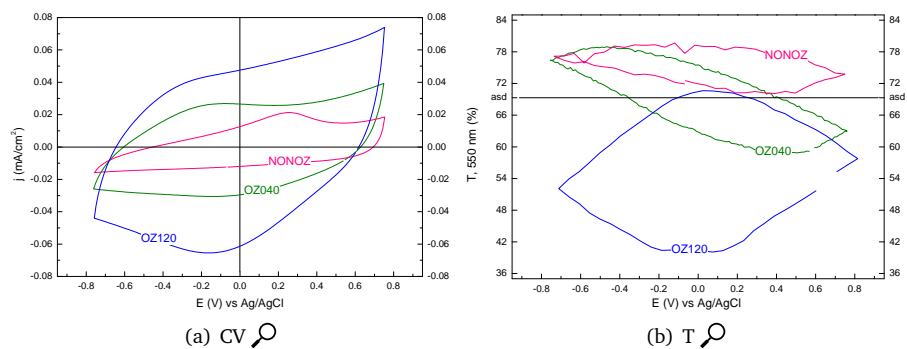


Figure 4.13: LiPC. CV and T at stable cycles for LiPC. (a) shows how the charge capacity increases on ozonation. (b) shows how the optical modulation band switches from only bleaching vs the as-deposited to only colouring vs the as-deposited state as ozonation time is increased. Intermediate ozonation gives the optical modulation an intermediate behaviour. See Figure C.15 for view per ozonation state.

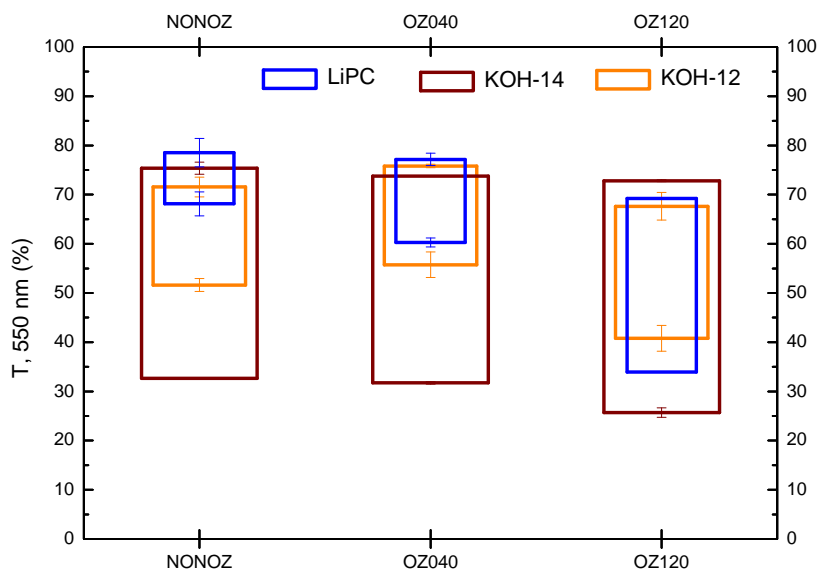


Figure 4.14: Column plot showing the optical modulation band limits in all electrolytes per ozonation state. The top level of a box is the bleached state transmittance ( $T_b$ ) and the bottom is the coloured state transmittance ( $T_c$ ).

#### 4.2.1 Optical characterisation

Let us briefly remind ourselves of our intention. The purpose of a transmittance-modulating electrochromic device (ECD), which is where the nickel oxide film is intended to function as counter electrode, is to *modulate* the optical transmittance within as wide limits as possible while consuming as little charge as possible. The priority is optical modulation (large difference between coloured and bleached state), since charges are still generally small and an acceptable cost to bear.

Figure 4.14 shows the optical modulation band limits at stable CV cycles in all electrolytes and for non-ozonated, intermediately ozonated and ozonated films. This relatively simple barplot diagram essentially contains the essence of this whole project. Namely, that ozonation in KOH-14 and KOH-12 increases the optical modulation only slightly, whereas ozonation and subsequent electrochemical cycling in LiPC turns a rather poor electrolyte (see the small modulation for non-ozonated films in LiPC) into a rather potent electrolyte, almost as good as KOH-14. This is also the major finding of this work. It indicates that the electrochromic performance of nickel oxide-based layers in Li-based electrolytes can be significantly boosted by charge extraction prior to cycling.

If Figure 4.14 was a “snapshot” of the optical modulation limits, Figure 4.15 displays the  $T_b$  and  $T_c$  per CV cycle.

Figure 4.15 showed that the coloured state transmittance changed more than the bleached state transmittance, and that a marked change occurred during the first few cycles. So, Figure 4.16 shows the  $T_c$  for the three first CV cycles grouped per ozonation state.

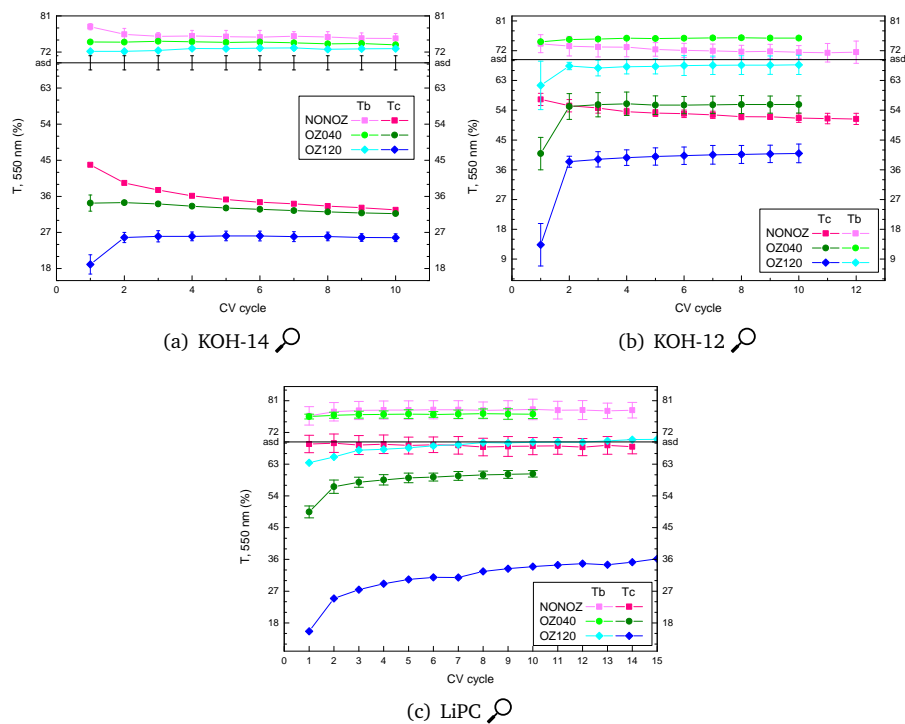


Figure 4.15: Bleached and coloured state transmittance,  $T_b$  and  $T_c$ , versus CV cycle and for each ozonation state. (a) shows the recorded behaviour for KOH-14, (b) shows KOH-12, and (c) shows that for LiPC.

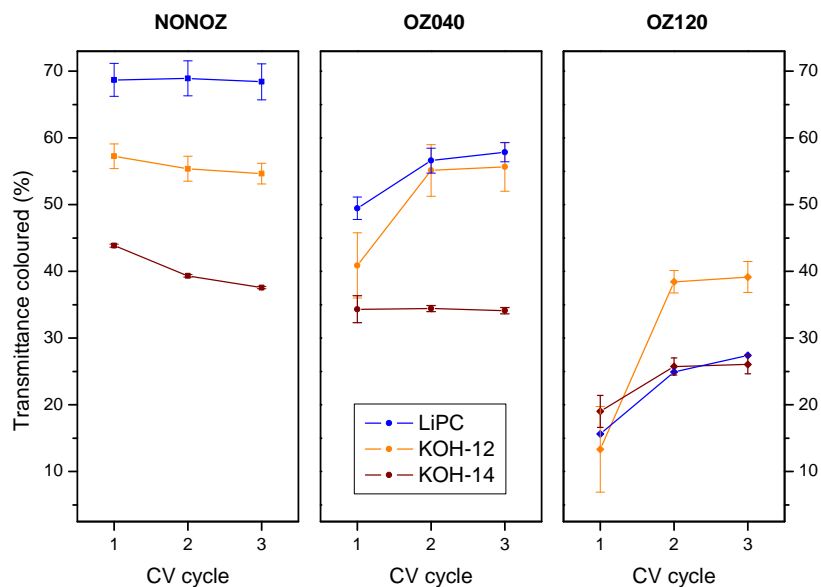


Figure 4.16:  $T_c$  for the first three CV cycles shown for different ozonation states (including non-ozonated).

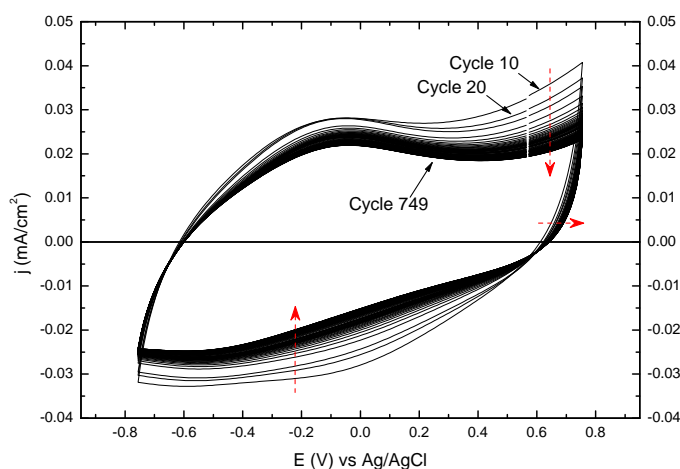


Figure 4.17: Recorded CV of long-time run of ozonated sample in LiPC. 🔍

#### 4.2.2 Long-time experiment in LiPC

It was observed that the coloured transmittance level,  $T_c$ , increased slowly for ozonated films in LiPC (see Figure 4.16(c)). To further investigate this behaviour, an extended cycling experiment in LiPC of an ozonated film was performed. During this experiment, one ozonated film was cycled a total of 749 cycles (Figure 4.17).

Cyclic voltammograms were recorded for every tenth cycle, except during the last 100 cycles, where every cycle was recorded.

During the last 100 cycles of the long-time experiment, the difference between cathodic and anodic charge was  $5.00 \pm 0.01\%$  (anodic charge was consistently five percent larger than the cathodic charge). The exhibited stability over those 100 cycles was exceptional, as evidenced by the low standard deviation.

The observed *in situ* transmittance at 550 nm (Figure 4.18) behaved like other ozonated films in LiPC initially, but changed character slowly. By the 31<sup>st</sup> cycle, the change of  $T_{550}$  with time had become slower, and the  $T_c$  had increased by seven percent units. At the last recorded cycle, the optical behaviour looked just like that of a non-ozonated film. The CV for the last cycle (cycle 749, Figure 4.17) exhibited a charge capacity equivalent to that of a non-ozonated film.

In summary, it was observed that, on continuous cycling in LiPC for over 700 cycles, an ozonated nickel oxide film slowly lost the optical and coulometric behaviour characteristic of an ozonated film, and eventually behaved just like a non-ozonated sample. This could be due to protons being consumed by the Li counter electrode in our setup. Based on that assumption, cycling of an ozonated nickel oxide film in an actual device could render it more stable than observed in this experiment.

#### 4.2.3 Film breakage on cycling in KOH-14

Cycling in KOH-14 caused mechanical failure after cycling for some time, which was curious at first since nickel oxide should be stable in alkaline conditions. Figure 4.19 shows photos of some films where the nickel oxide layer failed. I also



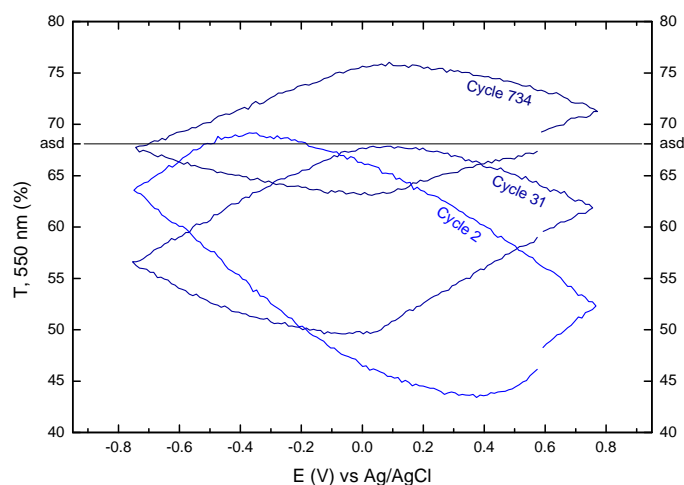


Figure 4.18: Optical *in situ* transmittance at 550 nm of long-time run of ozonated sample in LiPC. 🔍

observed that both the nickel oxide layer and ITO layer were affected, since resistance measurements on the exposed areas showed very high resistance, indicating that the ITO layer came loose together with the NiO layer.

Based on my observations I theorised that the breakage started at the film edges, the only place where the ITO layer should be exposed to the solution. To test this assumption, I sealed the edges of one film (YQ1) with two-component epoxy glue (Loctite 3430) and let it harden before cycling in KOH-14 between  $-0.5$  V and  $0.6$  V vs Ag/AgCl. The glued film showed first signs of break-down after 21 cycles. But although it suffered some loss of NiO layer, it remained stable until the 27<sup>th</sup> cycle, when the break started extending. The glued film showed better stability, but this little experiment cannot conclusively explain why the films broke on cycling in KOH-14.

Since the breakage generally started at the edges, the method used to cut the films from the sheet could possibly affect the films' stability. I envisage that cutting with a scissor or a razor-blade lends the cut significantly different structure (rugged, smooth, etc.). I cannot say which is best.

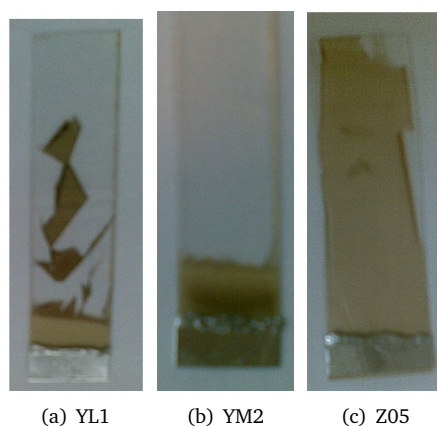


Figure 4.19: Photographs of some of the films that broke in KOH(aq). Film YL1, (a), was cycled in KOH-14 between  $-0.6$  V and  $0.5$  V vs Ag/AgCl for 18 cycles when failure became visible. By the 20<sup>th</sup> cycle, the cycling was stopped and this photo was taken. Film YM2, (b), was ozonated for 40 s prior to cycling. It was cycled using the same parameters as (a). At cycle 12, optical changes along the film edges were observed. At the 18<sup>th</sup> cycle visible onset of break-down occurred. I observed that break-down occurred primarily during the last half of the cathodic sweep, and it took three full cycles after cycle 18 for break-down to complete. Film Z05, (c), shows the breakage that occurred after ageing in KOH-14 (for a few hours), without any applied voltage. Generally when a film failed, the recorded current became zero since the electrical circuit was effectively broken.

## Conclusions

Electrochromic nickel vanadium oxide thin-films were ozonated and subsequently cycled in KOH(aq) at pH 14 (KOH-14) and pH 12 (KOH-12), and in LiClO<sub>4</sub>(PC) (LiPC). The films' optical transmittance in the visible wavelength range was monitored *in situ* during cycling.

The films exhibited a limited modulation band in LiPC, for both non-ozonated and intermediately ozonated samples. A significant increase of the modulation occurred for longer ozonation times. This extended modulation was observed to decrease slowly on cycling, eventually returning to the behaviour of a non-ozonated film. Films cycled in KOH-14, on the other hand, showed good optical

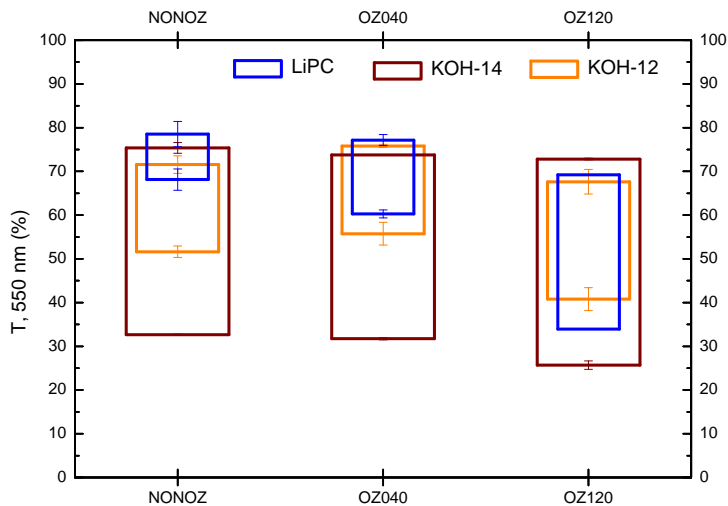


Figure 5.1: NiO could be coloured in KOH-14 and KOH-12, and ozonation increased the colouration slightly. In LiPC, non-ozonated NiO could only be bleached, but with increasing ozonation the mode of colouration switched and extensive colouration became possible. 🔍

modulation band stability, as did films cycled in KOH-12, but their mechanical stability in the alkaline environment was poor.

Charge capacities were found to decrease on ozonation in the aqueous electrolytes, but increased on ozonation, prior to cycling, in LiPC. Along with the optical modulation, this led to higher colouration efficiency (CE) in the ozonated state in all electrolytes. The general trend in each electrolyte was that ozonation increased CE. The highest CE,  $\sim 200$  mC/cm<sup>2</sup>, was observed in KOH-12 for heavily ozonated films. In that particular electrolyte the difference in CE between non-ozonated and ozonated films was also the largest (more than twice the magnitude).

In KOH-14 CE was  $\sim 130$  mC/cm<sup>2</sup> for ozonated films, and only slightly lower in LiPC. These values are comparable to results reported earlier [7, 10], and appears to be a result of the favourable chemical structure of the nickel oxide thin film.

The CE for ozonated films in LiPC is lower than in either KOH-14 or KOH-12. But the achieved CE-value still represents a tripling of the CE for non-ozonated films in LiPC. This is a potentially promising result, since most commercial electrolytes are based on lithium or PC.

The ozonation process in itself exhibited a reproducible correlation between ozonation time and optical transmittance of the nickel oxide thin film.

## 5.1 Outlook

This project draws on previous work on electrochromic nickel oxide by primarily S. Green and E. Avendaño. This work has benefited from the large amount of knowledge and technical know-how already present because of these and other workers efforts.

For future work, and based on the assumption that ozonation will be the method of choice for precharging of nickel oxide layers, I have a few suggestions, in all modesty, based on my own work on this project.

For the ozonation procedure, I believe the ability to measure the optical transmittance *in situ* (in the photoreactor during ozonation) could be useful. Additionally, I think the area of the ozonated sample affects the time needed to achieve a certain decrease in transmittance. This has implications for larger scale applications, and the ozone concentration required. On that note, actual measurements of the ozone concentration inside the photoreactor would be of scientific interest.

For the electrochemical cycling, the *in situ* spectrophotometry could be extended to feature reflectance as well, if some effort was expounded. But most importantly, the electrode configuration or possibly the cell itself should be changed so that the ohmic drops are minimised.

## Sammanfattning

I vissa material kan materialets optiska egenskaper ändras genom att påverka det elektrokemiskt i en reversibel process. Fenomenet benämns *elektrokromism*.

Den elektrokroma teknikens signum är förmågan att förändra materialets genomskinlighet steglöst, samt att materialet bara drar ström när det ska förändra sin genomskinlighet. I frånvaro av elektrisk spänning behåller det sin genomskinlighet under lång tid. Materialet har en "minneseffekt".

Ett elektrokromt material kan fås att ändra färg genom att lägga en elektrisk potential över materialet. Färgförändringen åstadkoms genom att elektrokemiskt inlagra och extrahera elektroner i materialet (alltså genom kemisk reduktion och oxidation). Eftersom den elektrokroma effekten i grunden åstadkoms av elektrontransport i materialet, krävs en konstruktion (Figur 6.1) lik den för ett uppladdningsbart batteri för att erhålla en fungerande elektrokrom anordning.

I detta arbete har ett anodiskt elektrokromt material, nickel vanadinoxid, undersökts genom cyklisk voltammetri och *in situ* spektrofotometri. Materialet har *ozonerats* (utsatts för UV-ljus i luft, UV-ljuset reagerar med syret i luften och bildar ozon,  $O_3$ ) under olika lång tid och cyklats i tre olika elektrolyter: KOH(aq) vid pH 14 och pH 12, samt litiumperklorat löst i propylenkarbonat ( $LiClO_4$ (PC)).

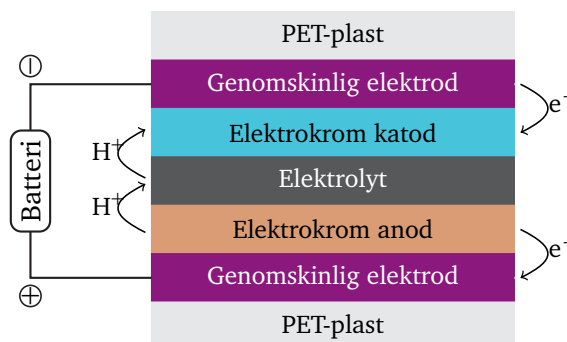


Figure 6.1: En fullständig elektrokrom anordning mellan två flexibla plastfilmer.

Resultatet från detta projekt visade på ett tydligt samband mellan ozonerings- och sänkt transmittans för oxiden ifråga. Andra egenskaper, såsom optisk modulation och laddningsmängdskapacitet vid cykling i elektrolyt, uppmättes, och ett flertal storheter härleddes ur dessa och andra experimentellt uppmätta storheter. En viktig storhet som relaterar den till materialet överförda laddningsmängden och den optiska förändring som denna laddning åstadkommer är den så kallade "colouration efficiency" (svensk motsvarighet saknas). Detta tal, CE, är direkt relaterat till materialets prestanda som elektrokrom.

Sammanfattningsvis, har detta arbete visat att ozonering är en möjlig lösning för att ladda det anodiska elektrokroma materialet till valfritt tillstånd (laddningstillståndet återspeglas i materialets transmittans enligt en kurva som har uppmätts experimentellt, se [Figur 4.4](#)).

## References

DOI<sup>®</sup>, *Digital Object Identifier*, is formatted as a hyperlink with monospaced font and dashed underline, like this [10.1016/j.mseb.2004.12.085](https://doi.org/10.1016/j.mseb.2004.12.085).

Clicking on the DOI will open that article's webpage in your browser, where you may have access to the fulltext article, depending on the publisher's terms of use.

- [1] Agency for Toxic Substances and Disease Registry (ATSDR). *Toxicological profile for nickel*. U.S. Department of Health and Human Services, Public Health Service, Atlanta, Georgia, August 2005.  
<http://www.atsdr.cdc.gov/toxprofiles/tp15.html>.
- [2] Agency for Toxic Substances and Disease Registry (ATSDR). *Toxicological profile for vanadium and compounds*. U.S. Public Health Service, Atlanta, Georgia, July 1992.  
<http://www.atsdr.cdc.gov/toxprofiles/tp58.html>.
- [3] AllBusiness.com, Inc. Aluminum-based PET catalyst bears high activity at low cost, 2003. <http://www.allbusiness.com/manufacturing/chemical-manufacturing/1114581-1.html>. Accessed on 2009-07-20.
- [4] Peter Atkins and Julio de Paula. *Atkins' Physical Chemistry*. Oxford University Press, seventh edition, 2002. ISBN 0-19-579285-9.
- [5] E. Avendaño, A. Azens, J. Isidorsson, R. Karmhag, G. A. Niklasson, and C. G. Granqvist. Optimized nickel-oxide-based electrochromic thin films. *Solid State Ionics*, 165(1-4):169-173, 2003.  
[10.1016/j.ssi.2003.08.029](https://doi.org/10.1016/j.ssi.2003.08.029).
- [6] E. Avendaño, A. Azens, G. A. Niklasson, and C. G. Granqvist. Nickel-oxide-based electrochromic films with optimized optical properties. *Journal of Solid State Electrochemistry*, 8(1):37-39, 2003.  
[10.1007/s10008-003-0405-9](https://doi.org/10.1007/s10008-003-0405-9).
- [7] E. Avendaño, A. Azens, G. A. Niklasson, and C. G. Granqvist. Electrochromism in nickel oxide films containing Mg, Al, Si, V, Zr, Nb, Ag, or Ta. *Solar Energy Materials and Solar Cells*, 84(1-4):337-350, 2004.  
[10.1016/j.solmat.2003.11.032](https://doi.org/10.1016/j.solmat.2003.11.032).
- [8] E. Avendaño, A. Azens, G. A. Niklasson, and C. G. Granqvist. Proton diffusion and electrochromism in hydrated NiO<sub>y</sub> and Ni<sub>1-x</sub>V<sub>x</sub>O<sub>y</sub> thin films. *Journal of the Electrochemical Society*, 152(12):F203-F212, 2005.  
[10.1149/1.2077308](https://doi.org/10.1149/1.2077308).

- [9] E. Avendaño, A. Kuzmin, J. Purans, A. Azens, G. A. Niklasson, and C. G. Granqvist. Changes in the local structure of nanocrystalline electrochromic films of hydrated nickel vanadium oxide upon ozone-induced coloration. *Physica Scripta*, T115:464–466, 2005. [10.1238/Physica.Topical.115a00464](https://doi.org/10.1238/Physica.Topical.115a00464).
- [10] E. Avendaño, L. Berggren, G. A. Niklasson, C. G. Granqvist, and A. Azens. Electrochromic materials and devices: Brief survey and new data on optical absorption in tungsten oxide and nickel oxide films. *Thin Solid Films*, 496(1):30–36, 2006. [10.1016/j.tsf.2005.08.183](https://doi.org/10.1016/j.tsf.2005.08.183).
- [11] E. Avendaño, H. Rensmo, A. Azens, A. Sandell, G. de M. Azevedo, H. Siegbahn, G. A. Niklasson, and C. G. Granqvist. Coloration mechanism in proton-intercalated electrochromic hydrated  $\text{NiO}_y$  and  $\text{Ni}_{1-x}\text{V}_x\text{O}_y$  thin films. *Journal of The Electrochemical Society*, 156(8):P132–P138, 2009. [10.1149/1.3148327](https://doi.org/10.1149/1.3148327).
- [12] Esteban Damián Avendaño Soto. *Electrochromism in Nickel-based Oxides: Coloration Mechanisms and Optimization of Sputter-deposited Thin Films*. Doctoral thesis, monograph, Uppsala university, 2004. <http://urn.kb.se/resolve?urn=urn:nbn:se:uu:diva-4307>.
- [13] A. Azens and C. G. Granqvist. Electrochromic smart windows: energy efficiency and device aspects. *Journal of Solid State Electrochemistry*, 7(2): 64–68, 2003. [10.1007/s10008-002-0313-4](https://doi.org/10.1007/s10008-002-0313-4).
- [14] A. Azens, G. Gustavsson, R. Karmhag, and C. G. Granqvist. Electrochromic devices on polyester foil. *Solid State Ionics*, 165(1–4):1–5, 2003. [10.1016/j.ssi.2003.08.009](https://doi.org/10.1016/j.ssi.2003.08.009). Fifth International Meeting on Electrochromism.
- [15] A. Azens, L. Kullman, and C. G. Granqvist. Ozone coloration of Ni and Cr oxide films. *Solar Energy Materials and Solar Cells*, 76:147–153, 2003. [10.1016/S0927-0248\(02\)00213-1](https://doi.org/10.1016/S0927-0248(02)00213-1).
- [16] A. Azens, E. Avendaño, J. Backholm, L. Berggren, G. Gustavsson, R. Karmhag, G. A. Niklasson, A. Roos, and C. G. Granqvist. Flexible foils with electrochromic coatings: science, technology and applications. *Materials Science and Engineering B*, 119(3):214–223, 2005. [10.1016/j.mseb.2004.12.085](https://doi.org/10.1016/j.mseb.2004.12.085).
- [17] Gianluca Baratti. Saint-Gobain Targets Energy Savers With Ferrari Glass. [http://www.bloomberg.com/apps/news?pid=20601072&sid=aCHqCmi0i\\_vE](http://www.bloomberg.com/apps/news?pid=20601072&sid=aCHqCmi0i_vE). Accessed on 2009-07-24.
- [18] F. Bardé, M. R. Palacin, B. Beaudoin, and J.-M. Tarascon. Ozonation: A Unique Route To Prepare Nickel Oxyhydroxides. Synthesis Optimization and Reaction Mechanism Study. *Chemistry of Materials*, 17(3):470–476, 2005. [10.1021/cm040133+](https://doi.org/10.1021/cm040133+).
- [19] R. Barnard, C. F. Randell, and F. L. Tye. Studies concerning charged nickel hydroxide electrodes: Part III. Reversible potentials at low states of charge. *Journal of Electroanalytical Chemistry*, 119(1):17–24, 1981. [10.1016/S0022-0728\(81\)80120-9](https://doi.org/10.1016/S0022-0728(81)80120-9).



- [20] R. Barnard, C. F. Randell, and F. L. Tye. Studies concerning charged nickel hydroxide electrodes: Part IV. Reversible potentials in LiOH, NaOH, RbOH and CsOH. *Journal of Applied Electrochemistry*, 11(4):517–523, 1981. [10.1007/BF01132440](https://doi.org/10.1007/BF01132440).
- [21] B. Beden, D. Floner, J. M. Léger, and C. Lamy. A voltammetric study of the formation on hydroxides and oxyhydroxides on nickel single crystal electrodes in contact with an alkaline solution. *Surface Science*, 162(1–3): 822–829, 1985. [10.1016/0039-6028\(85\)90985-9](https://doi.org/10.1016/0039-6028(85)90985-9).
- [22] B. Beverskog and I. Puigdomenech. Revised Pourbaix diagrams for nickel at 25–300 °C. *Corrosion Science*, 39(5):969–980, 1997. [10.1016/S0010-938X\(97\)00002-4](https://doi.org/10.1016/S0010-938X(97)00002-4).
- [23] H. Bode, K. Dehmelt, and J. Witte. Zur kenntnis der nickelhydroxidelektrode—I. Über das nickel (II)-hydroxidhydrat. *Electrochimica Acta*, 11(8):1079–1087, 1966. ISSN 0013-4686. [10.1016/0013-4686\(66\)80045-2](https://doi.org/10.1016/0013-4686(66)80045-2).
- [24] O. Bohnke, G. Frand, M. Rezrazi, C. Rousselot, and C. Truche. Fast ion transport in new lithium electrolytes gelled with PMMA. 2. Influence of lithium salt concentration. *Solid State Ionics*, 66(1–2):105–112, 1993. ISSN 0167-2738. [10.1016/0167-2738\(93\)90033-Y](https://doi.org/10.1016/0167-2738(93)90033-Y).
- [25] I. Bouessay, A. Rougier, P. Poizot, J. Moscovici, A. Michalowicz, and J.-M. Tarascon. Electrochromic degradation in nickel oxide thin film: A self-discharge and dissolution phenomenon. *Electrochimica Acta*, 50(18): 3737–3745, 2005. [10.1016/j.electacta.2005.01.020](https://doi.org/10.1016/j.electacta.2005.01.020).
- [26] A. Brazier, G. B. Appetecchi, S. Passerini, A. Surca Vuk, B. Orel, F. Donsanti, and F. Decker. Ionic liquids in electrochromic devices. *Electrochimica Acta*, 52(14):4792–4797, 2007. ISSN 0013-4686. [10.1016/j.electacta.2007.01.025](https://doi.org/10.1016/j.electacta.2007.01.025).
- [27] J. Brentano and E. O. Hoffmann. Structure of NiO. *Proceedings of the Royal Society of London, Series A: Mathematical and Physical Sciences*, 27: 184–193, 1925.
- [28] R. W. Cairns and E. Ott. X-Ray Studies of the System Nickel-Oxygen-Water. I. Nickelous Oxide and Hydroxide. *Journal of the American Chemical Society*, 55:527–533, 1933.
- [29] James F. Carlin Jr. Tin. Minerals yearbook, US Geological Survey, 2007.
- [30] James F. Carlin Jr. Tin. Mineral commodity summary, US Geological Survey, 2009.
- [31] Michael K. Carpenter and Dennis A. Corrigan. Photoelectrochemistry of Nickel Hydroxide Thin Films. *Journal of The Electrochemical Society*, 136 (4):1022–1026, 1989. [10.1149/1.2096777](https://doi.org/10.1149/1.2096777).
- [32] Michael K. Carpenter, Robert S. Conell, and Dennis A. Corrigan. The electrochromic properties of hydrous nickel oxide. *Solar Energy Materials*, 16(4):333–346, 1987. [10.1016/0165-1633\(87\)90082-7](https://doi.org/10.1016/0165-1633(87)90082-7).

- [33] Haiying Chen, Chengfeng Qiu, Huajun Peng, Zhilang Xie, Man Wong, and H. S. Kwok. Co-sputtered aluminum doped zinc oxide thin film as transparent anode for organic light-emitting diodes. *ASID*, pages 489–492, Feb 2004.
- [34] Hao-Long Chen and Yao-Sheng Yang. Effect of crystallographic orientations on electrical properties of sputter-deposited nickel oxide thin films. *Thin Solid Films*, 516(16):5590–5596, 2008. [10.1016/j.tsf.2007.07.035](https://doi.org/10.1016/j.tsf.2007.07.035).
- [35] K.-F. Chiu, C. Y. Chang, and C. M. Lin. The Electrochemical Performance of Bias-Sputter-Deposited Nanocrystalline Nickel Oxide Thin Films Toward Lithium. *Journal of The Electrochemical Society*, 152(6):A1188–A1192, 2005. [10.1149/1.1906024](https://doi.org/10.1149/1.1906024).
- [36] D. R. Crow. *Principles and applications of electrochemistry*. Chapman & Hall, fourth edition, 1994. ISBN 0-7514-0168-4.
- [37] Budhadipta Dan, Glen C. Irvin, and Matteo Pasquali. Continuous and Scalable Fabrication of Transparent Conducting Carbon Nanotube Films. *ACS Nano*, 3(4):835–843, 2009. [10.1021/nn8008307](https://doi.org/10.1021/nn8008307).
- [38] S. K. Deb. *Applied Optics Supplement*, 3:192–195, 1969. ISSN 0066-5495.
- [39] Herbert Dittrich, Peter Axmann, Margret Wohlfahrt-Mehrens, Jürgen Garche, Sven Albrecht, Julia Meese-Marktscheffel, Armin Olbrich, and Gerhard Gille. Structural study of  $\beta$ -Ni(OH)<sub>2</sub> and  $\alpha$ -Ni(OH)<sub>2</sub> variants for electrode applications. *Zeitschrift für Kristallographie*, 220(2–3):306–315, 2005. [10.1524/zkri.220.2.306.59135](https://doi.org/10.1524/zkri.220.2.306.59135).
- [40] DRYDEN AQUA. Ozone conversion factors. [http://www.drydenaqua.com/ozone/data/useful\\_ozone\\_conversion\\_factors.htm](http://www.drydenaqua.com/ozone/data/useful_ozone_conversion_factors.htm). Accessed 09-07-09.
- [41] EControl-Glas GmbH & Co. KG. Econtrol-glas, 2009. <http://www.econtrol-glas.de/58.html?&L=1>. Accessed on 2009-08-08.
- [42] Energimyndigheten. Sex projekt inbjuds konkurrera om 875 miljoner kronor. <http://www.energimyndigheten.se/sv/Press/Pressmeddelanden/Sex-projekt-inbjuds-konkurrera-om-875-miljoner-kronor/>. Accessed on 2009-06-11.
- [43] Walter Estrada, Anne M. Andersson, and Claes G. Granqvist. Electrochromic nickel-oxide-based coatings made by reactive dc magnetron sputtering: Preparation and optical properties. *Journal of Applied Physics*, 64(7):3678–3683, 1988. [10.1063/1.341410](https://doi.org/10.1063/1.341410).
- [44] Ferrari S.P.A. press release. Ferrari 575M Superamerica, 2005. <http://www.ultimatecarpage.com/car/2153/Ferrari-575M-SuperAmerica.html>. Accessed on 2009-07-24.

- [45] G. G. Fletcher, F. E. Rossetto, J. D. Turnbull, and E. Nieboer. Toxicity, uptake, and mutagenicity of particulate and soluble nickel compounds. *Environmental Health Perspectives*, 102(Supplement 3):69–79, 1994.
- [46] Heidi M. French, Mark J. Henderson, A. Robert Hillman, and Eric Vieil. Ion and solvent transfer discrimination at a nickel hydroxide film exposed to LiOH by combined electrochemical quartz crystal microbalance (EQCM) and probe beam deflection (PBD) techniques. *Journal of Electroanalytical Chemistry*, 500(1–2):192–207, 2001. [10.1016/S0022-0728\(00\)00373-9](https://doi.org/10.1016/S0022-0728(00)00373-9).
- [47] Heidi M. French, Mark J. Henderson, A. Robert Hillman, and Eric Vieil. Temporal resolution of ion and solvent transfers at nickel hydroxide films exposed to LiOH. *Solid State Ionics*, 150(1–2):27–37, 2002. [10.1016/S0167-2738\(02\)00261-8](https://doi.org/10.1016/S0167-2738(02)00261-8).
- [48] Kieran Furlong. Titanium — a real alternative to antimony catalysts in PET bottles, 2006. <http://www.jmcatalysts.com/pct/news2.asp?newsid=76>. Accessed on 2009-07-20.
- [49] Jianping Ge, Howon Lee, Le He, Junhoi Kim, Zhenda Lu, Hyoki Kim, James Goebel, Sunghoon Kwon, and Yadong Yin. Magnetochromatic Microspheres: Rotating Photonic Crystals. *Journal of the American Chemical Society*. [10.1021/ja903626h](https://doi.org/10.1021/ja903626h).
- [50] Gentex Corporation. Gentex Corporation, 2009. <http://www.gentex.com/>.
- [51] Peter Georén and Göran Lindbergh. Characterisation and modelling of the transport properties in lithium battery gel electrolytes: Part I. The binary electrolyte PC/LiClO<sub>4</sub>. *Electrochimica Acta*, 49(21):3497–3505, 2004. [10.1016/j.electacta.2004.03.020](https://doi.org/10.1016/j.electacta.2004.03.020).
- [52] R. J. Gilliam, J. W. Graydon, D. W. Kirk, and S. J. Thorpe. A review of specific conductivities of potassium hydroxide solutions for various concentrations and temperatures. *International Journal of Hydrogen Energy*, 32(3):359–364, 2007. [10.1016/j.ijhydene.2006.10.062](https://doi.org/10.1016/j.ijhydene.2006.10.062).
- [53] Marylou Gonsalves and A. Robert Hillman. Effect of time scale on redox-driven ion and solvent transfers at nickel hydroxide films in aqueous lithium hydroxide solutions. *Journal of Electroanalytical Chemistry*, 454(1–2):183–202, 1998. [10.1016/S0022-0728\(98\)00262-9](https://doi.org/10.1016/S0022-0728(98)00262-9).
- [54] C. G. Granqvist. Oxide electrochromics: Why, how, and whither. *Solar Energy Materials and Solar Cells*, 92(2):203–208, 2008. [10.1016/j.solmat.2006.10.027](https://doi.org/10.1016/j.solmat.2006.10.027). Selected Papers from the Seventh International Meeting on Electrochromism (IME-7), Seventh International Meeting on Electrochromism.
- [55] C. G. Granqvist. *Handbook of Inorganic Electrochromic Materials*. Elsevier, second edition, 1995. ISBN 0444899308. <http://books.google.com/books?id=MYd1Np3y0-8C>.

- [56] C. G. Granqvist and A. Hultåker. Transparent and conducting ITO films: new developments and applications. *Thin Solid Films*, 411(1):1–5, 2002. [10.1016/S0040-6090\(02\)00163-3](https://doi.org/10.1016/S0040-6090(02)00163-3).
- [57] C. G. Granqvist, G. A. Niklasson, and A. Azens. Electrochromics: Fundamentals and energy-related applications of oxide-based devices. *Applied Physics A: Materials Science & Processing*, 89(1):29–35, 2007. [10.1007/s00339-007-4067-9](https://doi.org/10.1007/s00339-007-4067-9).
- [58] C. G. Granqvist, S. Green, E. K. Jonson, R. Marsal, G. A. Niklasson, A. Roos, Z. Topalian, A. Azens, P. Georén, G. Gustavsson, R. Karmhag, J. Smulko, and L. B. Kish. Electrochromic foil-based devices: Optical transmittance and modulation range, effect of ultraviolet irradiation, and quality assessment by 1/f current noise. *Thin Solid Films*, 516(17): 5921–5926, 2008. [10.1016/j.tsf.2007.10.074](https://doi.org/10.1016/j.tsf.2007.10.074). Presented at 5th International Symposium on Transparent Oxide Thin Films for Electronics and Optics.
- [59] S. Green, J. Backholm, P. Georén, C. G. Granqvist, and G. A. Niklasson. Electrochromism in nickel oxide and tungsten oxide thin films: Ion intercalation from different electrolytes. *Solar Energy Materials and Solar Cells*, 2009. [10.1016/j.solmat.2009.05.009](https://doi.org/10.1016/j.solmat.2009.05.009).
- [60] Carl H. Hamann, Andrew Hamnett, and Wolf Vielstich. *Electrochemistry*. Wiley-VCH Verlag GmbH, 1998. ISBN 3-527-29095-8.
- [61] T. A. Han, J. P. Tu, J. B. Wu, Y. Li, and Y. F. Yuan. Electrochemical Properties of Biphasic Ni(OH)<sub>2</sub> Electrodes for Secondary Rechargeable Ni/MH Batteries. *Journal of the Electrochemical Society*, 153(4): A738–A742, 2006. [10.1149/1.2171829](https://doi.org/10.1149/1.2171829).
- [62] Kuo-Chuan Ho. The influence of charge capacity ratio on the performance of a complementary electrochromic system. *Solar Energy Materials and Solar Cells*, 56(3–4):271–280, 1999. [10.1016/S0927-0248\(98\)00137-8](https://doi.org/10.1016/S0927-0248(98)00137-8).
- [63] Liangbing Hu, George Gruner, Dan Li, Richard B. Kaner, and Jiri Cech. Patternable transparent carbon nanotube films for electrochromic devices. *Journal of Applied Physics*, 101(1):016102, 2007. [10.1063/1.2402330](https://doi.org/10.1063/1.2402330).
- [64] Annette Hultåker. *Transparent Conductive Tin Doped Indium Oxide: Characterisation of Thin Films Made by Sputter Deposition with Silver Additive and by Spin Coating from Nanoparticle Dispersions*. PhD thesis, Uppsala University, Department of Materials Science, 2002.
- [65] International Meeting on Electrochromism. Abstract book. In *Seventh International Meeting on Electrochromism*, Istanbul, Turkey, 2006. <http://www.fizik.itu.edu.tr/ime7/>.
- [66] R. S. Jayashree, P. Vishnu Kamath, and G. N. Subbanna. The effect of crystallinity on the reversible discharge capacity of nickel hydroxide. *Journal of The Electrochemical Society*, 147(6):2029–2032, 2000. [10.1149/1.1393480](https://doi.org/10.1149/1.1393480).

- [67] S. R. Jiang, P. X. Yan, B. X. Feng, X. M. Cai, and J. Wang. The response of a  $\text{NiO}_x$  thin film to a step potential and its electrochromic mechanism. *Materials Chemistry and Physics*, 77(2):384–389, 2002. [10.1016/S0254-0584\(02\)00010-X](https://doi.org/10.1016/S0254-0584(02)00010-X).
- [68] H. Kedesdy and A. Drukalsky. X-Ray Diffraction Studies of the Solid State Reaction in the NiO-ZnO System. *Journal of the American Chemical Society*, 76(23):5941–5946, 1954. [10.1021/ja01652a013](https://doi.org/10.1021/ja01652a013).
- [69] Per Kofstad. Defects and transport properties of metal oxides. *Oxidation of Metals*, 44(1–2):3–27, 1995. [10.1007/BF01046721](https://doi.org/10.1007/BF01046721).
- [70] Peter H. Kuck. Nickel. Mineral commodity summary, US Geological Survey, 2009.
- [71] A. Barry Kunz. Electronic structure of NiO. *Journal of Physics C: Solid State Physics*, 14(16):L455–L460, 1981. [10.1088/0022-3719/14/16/001](https://doi.org/10.1088/0022-3719/14/16/001).
- [72] Carl M. Lampert. Electrochromic materials and devices for energy efficient windows. *Solar Energy Materials*, 11(1–2):1–27, 1984. [10.1016/0165-1633\(84\)90024-8](https://doi.org/10.1016/0165-1633(84)90024-8).
- [73] Anna-Lena Larsson. *All-Thin-Film Electrochromic Devices for Optical and Thermal Modulation*. PhD thesis, Uppsala University, 2004.
- [74] Anna-Lena Larsson and Gunnar A. Niklasson. Optical properties of electrochromic all-solid-state devices. *Solar Energy Materials and Solar Cells*, 84(1–4):351–360, 2004. [10.1016/j.solmat.2004.02.051](https://doi.org/10.1016/j.solmat.2004.02.051). Presented at International Solar Energy Society World Congress 2003.
- [75] Jong-Won Lee, Jeong-Nam Han, Masahiro Seo, and Su-Il Pyun. Transport of alkaline cation and neutral species through the  $\alpha\text{-Ni}(\text{OH})_2/\gamma\text{-NiOOH}$  film electrode. *Journal of Solid State Electrochemistry*, 5(7–8):459–465, 2001. [10.1007/s100080100198](https://doi.org/10.1007/s100080100198).
- [76] Se-Hee Lee, C. Edwin Tracy, and J. Roland Pitts. Effect of Nonstoichiometry of Nickel Oxides on Their Supercapacitor Behavior. *Electrochemical and Solid-State Letters*, 7(10):A299–A301, 2004. [10.1149/1.1786233](https://doi.org/10.1149/1.1786233).
- [77] O. Legrini, E. Oliveros, and A. M. Braun. Photochemical processes for water treatment. *Chemical Reviews*, 93(2):671–698, 1993. [10.1021/cr00018a003](https://doi.org/10.1021/cr00018a003).
- [78] Kuo-Chuan Liu and Marc A. Anderson. Porous Nickel Oxide/Nickel Films for Electrochemical Capacitors. *Journal of the Electrochemical Society*, 143(1):124–130, 1996. [10.1149/1.1836396](https://doi.org/10.1149/1.1836396).
- [79] Carlos R. Magaña, Dwight R. Acosta, Arturo I. Martínez, and Jesús M. Ortega. Electrochemically induced electrochromic properties in nickel thin films deposited by DC magnetron sputtering. *Solar Energy*, 80(2):161–169, 2006. [10.1016/j.solener.2005.04.006](https://doi.org/10.1016/j.solener.2005.04.006).

- [80] MBR. USS-9200 Ultrasonic Soldering System, 2009. [http://www.sonicsolder.com/products/uss-9200\\_gb.html](http://www.sonicsolder.com/products/uss-9200_gb.html). Accessed in May 2009.
- [81] Metrohm. Metrohm Ag/AgCl reference electrodes data sheet. <http://products.metrohm.com/prod-60733100.aspx>. Accessed in May 2009.
- [82] IVL Svenska Miljöinstitutet. Övervakning av marknära ozon. <http://www3.ivl.se/miljo/projekt/ozon/>. Accessed on 2009-07-09.
- [83] Eric L. Miller and Richard E. Rocheleau. Electrochemical and electrochromic behavior of reactively sputtered nickel oxide. *Journal of the Electrochemical Society*, 144(6):1995–2003, 1997. [10.1149/1.1837734](https://doi.org/10.1149/1.1837734).
- [84] Paul M. S. Monk, Roger Mortimer, and David Rosseinsky. *Electrochromism and Electrochromic Devices*. Cambridge University Press, 2007. ISBN 978-0-521-82269-5. <http://books.google.com/books?id=FRMn49EpREoC>.
- [85] National Toxicology Program. *Report on Carcinogens — Nickel*. U.S. Department of Health and Human Services, Public Health Service, eleventh edition, 2009. <http://ntp.niehs.nih.gov/index.cfm?objectid=32BA9724-F1F6-975E-7FCE50709CB4C932>.
- [86] R. Newman and R. M. Chrenko. Optical properties of nickel oxide. *Physical Review*, 114:1507–1513, 1959. [10.1103/PhysRev.114.1507](https://doi.org/10.1103/PhysRev.114.1507).
- [87] Gunnar A. Niklasson and Claes G. Granqvist. Electrochromics for smart windows: thin films of tungsten oxide and nickel oxide, and devices based on these. *Journal of Materials Chemistry*, 17:127–156, 2007. [10.1039/b612174h](https://doi.org/10.1039/b612174h). Feature Article.
- [88] Pavel Nikolaev, Michael J. Bronikowski, R. Kelley Bradley, Frank Rohmund, Daniel T. Colbert, K. A. Smith, and Richard E. Smalley. Gas-phase catalytic growth of single-walled carbon nanotubes from carbon monoxide. *Chemical Physics Letters*, 313(1–2):91–97, 1999. [10.1016/S0009-2614\(99\)01029-5](https://doi.org/10.1016/S0009-2614(99)01029-5).
- [89] OceanOptics, Inc. LS-1 Tungsten Halogen Light Source, 2009. <http://www.oceanoptics.com/products/ls1.asp>.
- [90] OceanOptics, Inc. S2000 Miniature Fiber Optic Spectrometer. <http://www.oceanoptics.com/technical/engineering/S20000EMDataSheet.pdf>.
- [91] P. Oliva, J. Leonardi, J. F. Laurent, C. Delmas, J. J. Braconnier, M. Figlarz, F. Fievet, and A. de Guibert. Review of the structure and the electrochemistry of nickel hydroxides and oxy-hydroxides. *Journal of Power Sources*, 8(2):229–255, 1982. [10.1016/0378-7753\(82\)80057-8](https://doi.org/10.1016/0378-7753(82)80057-8).

- [92] Pastair AB. Kall pastörisering, 2009. <http://www.mentoronline.se/iuware.aspx?pageid=58281&ssoid=101416>. Accessed on 2009-07-20.
- [93] Derek Pletcher. *A first course in Electrode Processes*. The Electrochemical Consultancy, 1991. ISBN 0-9517307-0-3.
- [94] Derek Pletcher, James F. Rohan, and Andrew G. Ritchie. Microelectrode studies of the lithium/propylene carbonate system — Part I. Electrode reactions at potentials positive to lithium deposition. *Electrochimica Acta*, 39(10):1369–1376, 1994.
- [95] R. J. Powell and W. E. Spicer. Optical Properties of NiO and CoO. *Physical Review B*, 2(6):2182–2193, 1970. [10.1103/PhysRevB.2.2182](https://doi.org/10.1103/PhysRevB.2.2182).
- [96] Su-Il Pyun, Kwang-Hoon Kim, and Jeong-Nam Han. Analysis of stresses generated during hydrogen extraction from and injection into Ni(OH)<sub>2</sub>/NiOOH film electrode. *Journal of Power Sources*, 91(2):92–98, 2000. [10.1016/S0378-7753\(00\)00464-X](https://doi.org/10.1016/S0378-7753(00)00464-X).
- [97] YuanQiao Rao, Jehuda Greener, Carlos A. Avila-Orta, Benjamin S. Hsiao, and Thomas N. Blanton. The relationship between microstructure and toughness of biaxially oriented semicrystalline polyester films. *Polymer*, 49(10):2507–2514, 2008. [10.1016/j.polymer.2008.03.046](https://doi.org/10.1016/j.polymer.2008.03.046).
- [98] Carl-Gustaf Ribbing. Introduction to material optics. Compendium. Department of Solid State Physics, Uppsala University.
- [99] D. R. Rosseinsky and R. J. Mortimer. Electrochromic Systems and the Prospects for Devices. *Advanced Materials*, 13(11):783–793, 2001. [10.1002/1521-4095\(200106\)13:11<783::AID-ADMA783>3.0.CO;2-D](https://doi.org/10.1002/1521-4095(200106)13:11<783::AID-ADMA783>3.0.CO;2-D).
- [100] SAGE Electrochromics, Inc. Sageglass® windows, 2009. <http://www.sage-ec.com/index.html>. Accessed on 2009-08-08.
- [101] Saint-Gobain Sekurit. Electrochromic glass, 2009. <http://www.saint-gobain-sekurit.com/en/index.asp?nav1=PR&id=372>. Accessed on 2009-08-08.
- [102] Neerja Saran, Kunjal Parikh, Dong-Seok Suh, Edgar Munoz, Harsha Kolla, and Sanjeev K. Manohar. Fabrication and characterization of thin films of single-walled carbon nanotube bundles on flexible plastic substrates. *Journal of the American Chemical Society*, 126(14):4462–4463, 2004. [10.1021/ja037273p](https://doi.org/10.1021/ja037273p).
- [103] William Shotyk, Michael Krachler, and Bin Chen. Contamination of Canadian and European bottled waters with antimony from PET containers. *Journal of Environmental Monitoring*, 8:288–292, 2006. [10.1039/b517844b](https://doi.org/10.1039/b517844b).
- [104] D. F. Shriver and P. W. Atkins. *Inorganic Chemistry*. Oxford University Press, third edition, 1999. ISBN 0-19-850330-X.



- [105] Deepika Singh. Characteristics and Effects of  $\gamma$ -NiOOH on Cell Performance and a Method to Quantify It in Nickel Electrodes. *Journal of The Electrochemical Society*, 145(1):116–120, 1998. [10.1149/1.1838222](https://doi.org/10.1149/1.1838222).
- [106] N. Smith. The structure of thin films of metallic oxides and hydrates. *Journal of the American Chemical Society*, 58(1):173–179, 1936.
- [107] Peter Frederick Smith. *Sustainability at the Cutting Edge: Emerging technologies for low energy buildings*. Elsevier, second edition, 2007. ISBN 0750683007. <http://books.google.com/books?id=BGCSy7EilnQC>.
- [108] J. S. E. M. Svensson and C. G. Granqvist. Electrochromic hydrated nickel oxide coatings for energy efficient windows: Optical properties and coloration mechanism. *Applied Physics Letters*, 49(23):1566–1568, 1986. [10.1063/1.97281](https://doi.org/10.1063/1.97281).
- [109] Amy C. Tolcin. Indium. Minerals yearbook, US Geological Survey, 2007.
- [110] Amy C. Tolcin. Indium. Mineral commodity summary, US Geological Survey, 2009.
- [111] Japan Chemical Week. Al-based polyester catalyst. *Focus on Catalysts*, (6): 5–6, 2004. [10.1016/S1351-4180\(04\)00363-0](https://doi.org/10.1016/S1351-4180(04)00363-0).
- [112] M. Wehrens-Dijksma and P. H. L. Notten. Electrochemical quartz microbalance characterization of Ni(OH)<sub>2</sub>-based thin film electrodes. *Electrochimica Acta*, 51(18):3609–3621, 2006. [10.1016/j.electacta.2005.10.022](https://doi.org/10.1016/j.electacta.2005.10.022). Review Article.
- [113] J. Wiszniowski, D. Robert, J. Surmacz-Gorska, K. Miksch, and J. V. Weber. Landfill leachate treatment methods: A review. *Environmental Chemistry Letters*, 4(1):51–61, 2006. [10.1007/s10311-005-0016-z](https://doi.org/10.1007/s10311-005-0016-z).
- [114] Jens Wohlers, In-Ock Koh, Wolfram Thiemann, and Wolfgang Rotard. Application of an air ionization device using an atmospheric pressure corona discharge process for water purification. *Water, Air, & Soil Pollution*, 196(1–4):101–113, 2009. [10.1007/s11270-008-9760-6](https://doi.org/10.1007/s11270-008-9760-6).
- [115] Zhuangchun Wu, Zhihong Chen, Xu Du, Jonathan M. Logan, Jennifer Sippel, Maria Nikolou, Katalin Kamaras, John R. Reynolds, David B. Tanner, Arthur F. Hebard, and Andrew G. Rinzler. Transparent, Conductive Carbon Nanotube Films. *Science*, 305(5688):1273–1276, 2004. [10.1126/science.1101243](https://doi.org/10.1126/science.1101243).
- [116] R. W. G. Wyckoff. Rocksalt structure. *Crystal Structures*, 1:85–237, 1963.
- [117] Wei Xing, Feng Li, Zi feng Yan, and G. Q. Lu. Synthesis and electrochemical properties of mesoporous nickel oxide. *Journal of Power Sources*, 134(2):324–330, 2004. [10.1016/j.jpowsour.2004.03.038](https://doi.org/10.1016/j.jpowsour.2004.03.038).



- [118] Hu Xingfang, Chen Xiaofeng, and Song Xiangyun. Structure study on electrochromic films of nickel oxide. In Carl M. Lampert, editor, *Optical Materials Technology for Energy Efficiency and Solar Energy Conversion XII*, volume 2017, pages 172–181, San Diego, California, USA, 1993. SPIE — The International Society for Optical Engineering. [10.1117/12.161957](https://doi.org/10.1117/12.161957).
- [119] Zhang Xuping and Chen Guoping. The microstructure and electrochromic properties of nickel oxide films deposited with different substrate temperatures. *Thin Solid Films*, 298(1–2):53–56, 1997. [10.1016/S0040-6090\(96\)09110-9](https://doi.org/10.1016/S0040-6090(96)09110-9).
- [120] Young-Gi Yoon and Su-Il Pyun. Hydrogen transport through nickel hydroxide film: current transient analysis. *Electrochimica Acta*, 42(16): 2465–2474, 1997. [10.1016/S0013-4686\(96\)0043S-S](https://doi.org/10.1016/S0013-4686(96)0043S-S).
- [121] Kazuki Yoshimura, Takeshi Miki, and Sakae Tanemura. Cross-sectional observations by HRTEM of the structure of nickel oxide electrochromic thin films in the as-deposited state and the bleached state. *Materials Research Bulletin*, 32(7):839–845, 1996. [10.1016/S0025-5408\(97\)00057-3](https://doi.org/10.1016/S0025-5408(97)00057-3).
- [122] P. C. Yu, G. Nazri, and C. M. Lampert. Spectroscopic and electrochemical studies of electrochromic hydrated nickel oxide films. *Solar Energy Materials*, 16(1–3):1–17, 1987. [10.1016/0165-1633\(87\)90003-7](https://doi.org/10.1016/0165-1633(87)90003-7).
- [123] Shi Yueyan, Zhou Zhiyang, and Yang Xiaoji. Electrochromic properties of  $\text{NiO}_x\text{H}_y$  thin films. *Solar Energy Materials and Solar Cells*, 71(1):51–59, 2002. [10.1016/S0927-0248\(01\)00043-5](https://doi.org/10.1016/S0927-0248(01)00043-5).



# Method

## A.1 Handling and storage

### Handling

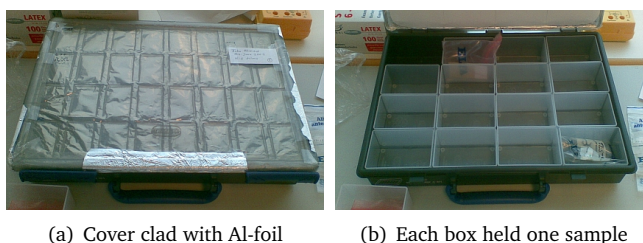
The following is an outline of the preparation steps:

1. The sheet was covered on both sides with protective transparent plastic sheets, forming a “sandwich” with the sputtered sheet in the middle.
2. The sheet sandwich (which was still transparent) was placed on a plastic measuring and cutting pad with millimeter markings.
3. The plastic sandwich was cut completely through with a segmented-blade Stanley knife, using, e.g., the cutting scheme of [Figure 3.2](#).
  - a) The sheet was cut so the electric tape could be applied and soldered along the width of the sheet in one application.
  - b) Then the taped sections were cut into strips, see [Figure 3.2\(b\)](#).
4. The electrical resistance along each strip was measured with an ohmmeter. Not a necessary step.
5. Finally the electrodes were produced by cutting down the middle of each strip (every strip makes two film electrodes).

Soldering was done with an USS-9200 Ultrasonic Soldering System, from MBR Electronics GmbH [80] with an ultrasonic frequency of 60 kHz and tip temperature  $\sim 220^\circ\text{C}$ .

### Storage

The storage solution consisted of slightly customised Raaco service cases. Nothing fancy, really, just what was at hand. The important thing to note is that storage was protected from light, at ambient temperature, and in ambient atmosphere (although circulation should have been limited due to the layer-upon-layer enclosure of the sample).



(a) Cover clad with Al-foil

(b) Each box held one sample

Figure A.1: The storage system consisted of Raaco boxes, as shown in the photo, customised by cladding the inside of the cover with aluminium foil. Each film electrode was stored inside a zip-locked ESD-shielding bag, and the plastic bag was stored inside a box as shown in the photo.

Table A.1: Prepared electrolytes.

	Electrolyte conc., mol/L	pH	Solution vol., L
KOH(aq)	1.0	14	1.0
KOH(aq)	$1.0 \cdot 10^{-2}$	12	0.99
KOH(aq)	$1.0 \cdot 10^{-4}$	10	1.0
Li(PC)	1.0	–	0.50

## A.2 Preparation of electrolytes

KOH(s) from the same batch (potassium hydroxide pellets, pro analysi, 1 kg, Merck) for all aqueous electrolytes.

### A.2.1 Preparation of KOH(aq), 1 mol/L

56.2836 g of KOH(s) was weighed on a plastic petridish. Empty petridish weighed 7.3526 g, petridish and pellets weighed 63.6362 g. The pellets were transferred to a 1000 mL flask containing some water. Deionised water was used. After complete dissolution of the base, and after adjusting the solution volume to the mark, the alkaline solution was transferred to a plastic (PP) bottle for storage.

### A.2.2 Preparation of KOH(aq), 0.01 mol/L

571.0 mg of KOH(s) (plastic balance pan plus pellets: 1.086 g, empty balance pan: 0.5150 g) was added to 1000 mL volumetric flask. Used exclusively deionised water from the clean-room's dedicated supply. The base was completely dissolved, and the volume filled to the mark. The solution was then transferred to a polypropylene flask.

### A.2.3 Preparation of KOH(aq), 0.1 mmol/L

10 mL of the  $0.01 \text{ molL}^{-1}$  solution was transferred with a volumetric pipette to a 1000 mL volumetric flask, and then diluted to the mark. Used exclusively deionised water from the clean-room's dedicated supply.

Table A.2: Perkin Elmer  $\lambda 9$  settings.

ORD/ABSC MODE	%T
SLIT	2.00 NM
SCAN SPEED	120 NM/MIN
RESPONSE	2 S
ABSC	300-2500 NM
LAMP/DET	319.2/860.8 NM

#### A.2.4 Preparation of LiPC, 1 mol/L

Solution prepared in glovebox under protective argon atmosphere. 53.20 g of anhydrous lithium chlorate,  $\text{LiClO}_4$ , was dissolved in propylene carbonate (PC) and diluted to 500 mL in a volumetric flask.

### A.3 Some experimental notes

The Ag/AgCl reference electrode used in all aqueous electrolyte experiments was a Metrohm 8.109.1156, article number 6.0733.100 [81], filled with  $c(\text{KCl})=3$  mol/L. The reference electrode had a ceramic pin diaphragm, a resistance of 3 k $\Omega$ , and a required minimum immersion depth of 5 mm, which was fulfilled in all experiments.

The starting sequence of an *in situ* spectroscopy electrochemical experiment usually proceeded as follows. After the computers and instruments were started and ready, and after letting the LS-1 lamp warm-up for at least 30 minutes, the electrochemical cycling was started first, and immediately afterwards the S2000 spectrometer was started.

Spectra recording on the Perkin Elmer  $\lambda 9$  was always preceded by a back correction at least once per day.

All (and I mean *all and every one*) spectroscopic measurements reported in this work had the nickel oxide layer facing the spectrometer lamp. Which side of the film that faced the lamp had major affect on reflectance measurements, but only a marginal effect on transmittance measurements. Again, all reported spectra and measurements were with the NiO layer facing the spectrometer lamp.



Figure A.2: Mettler H18 chemical balance.



## Analysis of primary data

Data analysis was mainly performed using MATLAB<sup>®</sup> and Origin Pro software, both kindly provided by Uppsala university. To a lesser extent OpenOffice Calc and Microsoft Excel was used.

The purpose of the written MATLAB<sup>®</sup> scripts were to harmonise data recorded from different instruments to a single format, and additionally some scripts extract useful data from the usually large experimental datasets.

### B.1 MATLAB M-functions

Below, MATLAB code is displayed with a gray background. Please note that displayed code is not always complete M-functions; code that is not part of the main algorithm is stripped out. The full, complete M-functions can be displayed by clicking the magnifying glass symbol at each heading.

**Disclaimer:** The MATLAB code shown in this report is presented mainly to allow opponents and anyone else interested in validating my results to do so. It is presented as-is. Note that the code was written to address specific problems, which sometimes resulted in certain parameters (such as file paths, number of expected columns, etc.) being hard-coded into the functions. Not very elegant, but it got the job done. The author is available if you have any questions regarding algorithms or surrounding code.

#### B.1.1 Input file formats

The raw data collected by the instruments and recorded with various proprietary computer software, were all in ASCII text format, although their disposition varied depending on the type of instrument and experiment.

The experiment that generates the largest amount of data is the cyclic voltammetry with *in situ* optical measurement. Electrical current and optical transmittance was typically logged once every few seconds, and an experiment could last for around an hour. Additionally, optical intensities were logged at several wavelengths simultaneously.

We have a finite number of input data formats. These (below) are the main data formats produced from experiments.

- OceanOptic spectrophotometer
  - \*.XY, optical spectra, wavelength (nm) vs intensity (0 – 100).
  - \*.TIME, optical intensity at some wavelengths (at least two columns, time and optical intensity for a specific wavelength).
- $\lambda 9$  spectrophotometer
  - \*.XY, optical spectra, wavelength (nm) vs intensity (0 – 1).
- AUTOLAB potentiostat
  - \*.OCW, cyclic voltammogram, potential (V) vs current (A).
  - \*.Q&Q, charge (C) per scan.

### B.1.2 MultiplyOpticColumn 🔍

We have optical spectra, which boil down to a two-column file with wavelength versus intensity. The intensity values can have different scales, e.g., 0 – 1 or 0 – 100 depending on instrument. I chose to use the 0 – 100 scale overall, which meant that spectra from the Perkin Elmer  $\lambda 9$  needed to be multiplied by a factor 100. This conversion was achieved through the `MultiplyOpticColumn` function (Table B.1).

Table B.1: `MultiplyOpticColumn.m` — Multiplies optical intensity from  $\lambda 9$  by a factor one hundred.

```

1 function MultiplyOpticColumn(file_with_full_path)
2 %Multiplies Y column with a factor 100.
3 %—— OVERWRITES ORIGINAL FILE.
4 format long;
5
6 [x,y] = xyreader(file_with_full_path);
7 y = y*100;
8
9 for k = 1:length(x)
10 file_contents(1:2,k) = [x(k);y(k)];
11 end
12
13 fid = fopen(file_with_full_path, 'wt');
14 count = fprintf(fid, '%4.0f_%8.4f\n', file_contents);
15 status = fclose(fid);
16 exit

```

### B.1.3 xyreader 🔍

The `MultiplyOpticColumn` function internally calls the `xyreader` (Table B.2) function, which was written to fetch numerical data from two arbitrarily long columns, assuming the leftmost column was  $x$ -values and the other  $y$ -values. This function was used to read all input data formats, except for \*.TIME and \*.Q&Q formats.

### B.1.4 xmultiyreader 🔍

Data from \*.TIME files was read with the `xmultiyreader` function (Table B.3). This function returns the file contents as two arrays, the first is a vector ( $x$ -values) and the second is a six-column array with intensity data.



Table B.2: `xyreader.m` — Reads two-column ASCII data and returns two arrays.

```

1 function [x,y] = xyreader(file_with_path)
2 format long;
3
4 fid = fopen(file_with_path, 'rt');
5
6 rn=0;
7 while 1
8   rn=rn+1;
9   file_as_cell{rn} = fgetl(fid);
10  if ~ischar(file_as_cell{rn})
11    break;
12  end
13 end
14
15 for k = 1:rn-1
16   file_as_numbers(k,1:2) = str2num(file_as_cell{k});
17 end
18 y = file_as_numbers(:,2);
19 x = file_as_numbers(:,1);
20 status = fclose(fid);

```

Table B.3: `xmultiyreader.m` — Reads data file with several Y columns (specifically, transmission (several channels) vs time data).

```

1 function [x,y] = xmultiyreader(file_with_path)
2 format long;
3
4 fid = fopen(file_with_path, 'rt');%t for text-mode
5 rn=0;
6 while 1
7   rn=rn+1;
8   file_as_cell{rn} = fgetl(fid);
9   if ~ischar(file_as_cell{rn})%Look for EOF
10    break;
11  end
12 end
13
14 %skips first row, header
15 for k = 2:rn-1
16   file_as_numbers(k-1,1:7) = str2num(file_as_cell{k});
17 end
18
19 y = file_as_numbers(:,2:7);
20 x = file_as_numbers(:,1);
21
22 status = fclose(fid);

```

### B.1.5 qqreader 🔍

Data from \*.Q&Q files was read with the `qqreader` (Table B.4). This function reads the multi-column file and returns four arrays containing the following quantities: positive charge, negative charge, positive charge plus negative charge, and arithmetic average (always positive) of positive and negative charge. Note that the unit is still Coulomb.

### B.1.6 chargecollector 🔍

See Table B.5.

### B.1.7 unfoldcv 🔍

See Table B.6.

Table B.4: qqreader.m — Fetches charge data from file.

```

1 function [qp,qm,dq,qa] = qqreader(file_with_path)
2
3 format long;
4 fid = fopen(file_with_path, 'rt');
5
6 rn=0;
7 while 1
8   rn=rn+1;
9   file_as_cell{rn} = fgetl(fid);
10  if ~ischar(file_as_cell{rn})
11    break;
12  end
13 end
14
15 for k = 2:rn-1
16   file_as_numbers(k-1,1:3) = str2num(file_as_cell{k});
17 end
18
19 scannr = file_as_numbers(:,1);
20 qp = file_as_numbers(:,2);
21 qm = file_as_numbers(:,3);
22 dq = qp+qm;
23 qa = (abs(qp)+abs(qm))/2;
24
25 status = fclose(fid);

```

Table B.5: chargecollector.m — Manages charge data.

```

1 function chargecollector(FolderName)
2
3 [qplus, qminus, qdelta, qavg] = qqreader(path_and_file_string);
4 area = GetArea(area_path);
5
6 qpCcm = qplus./area;
7 qmCcm = qminus./area;
8 qdCcm = qdelta./area;
9 qaCcm = qavg./area;
10
11 qpmCcm = qpCcm*1000;
12 qmmCcm = qmCcm*1000;
13 qdmCcm = qdCcm*1000;
14 qamCcm = qaCcm*1000;
15
16 scannr = [1:length(qpmCcm)];
17 scannr = transpose(scannr);
18
19 for k = 1:length(scannr)
20   output_file_contents(k,1:5) = [scannr(k);qpmCcm(k);qmmCcm(k);qdmCcm(k);qamCcm(k)];
21 end
22
23 fid = fopen(output_path_and_file_string, 'wt');
24 for lof = 1:length(scannr)
25   cout = fprintf(fid, '%-2.0d_%12.8f_%12.8f_%12.8f_%12.8f\n', output_file_contents(lof,1:5));
26 end
27 status = fclose(fid);
28 exit

```

### B.1.8 foldoptic

Optical transmittance, as recorded with OceanOptics spectrometer and software, was set to be recorded every five seconds.\* By inspection of the recorded \*.TIME files I found that this was not exactly upheld by the OceanOptics software. On average (over all experiments), the interval time was slightly larger than the specified, and additionally the interval time during a single experiment was not constant, but fluctuated around the setpoint value.  $5.16 \pm 0.09$  s (calculated as shown on lines 29–31 in Table B.7). Over the course of an experiment, this deviation amplifies.

\*For all experiments except for V-series, which had an interval time of one second ( $1.22 \pm 0.06$  s).

Table B.6: `unfoldcv.m` — Unwraps the cyclic voltammograms.

```

1 function unfoldcv(FolderName, ScanMax)
2
3 for ScanIndex = 1:str2num(ScanMax)
4 [x,y] = xyreader(path_and_file_string);
5
6 [max_x_value, max_x_row_number] = max(x);
7 [min_x_value, min_x_row_number] = min(x);
8 [max_y_value, max_y_row_number] = max(y);
9 [min_y_value, min_y_row_number] = min(y);
10
11 upy = [y(min_x_row_number:max_x_row_number-1)];
12 downy = [y(max_x_row_number:end); y(1:min_x_row_number-1)];
13 complete_y = [upy; downy];
14 upx = [x(min_x_row_number:max_x_row_number-1)];
15 downx = [x(max_x_row_number:end); x(1:min_x_row_number-1)];
16 for m = 1:length(downx)
17     downx(m) = max_x_value+(max_x_value-downx(m));
18 end
19 complete_x = [upx; downx];
20
21 for n = 1:length(complete_x)
22     complete_x(n) = complete_x(n) + (0 - min_x_value);
23 end
24
25 complete_x = complete_x*(1/(complete_x(2)-complete_x(1)));
26 step_x = (ScanIndex-1)*(complete_x(2)-complete_x(1));
27 addterm = (ScanIndex-1)*complete_x(end);
28 complete_x = complete_x + addterm + step_x;
29
30 [max_compx_value, max_compx_row_number] = max(complete_x);
31 [min_compx_value, min_compx_row_number] = min(complete_x);
32 [max_compy_value, max_compy_row_number] = max(complete_y);
33 [min_compy_value, min_compy_row_number] = min(complete_y);
34
35 for k = 1:length(x)
36     output_file_contents(1:2,k) = [complete_x(k); complete_y(k)];
37 end
38
39 exit

```

This fluctuation of the interval time is carried over into the folded optical transmittance, causing plots of folded optical transmittivity cycles of the same experiment to have slightly different endpoints, and further, those endpoints may not correspond exactly to the endpoints of the cyclic voltammogram. This inexactness on the behalf of the folded optical transmittance curve is due primarily to the inexact interval time during primary data collection. One way to reduce this problem would have been to increase the sampling rate (i.e., record transmittance values more often) or combine the presented algorithm with a spline function.

$T_b$  and  $T_c$  are defined as the transmittance values at the extreme points (minima and maxima, respectively) for each CV scan.

### B.1.9 `GetArea`

See Table B.8.

### B.1.10 `multiplyoncolumn`

See Table B.9.

Table B.7: foldopt.i.c.m — Takes optical intensity vs time and transforms it to intensity vs potential.

```

1function foldoptic(FolderName)
2format long;
3
4%fetch one scan, EC data
5[volt, current] = xreader(fullfile(OCWPathName,
6OCWFileName));
7[Voltmax, Vmaxindex] = max(volt);
8VoltStart = volt(1);
9VoltEnd = volt(end);
10
11VoltageSpan = Voltmax-Voltmin;
12CycleLengthVolt = 2*VoltageSpan;
13scanspeed_vector = abs(diff(volt));
14ScanSpeed = mean(scanspeed_vector);
15CycleLength = CycleLengthVolt/ScanSpeed;
16
17for j = 1:length(volt)
18 VoltShifted(j,1) = volt(j)-Voltmin;
19end
20VoltShiftedTime = VoltShifted./ScanSpeed;
21[VSTmin, VSTminPOS] = min(VoltShiftedTime);
22[VSTmax, VSTmaxPOS] = max(VoltShiftedTime);
23VSTstart = VoltShiftedTime(1);
24VSTend = VoltShiftedTime(end);
25
26[time, INTENSITYallChannels] = xmultireader(
27FullPathTimeFile);
28timeModulus = INTENSITYallChannels(:,3);
29TimeStepVector = mod(time, CycleLength);
30MeanTimeStep = mean(TimeStepVector);
31StdDevTimeStep = std(TimeStepVector);
32
33breakrow = 0;
34for row = 1:length(time)
35 if row > 1
36 if timeModulus(row) < timeModulus(row-1)
37 RowNumber(row,1) = row;
38 else
39 RowNumber(row,1) = 0;
40 end
41 else %row = 1
42 RowNumber(row,1) = 1;
43 end
44end
45RowNumber(end,1) = row;
46RowNumber = nonzeros(RowNumber);
47RowNrDiff = diff(RowNumber);
48
49loopcounter = 0;
50for cycles = 1:length(RowNrDiff)
51 for rn = 1:RowNrDiff(cycles)
52 loopcounter = loopcounter+1;
53 OptIntPerCycle(rn, cycles) = OptIntLumWL(loopcounter);
54 end
55end
56
57[rows, cols] = size(OptIntPerCycle);
58for cycle = 1:cols
59 [maxoptint(cycle), maxoptintpos(cycle)] = max(
60 OptIntPerCycle(:, cycle));
61 [minoptint(cycle), minoptintpos(cycle)] = min(nonzeros(
62 OptIntPerCycle(:, cycle)));
63end
64loopcounter = 0;
65for rn = 1:RowNrDiff(cycles)
66 loopcounter = loopcounter+1;
67 timePerCycle(rn, cycles) = time(loopcounter);
68 end
69end
70
71[rows, cols] = size(timePerCycle);
72for c = 1:cols
73 for r = 1:rows
74 startconst = timePerCycle(1, c);
75 if timePerCycle(r, c)
76 TPC(r, c) = timePerCycle(r, c)-startconst;
77 else
78 TPC(r, c) = 0;
79 end
80 end
81end
82
83%first inflection point
84[rows, cols] = size(TPC);
85for c = 1:cols
86 startrow(c) = 1;
87 while (TPC(startrow(c), c) < VSTstart) && (startrow(c)
88 < rows)
89 startrow(c) = startrow(c)+1;
90 startrow(c) = startrow(c)-1;
91end
92%second inflection point
93[rows, cols] = size(TPC);
94for c = 1:cols
95 maxrow(c) = 1;
96 while (TPC(maxrow(c), c) < (VSTmax+VSTstart)) && (
97 maxrow(c) < rows)
98 maxrow(c) = maxrow(c)+1;
99 end
100end
101
102% - "Folding" at inflection points
103[rows, cols] = size(TPC);
104for c = 1:cols
105 for r = 1:rows
106 if (r > 1) && (TPC(r, c))
107 if r <= startrow(c)
108 TPC(r, c) = -TPC(r, c);
109 startconst(c) = -TPC(startrow(c), c);
110 else if r <= maxrow(c)
111 TPC(r, c) = 2*startconst(c) + TPC(r, c);
112 oldmaxconst(c) = TPC(r, c);
113 maxconst(c) = TPC(r, c);
114 else
115 TPC(r, c) = maxconst(c) - (TPC(r, c) - oldmaxconst(
116 c));
117 end
118 end
119 end
120end
121
122TPCPV = TPC*ScanSpeed;
123[rows, cols] = size(TPCPV);
124for c = 1:cols
125 for r = 1:rows
126 if TPCPV(r, c) || (r==1)
127 TPCPV(r, c) = TPCPV(r, c)+VoltStart;
128 else
129 TPCPV(r, c) = 0;
130 end
131 end
132end
133
134exit

```

Table B.8: `GetArea.m` — Fetches sample area information from file.

```

1 function [area] = GetArea(area_path)
2 format long;
3
4 area_file_name = 'SampleArea.txt';
5 if area_path(end) == '\\'
6   area_path_and_file_string = [area_path, area_file_name];
7 else
8   area_path_and_file_string = [area_path, '\\', area_file_name];
9 end
10
11 fid = fopen(area_path_and_file_string, 'rt');
12 rn=0;
13 while 1
14   rn=rn+1;
15   file_as_cell{rn} = fgetl(fid);
16   if ~ischar(file_as_cell{rn})
17     break;
18   end
19 end
20
21 if file_as_cell{1}(1:3) == 'N/A'
22   area = 1;
23 else
24   for k = 1:rn-1
25     area(k,1) = str2num(file_as_cell{k});
26   end
27 end

```

Table B.9: `multiplyoncolumn.m` — Adjusts all values in one column with respect to sample area and factor one-thousandth.

```

1 function [adjusted_column] = multiplyoncolumn(column, area)
2 %Adjusts Y column of ECC scans to sample area.
3 format long;
4 area_adjusted_column = column./area;
5 milliamp_adjusted_column = 1000;
6 adjusted_column = milliamp_adjusted_column*area_adjusted_column;

```



## Results

This supplement contains all those plots that never earned a place in the main part, but still need to be shown for completeness. All plots can be accessed separately using the magnifying glass symbol in their captions.

First, two plots on charge capacity are shown. That is followed by five figures with bleached and coloured state transmittance measured *in situ*, and optical modulation curves for one experiment in each electrolyte. That in turn, is followed by five figures with colouration efficiencies, recorded both *in situ* and *ex situ*, and for the latter case results of using both the complete CE formula (Equation 2.20) and the shortened CE formula (Equation 2.21) are shown.

Then comes the results that fulfill the completeness criterium above. This is 14 figures, from Figure C.13–C.26, displaying primary CV and *in situ* optical data as recorded, for the first CV cycle and for a CV cycle at steady state (usually cycle number nine) for all CV experiments. These figures show the primary experimental data (except actual data consists of all cycles, not just two cycles; but showing all cycles would only confuse) from which all other electrochemical quantities can be derived, in theory.

Finally, one table and four plots detail the as-deposited state optical transmittance for films from all series, and another plot shows the measured transmittance increase for a number of ozonated films while being exposed to air for 200 seconds.

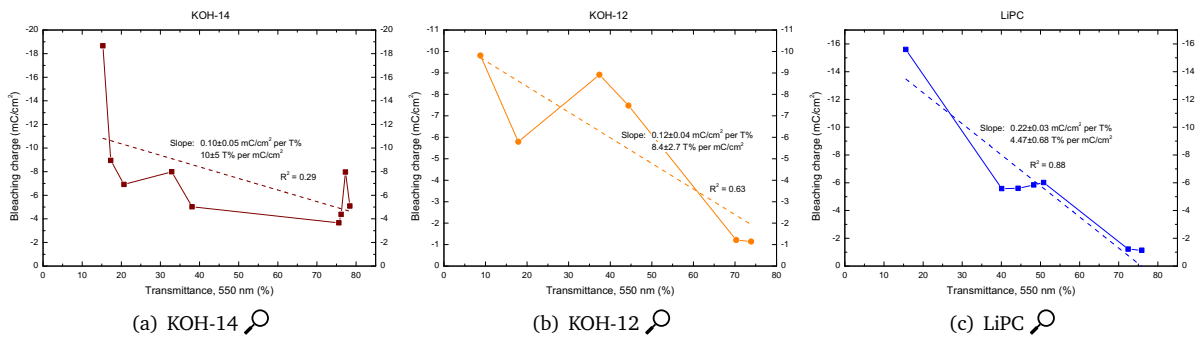


Figure C.1: Bleaching charge (cathodic charge capacity) versus transmittance at 550 nm, for varying degree of ozonation (represented by the measured transmittance after ozonation) in (a) KOH-14, (b) KOH-12, and (c) LiPC.

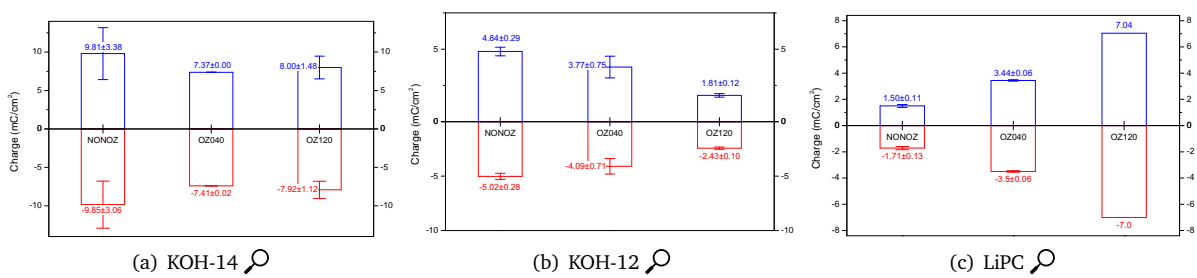


Figure C.2: Anodic (blue) and cathodic (red) charge capacities at stable cycles for NONOZ, OZ040 and OZ120 films in (a) KOH-14, (b) KOH-12, and (c) LiPC.



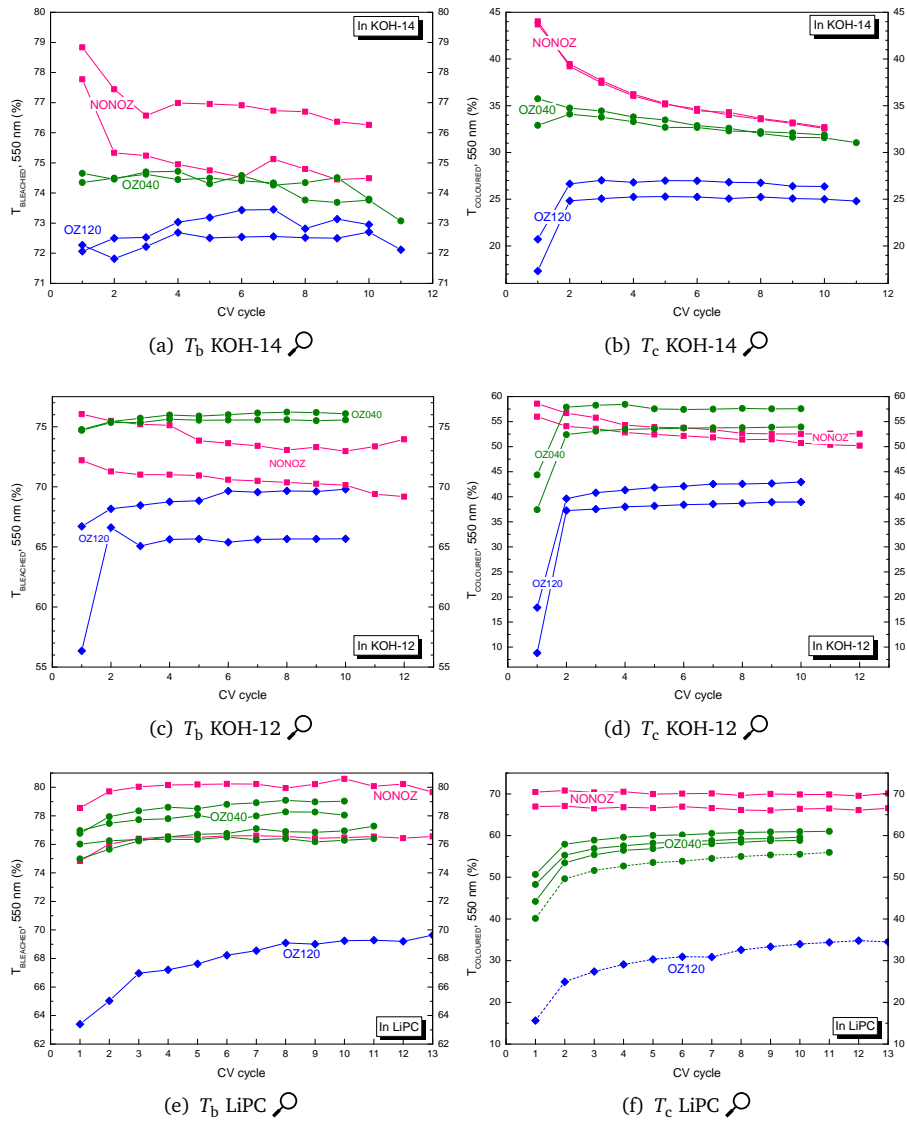


Figure C.3: Bleached state transmittance at 550 nm ( $T_b$ ) for NONOZ, OZ040, and OZ120 films cycled in (a) KOH-14, (c) KOH-12, and (e) LiPC. Coloured state transmittance at 550 nm ( $T_c$ ) for NONOZ, OZ040, and OZ120 films cycled in (b) KOH-14, (d) KOH-12, and (f) LiPC.

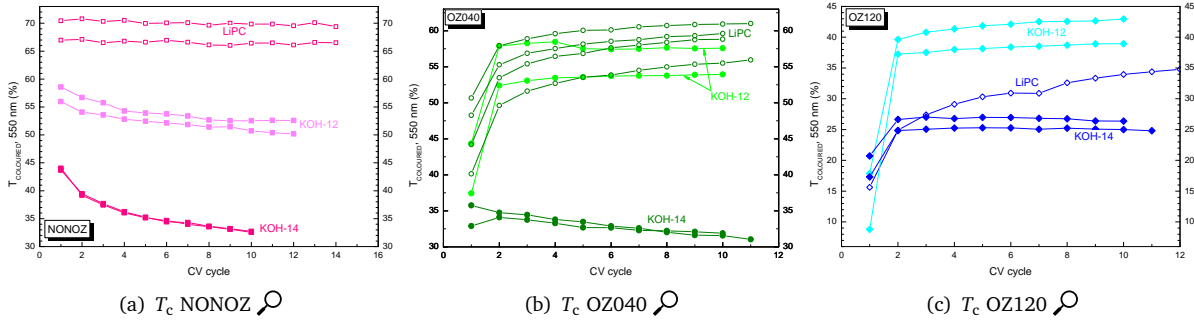


Figure C.4: (a) shows  $T_c$  at 550 nm across electrolytes for non-ozonated films versus CV cycles. Coloured state becomes darker on cycling in KOH-14 and KOH-12, but shows good stability at high transmittance in LiPC. (b) shows  $T_c$  at 550 nm across electrolytes for OZ040 films versus CV cycles.  $T_c$  decreases in KOH-14, but increases in KOH-12 to levels comparable with NONOZ films after just one cycle. Intermediate ozonation has no lasting effect on  $T_c$  in LiPC. (c) shows  $T_c$  at 550 nm across electrolytes for OZ120 films versus CV cycles. Both KOH-14 and KOH-12 cause initial increase of  $T_c$ , but  $T_c$  appears to stabilise at levels below the stable levels for non-ozonated films. OZ120 thus decreases  $T_c$  in these electrolytes.  $T_c$  in LiPC increases quite a lot after the first cycle, and then increases more slowly but steadily for every cycle.

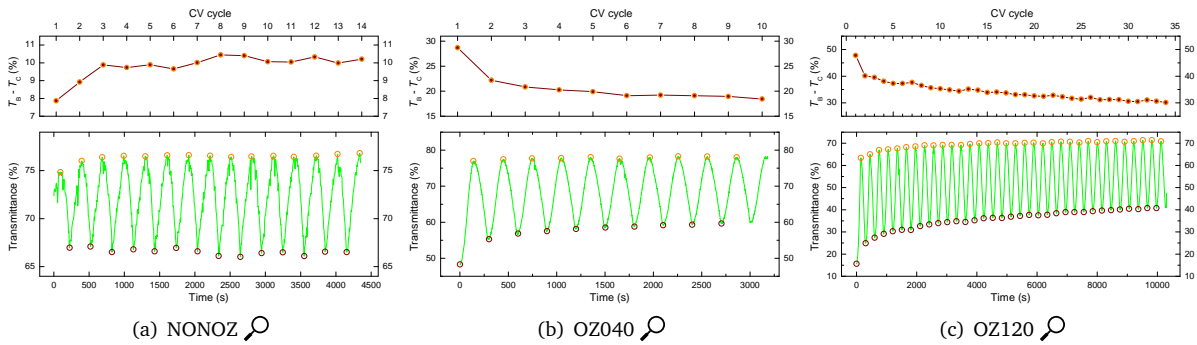


Figure C.5: Optical modulation for (a) NONOZ, (b) OZ040, and (c) OZ120 films cycled in LiPC. The green line is the recorded *in situ* transmittance at 550 nm, and the circles mark the highest and lowest transmission values ( $T_b$  and  $T_c$ ). The smaller subplot shows how the difference  $T_b - T_c$  varies per cycle.

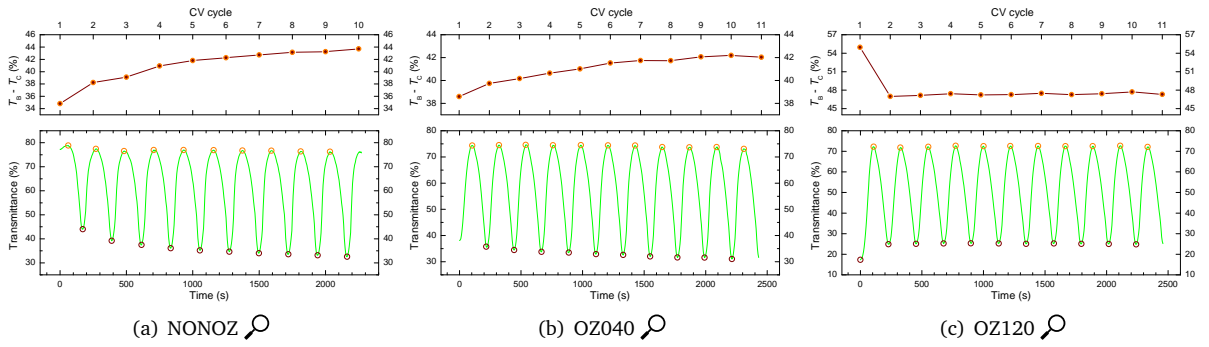


Figure C.6: Optical modulation for (a) NONOZ, (b) OZ040, and (c) OZ120 films cycled in KOH-14. The green line is the recorded *in situ* transmittance at 550 nm, and the circles mark the highest and lowest transmission values ( $T_b$  and  $T_c$ ). The smaller subplot shows how the difference  $T_b - T_c$  varies per cycle.

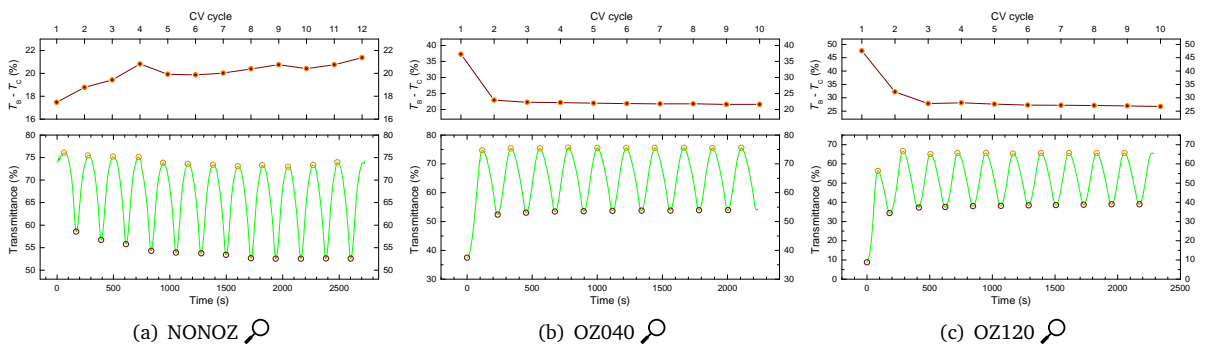


Figure C.7: Optical modulation for (a) NONOZ, (b) OZ040, and (c) OZ120 films cycled in KOH-12. The green line is the recorded *in situ* transmittance at 550 nm, and the circles mark the highest and lowest transmission values ( $T_b$  and  $T_c$ ). The smaller subplot shows how the difference  $T_b - T_c$  varies per cycle.

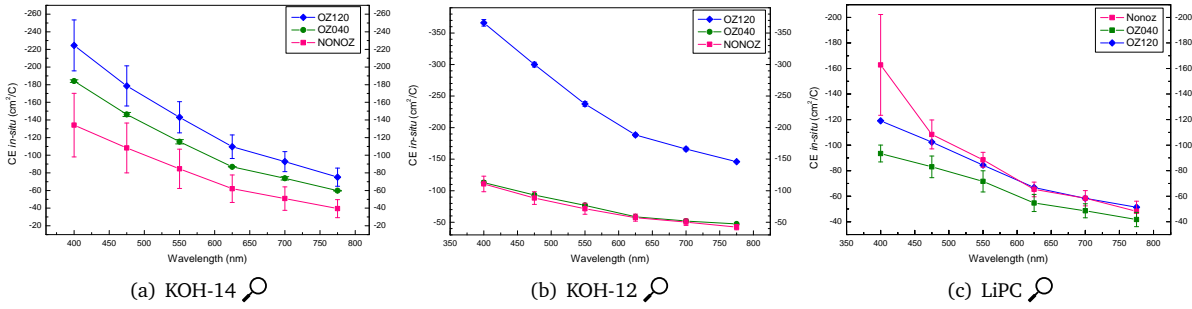


Figure C.8: Colouration efficiency at the last CV cycle for non-ozonated and ozonated films in (a) KOH-14, (b) KOH-12 and (c) LiPC. CE is calculated from *in situ* optical transmittance at 550 nm with the averaged anodic and cathodic charge during the last CV cycle (or the next-to-last cycle if the last cycle did not constitute a full cycle).

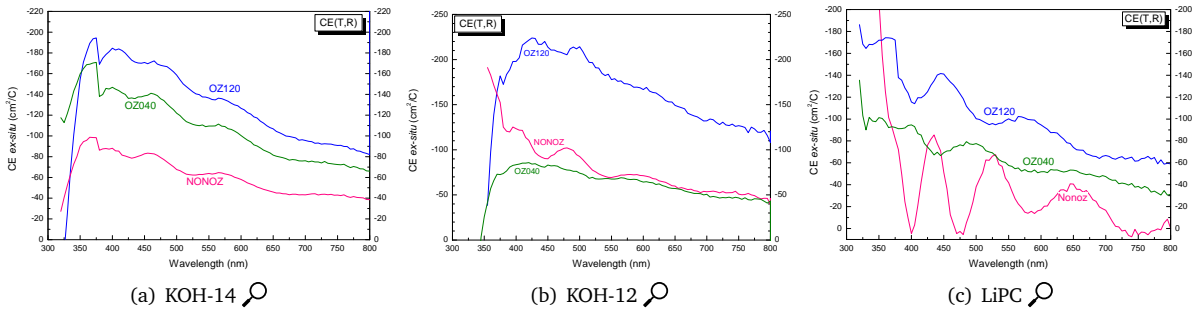


Figure C.9: Colouration efficiency for non-ozonated and ozonated films cycled in (a) KOH-14, (b) KOH-12, and (c) LiPC. CE is calculated from measured transmittance and reflectance spectra recorded *ex situ* after termination of cycling. Exchanged charge is calculated from the anodic and cathodic charge during the last CV cycle (or the next-to-last cycle if the last cycle did not constitute a full cycle).

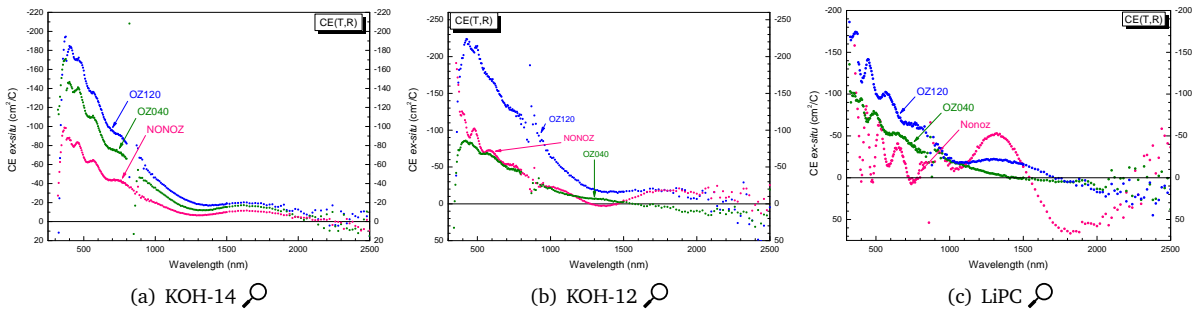


Figure C.10: Colouration efficiency in the full solar wavelength range. Only visible range of these spectra are shown in Figure C.9.

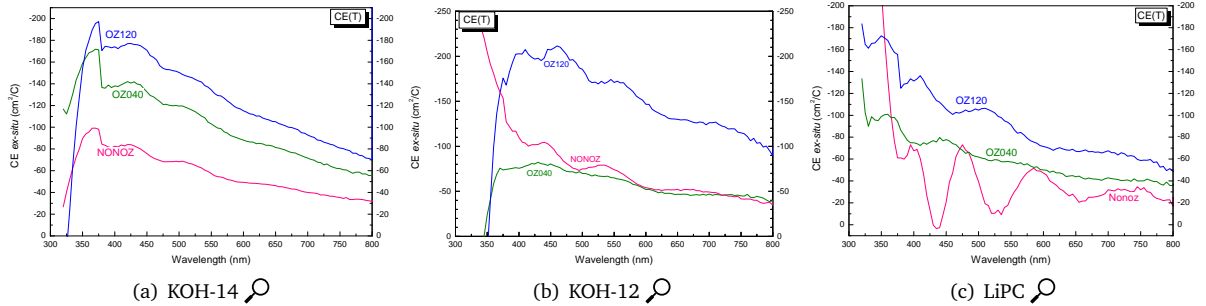


Figure C.11: Colouration efficiency for non-ozonated and ozonated films cycled in (a) KOH-14, (b) KOH-12, and (c) LiPC. CE is calculated from measured transmittance spectra recorded *ex situ* after termination of cycling. Exchanged charge is calculated from the anodic and cathodic charge during the last CV cycle (or the next-to-last cycle if the last cycle did not constitute a full cycle).

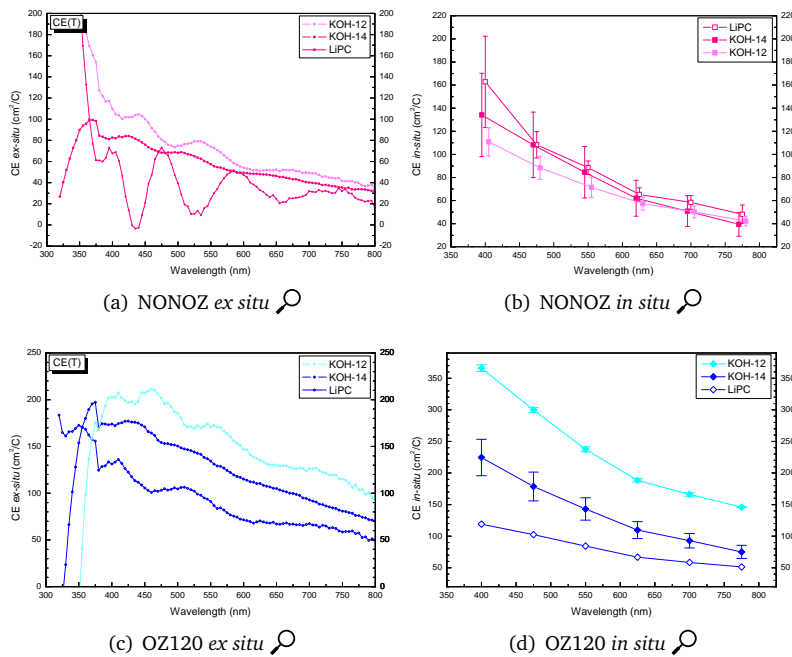


Figure C.12: Comparison of calculated *ex situ* and *in situ* CE for (a), (b) non-ozonated and (c), (d) ozonated films. CE calculated from *in situ* transmittance data are significantly higher, which indicates that the manual handling of the films after cycling termination and prior to *ex situ* spectroscopy affects the results.

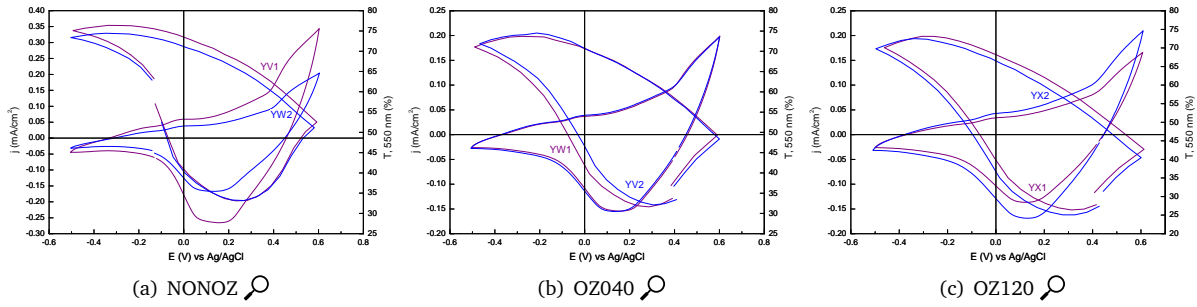


Figure C.13: Recorded CV and *in situ* transmittance at 550 nm for films cycled in KOH-14. For each ozonation state, (a) NONOZ, (b) OZ040, (c) OZ120, two experiments were performed. Each figure shows the recorded CV and  $T_{550}$  from the same cycle. Small deviations between repeat experiments indicate that reproducibility is good.

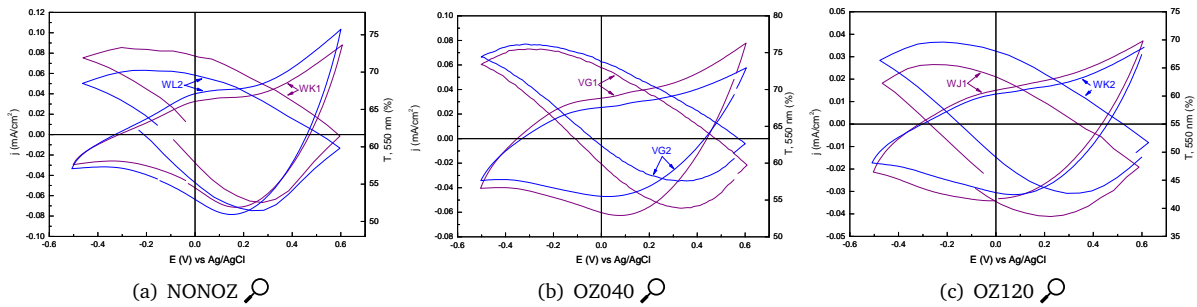


Figure C.14: Recorded CV and *in situ* transmittance at 550 nm for films cycled in KOH-12. For each ozonation state, (a) NONOZ, (b) OZ040, (c) OZ120, two experiments were performed. Each figure shows the recorded CV and  $T_{550}$  from the same cycle. Moderate deviations between repeated experiments.

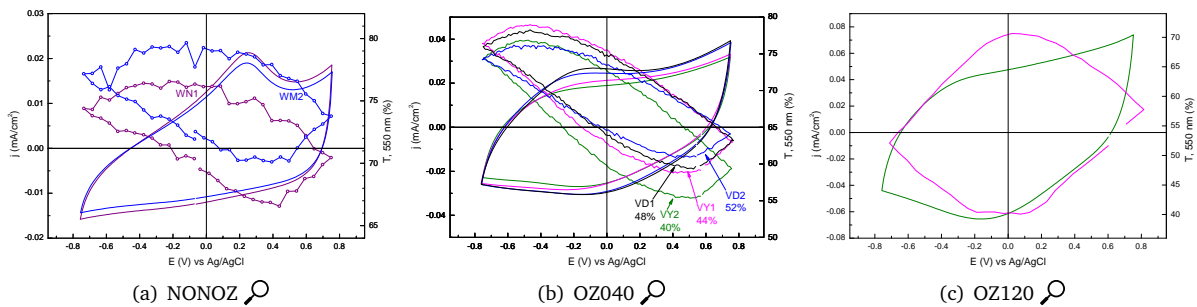


Figure C.15: Recorded CV and *in situ* transmittance at 550 nm for films cycled in LiPC. (a) NONOZ two films, (b) OZ040 four films, (c) OZ120 one film. Each figure shows the recorded CV and  $T_{550}$  from the same cycle. CVs and  $T_{550}$  show small variations. The percentages in (b) indicate  $T_i$  of the film for each experiment.

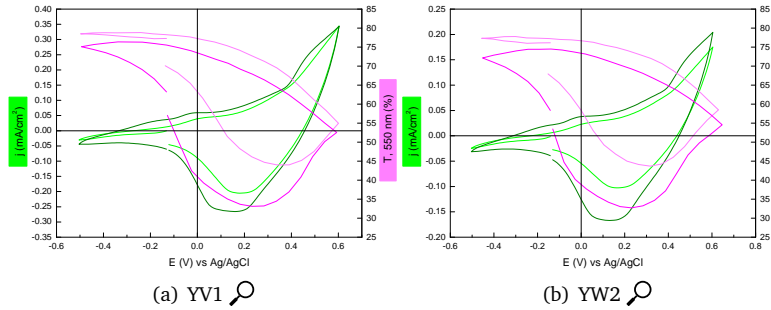


Figure C.16: CV and  $T_{550}$  for non-ozonated films in KOH-14. Both plots show the first (light-coloured) and the ninth cycle (dark-coloured) out of 11 cycles.

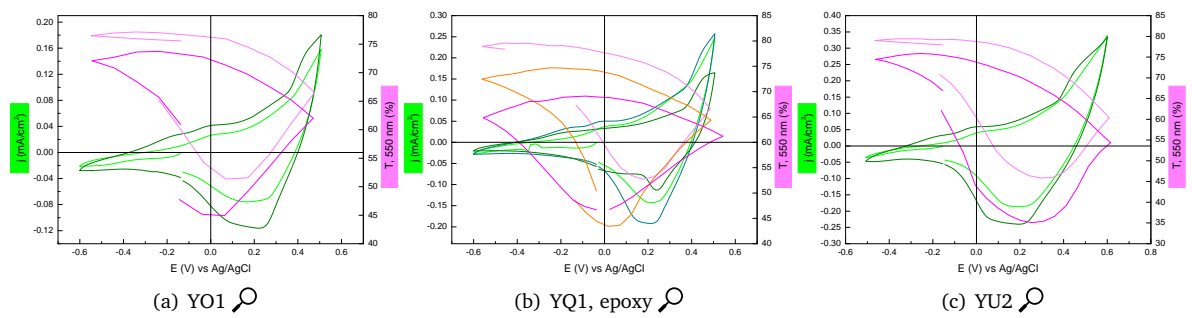


Figure C.17: CV and  $T_{550}$  for non-ozonated films in KOH-14. (a) shows cycles 1 and 15 (of 18), (b) shows cycles 1, 15 and 26 (of 31), (c) shows cycles 1 and 8 (of 11).

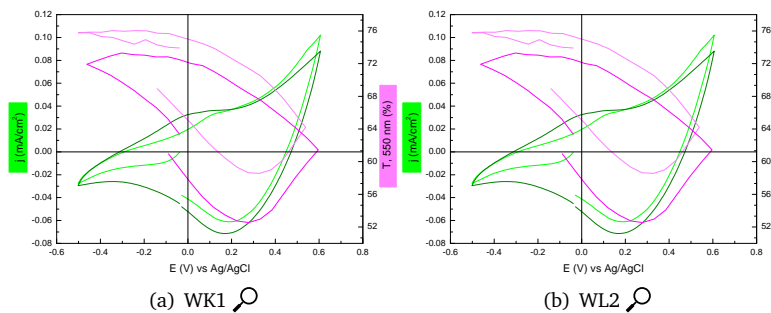


Figure C.18: CV and  $T_{550}$  for non-ozonated films in KOH-12. The light-coloured curves show the first scan, and the darker curves show the ninth scan (out of 13 scans).

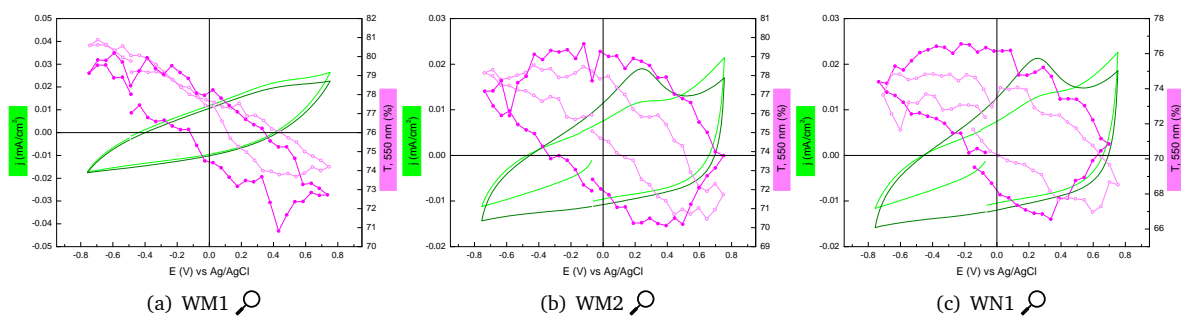


Figure C.19: CV and  $T_{550}$  for non-ozonated films in LiPC. (a) shows the second and 18<sup>th</sup> cycles (of 20), (b) shows the first and 13<sup>th</sup> cycles (of 15), (c) shows the first and 13<sup>th</sup> cycles (of 15).

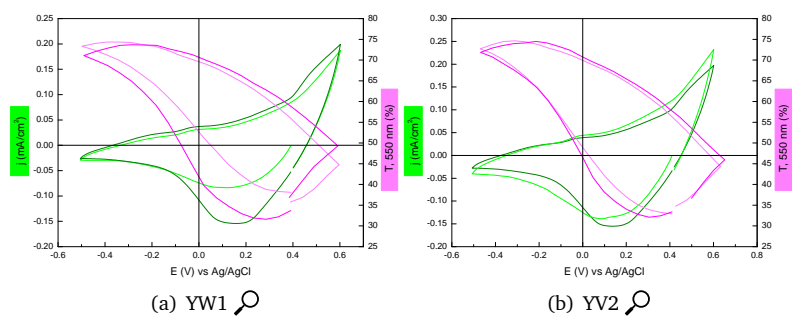


Figure C.20: CV and  $T_{550}$  for intermediately ozonated films in KOH-14. The light-coloured curves show the first scan, and the darker curves show the ninth scan (out of 11 scans).

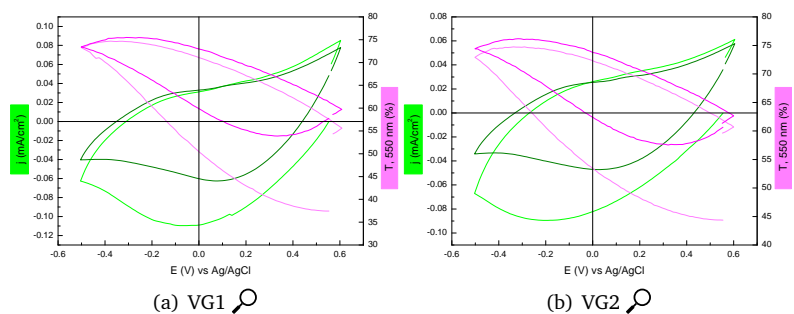


Figure C.21: CV and  $T_{550}$  for intermediately ozonated films in KOH-12. The light-coloured curves show the first scan, and the darker curves show the ninth scan (out of 11 scans).



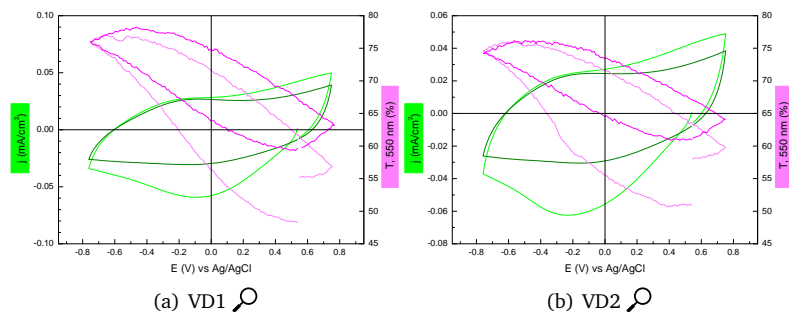


Figure C.22: CV and  $T_{550}$  for intermediately ozonated films in LiPC. The light-coloured curves show the first scan, and the darker curves show the ninth scan (out of 11 scans).

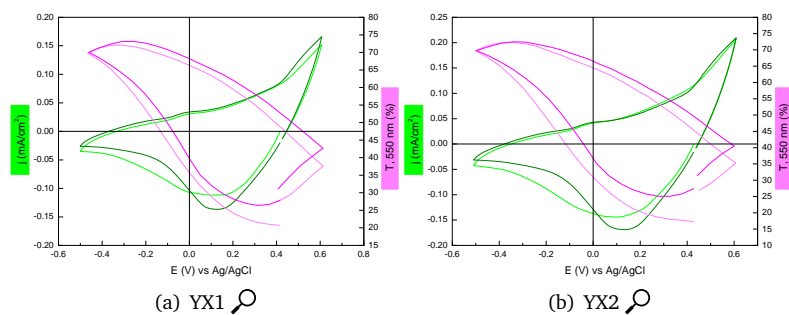


Figure C.23: CV and  $T_{550}$  for ozonated (OZ120) films in KOH-14. The light-coloured curves show the first scan, and the darker curves show the ninth scan (out of 11 scans).

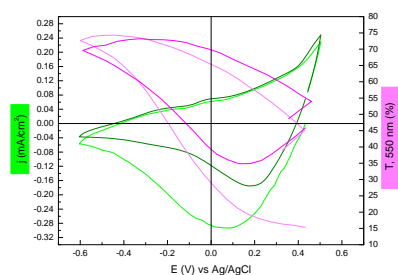


Figure C.24: CV and  $T_{550}$  for YP1, ozonated (OZ120) film in KOH-14. The light-coloured curves show the first scan, and the darker curves show the 16<sup>th</sup> scan (out of 19).

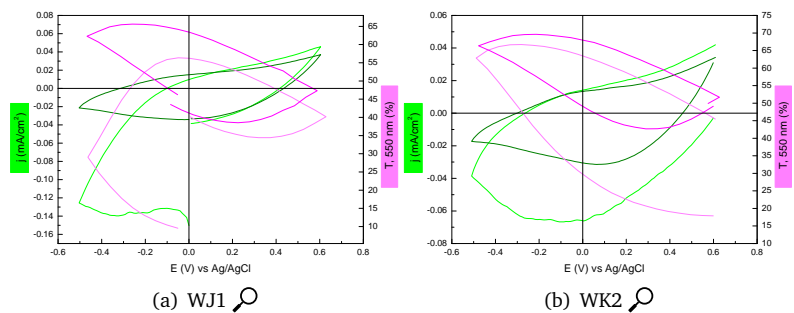


Figure C.25: CV and  $T_{550}$  for ozonated (OZ120) films in KOH-12. The light-coloured curves show the first scan, and the darker curves show the ninth scan (seventh scan for (a)) out of 11.

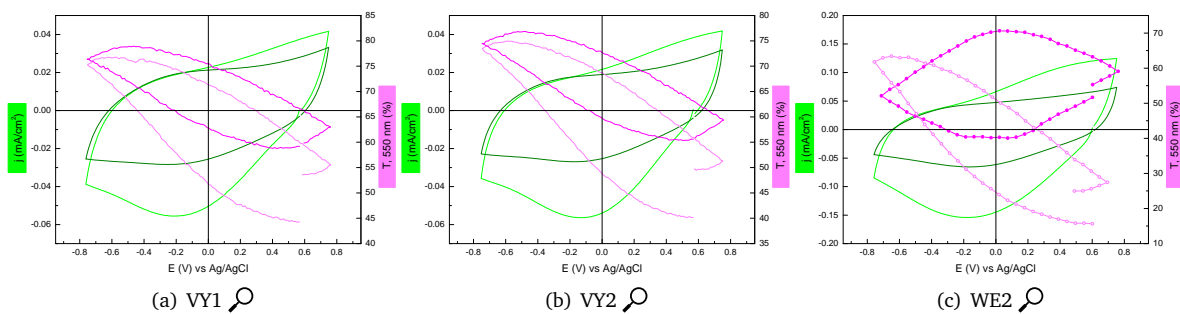


Figure C.26: CV and  $T_{550}$  for ozonated (OZ120) films in LiPC. (a) and (b) show the first and ninth cycles (of 11), (c) shows the first and 30<sup>th</sup> cycles (of 34).

Table C.1: Transmittance at 550 nm for all sheets (except the first, Z-series) in as-deposited state, all measured within two days of sputtering. Measured on different films within each series on the OceanOptics spectrometer.

	$T_{\text{asd}}/\%$	$n$
V-series	$68.1 \pm 1.67$	12
W-series	$69.8 \pm 1.54$	12
X-series	$68.9 \pm 1.09$	12
Y-series	$71.0 \pm 1.52$	8
All sheets	$69.3 \pm 1.76$	

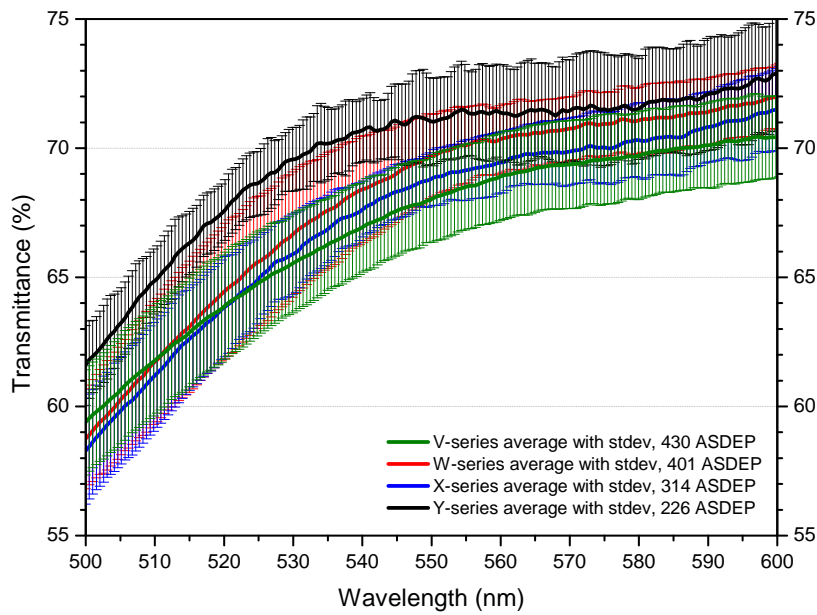


Figure C.27: Average transmittance for as-deposited sheets, here shown in the 500–600 nm range. The standard deviation is also shown. Based on measurements on 12 different films from each series. Also see [Table C.1](#).

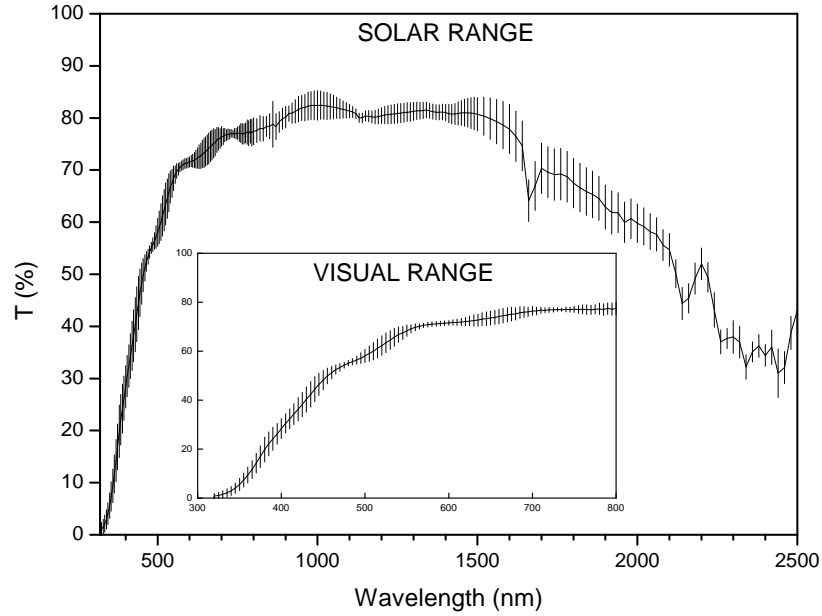


Figure C.28: Averaged as-deposited solar transmittance spectrum. The standard deviation (calculated from 8 measurements) is shown. The low transmittance (which corresponds to high absorptance since reflectance is small) is due to the semiconductor band gap of nickel oxide, plus contributions from the substrate and ITO layer. 🔍

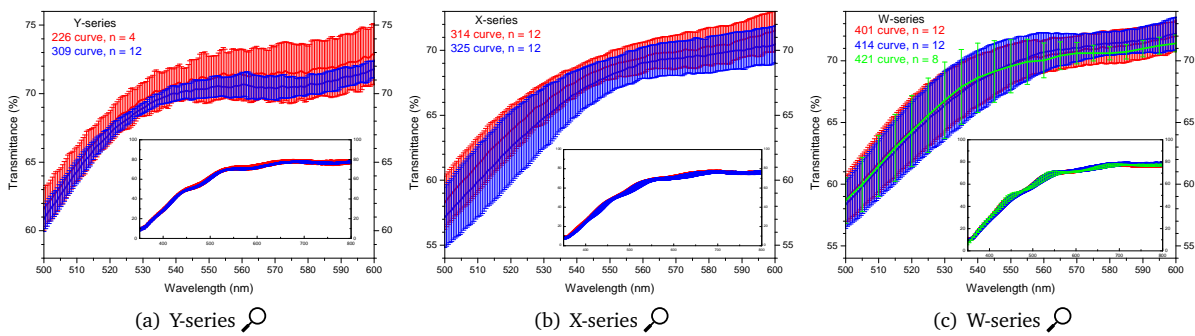


Figure C.29: Change of optical transmittance during storage for each sample series, for (a) Y-series (11 days between measurements), (b) for X-series (11 days between measurements), and (c) for W-series (13 days between measurements). All measurements show no significant change in optical transmittance after storage. Transmittance in itself is thus not a reliable way to measure film “freshness”. 🔍

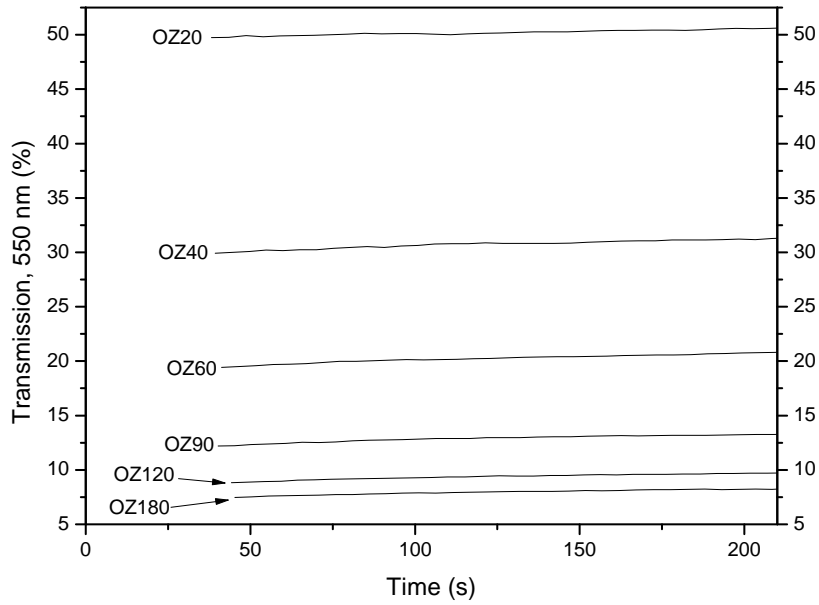


Figure C.30: Post-ozonation increase of optical transmission (at 550 nm) for a nickel oxide layer exposed to air, shown for the first 200 seconds.  $t = 0$  is the end of ozonation, then there is a gap of varying length (roughly 40 s) which is the time it took to setup and start the transmission measurement.

Table C.2: Linear equations fitted to each line in Figure C.30.  $y = at + c$ .

Time (s)	$c$ (%)	$a$ (%/s)	$a^{-1}$ (s/%)	$r^2$
20	49.61	0.0048	209	0.96961
40	29.85	0.0069	145	0.95356
60	19.34	0.0071	141	0.97293
90	12.19	0.0054	186	0.92423
120	8.78	0.0046	217	0.95003
180	7.44	0.0040	253	0.94145





# Document notes

This document features some functionality above the immediately visible content. Generally these features only enrich the on-screen experience, with little to no benefit for the printed document.

## Special functionality

The PDF document comes with *embedded* files, mainly other PDF files and some MATLAB<sup>®</sup> M-files. The use of this PDF-format specific function stemmed from the need to include numerous graphs and plots with high visibility and at the same time conserve page real-estate.

An otherwise common solution is to simply rely on the zoom function built into most PDF-reader software. This works well on-screen, but does not provide an efficient way for clear printing of specific plots or facile recycling of the graphic itself in other ways.

My solution features a magnifying glass symbol, , which is placed in the caption next to the “expandable” graphic. The  symbol is not visible in print (except those on this page), unless the user chooses to print all annotations.

The magnifying glass symbol is clickable, and on double-click opens a new window with the expanded graphic, so it can be viewed, printed or saved separately. This feature will work in all new versions of Adobe Acrobat Reader software and other modern PDF readers.

Hopefully this approach will alleviate the problem with the PDF format’s tendency to “lock-in” data and make it difficult to access and share.

## Hyperlinks and such

This document features internal and external hyperlinks, such as figure references and URL hyperlinks. It also features hyperlinked DOIs in the references. Hyperlinks are a common feature in PDF documents, and need no further explanation.

## Production notes

This document was created using  $\text{\LaTeX}$  2<sub>ε</sub> with the `memoir` class by Peter Wilson and with an array of packages and ad hoc  $\text{\LaTeX}$  programming.

The text body font used is Bitstream Charter (Matthew Carter) at 10pt.

The report was typeset with the base  $\text{\LaTeX}$  release dated 2005/12/01 from the MiK $\text{\TeX}$  2.5 release, which featured pdf $\text{\TeX}$  version 1.30.6.